A search for disappearing tracks in proton-proton collisions at $\sqrt{s} = 8$ TeV

DISSERTATION

Presented in Partial Fulfillment of the Requirements for the Degree Doctor of Philosophy in the Graduate School of The Ohio State University

By

Jessica Danielle Brinson, B.S, M.S.

Graduate Program in Physics

The Ohio State University

2015

Dissertation Committee:

Chris Hill, Advisor

Stan Durkin, Stuart Raby, and Ratnasingham Sooryakamur

Abstract

This thesis presents a search for evidence of new supersymmetric particles in proton-proton collision data collected by the Compact Muon Solenoid at the Large Hadron Collider located in Geneva, Switzerland. The data was collected in 2012 at a center of mass energy of 8 TeV and corresponds to an integrated luminosity of 19.5 fb^{-1}. The search examines events that produce the experimental signature of a disappearing track. Disappearing tracks are identifed as those with little or no associated calorimeter energy deposits and with several missing hits in the outer layers of the tracker. This search is motived by anomaly-mediated supersymmetry which postulates that a long-lived chargino decaying to a neutralino and pion with low momentum could give rise to a disappearing track. The sources of background in this search arise from leptons which fail to be reconstructed and false trajectories determined by the track reconstruction algorithm. The number of observed events is in agreement with the background expectation, and limits are set on the cross section of direct electroweak chargino production in terms of the chargino mass and mean proper lifetime. At 95% confidence level, anomaly-mediated supersymmetry breaking models with a chargino mass less than 260 GeV, corresponding to a mean proper lifetime of 0.2 ns, are excluded.

Acknowledgments

First of all, I would like to thank all of the people who came before me and made the LHC and CMS a reality. This thesis is the result of the large amount of work put into these amazing machines. Next, I would like to thank my advisor Chris Hill for the opportunity to do this unique analysis. His direction and motivation have been indispensable. I would also like to thank Stan Durkin; even though he was not my advisor, he was always happy to help me out. I also need to thank Wells Wulsin, my colleague, friend, and mentor. He was always happy to answer my endless questions, and it was truly a pleasure to work with him. Without his tireless efforts and optimistic attitude, this analysis would not have been possible.

I made it to grad school with the help of James Hostetter, my friend from LSU. My lab partner and faithful friend for years, I remember all the time we spent in Baton Rouge fondly. I would also like to thank the friends that I made here at OSU. Kevin and Joe, two of my first friends when I moved here and my officemates during our first year; Garrett, an honorary member of office 3026 and my favorite person to commiserate with; Brendon, the first person I recognized from open house and who kept in touch with me even when I moved across the Atlantic; Adam, Mike, Jeremy, and Matt, helping me unwind during our weekly lunches; and Marissa, my kindred spirit and the best officemate a girl could ask for.

And to the friends I made at CERN, they immediately made me feel like I was at home instead of a stranger in a strange land. Quiz with Colonel Moutarde, sitting outside at Charley's, and signifying the end of the work week with beers in R1 will always make me smile. Ted, Rachel, Sarah Boutle, and Chris Neu, my CERN gurus, who were happy to give advice about physics and life over lunch or a beer; Justin and Dusty, always up for an adventure, our trip to Barcelona is probably my favorite vacation; Christine, my fellow animated film aficionado; Jamie and Nicole Antonelli, the best neighbors I've ever had, who were always happy to have me in their home; Hasib, from Hungary back to CERN, I had so much fun hanging out with you; Dave and Kat, who helped me appreciate the finer things; Ben, Kristina, and Bing, I met you at OSU, but we didn't truly bond until we were thrown together at CERN; and Michael Planer, the friend I didn't know I was looking for until I met you. I miss you all the time.

Without my family, I never would have made it this far. I would like to thank my sister, Sarah and brother-in-law, Patrick, my brother, Mike and, sister-in-law Becca, Aunt Kris and Uncle Mark, Jaime and Matthew, and Grandpa and Miss Cynthia. Their unending support and affection has never ceased to amaze me. From coming to visit me in Ohio and galavanting around Europe to their constant phone calls and e-mails of love and support, I am always amazed by how lucky I am to have all of you in my life. I am also fortunate to have two nephews, Brock and Peyton, and a niece LaLou. It is a pleasure to be their aunt, and they have brought me so much joy ever since they were born. I cannot imagine my life without them. I would also like to thank my best friend since I was five, William, for always being there for me. I could not have done this without you.

Lastly, I would like to thank my parents, Scotty and Liz Brinson, for their unwavering support over the course of my entire life. They always told me that I could be and do anything. For that, I am truly thankful. I owe everything I have become and everything I have accomplished to them.

Vita

April 17, 1987	Born, Ferriday, LA
May 2005	Graduated from Tensas Academy, St. Joseph, LA
December 2009	B.S. Physics, Louisiana State University
December 2012	M.S. Physics, High Energy Experiment, The Ohio State University
2007-2010	Undergraduate Research Assistant, Louisiana State University.
2010-2011	Graduate Teaching Assistant, The Ohio State University.
2010-present	Graduate Researcher, The Ohio State University.

Publications

CMS Collaboration "Search for disappearing tracks in proton-proton collisions at sqrt(s) = 8 TeV" *Journal of High Energy Physics* **01** (2015) 096. arXiv:1411.6006

CMS Collaboration "Search for fractionally charged particles in pp collisions at sqrt(s) = 7 TeV" *Phys. Rev. D.* **87** (2013) 092008. arXiv:1210.2311

Fields of Study

Major Field: Physics

Contents

Appendices

List of Tables

List of Figures

Chapter 1
Introduction

The Standard Model has been wildly successful in describing physics up to the TeV scale. However, there are still some questions which the Standard Model is not equipped to address such as the differences in the masses of the particles in the Standard Model, the specific values of the coupling constants, or why there are three generations of quarks and leptons. Searches for deviations from the Standard Model that could answer these questions have been performed for years and continue to this day.

This thesis details a search for physics beyond the Standard Model. The Large Hadron Collider, situated in Geneva, Switzerland, has provided many opportunities for exploring the frontier for new physics. In 2012, data was collected by the proton-proton collider at an energy of 8 TeV. At these energies, it is believed that heavier particles, which have yet to be observed could be produced and subsequently detected.

In this thesis, we search for evidence of physics beyond the Standard Model in which a charged supersymmetric particle of intermediate lifetime produces a partially reconstructed track and subsequently decays to a neutral supersymmetric particle. This search is performed at the Compact Muon Solenoid with the data collected during 2012. The Compact Muon Solenoid is a hermetic, general purpose detector designed to detect all particles that result from the proton-proton collisions produced by the Large Hadron Collider.

This thesis is organized as follows. In Chapter 2, we discuss the theoretical motivation for this search. Chapter 3 and Chapter 4 present an overview of the Large Hadron Collider and the detector of interest in this search, the Compact Muon Solenoid. Next, Chapter 5 lists the datasets used in this search, and Chapter 6 details the requirements placed on various selection samples used in this search. Chapter 7 shows how experimental signatures from Standard Model particles can mimic that of the signal. Chapter 8 discusses how the contribution from these sources is predicted while Chapter 9 describes how the sources of uncertainty to this search are addressed. Then, in Chapter 10, the results of the search are presented, and Chapter 11 lists the future preparations. Finally, the conclusion is presented in Chapter 12.

Chapter 2
Theoretical Motivation and Framework

2.1 The Standard Model and the Higgs Mechanism

The Standard Model (SM) is the mathematical framework which has successfully described the fundamental interactions between elementary particles that we have observed to date. The overview presented in this section is not meant to be comprehensive; a more detailed description can be found in [16].

The current framework of the SM came about in the 1960's when Sheldon Glashow, Steven Weinberg, and Abdus Salam combined the electromagnetic and weak forces into one phenomenon, the electroweak force, and incorporated the mechanism for electroweak symmetry breaking [17–20]. Then, in the mid-1960's it was proposed that protons were in fact made of quarks [21]. This hypothesis would grow into the theory of quantum chromodynamics (QCD) and describe the strong force. The electroweak and strong force together allow us to describe the SM as a set of fields which are invariant under a $SU(3)_C \times SU(2)_L \times U(1)_Y$ gauge group. $SU(3)_C$ describes the color interactions among quarks, $SU(2)_L$ describes the weak interactions among quarks and leptons, and $U(1)_Y$, defined as weak hypercharge is related to the electromagnetic interaction. A depiction of the fundamental particles of the SM as well as their interactions with each other can be seen in Figure 2.1.

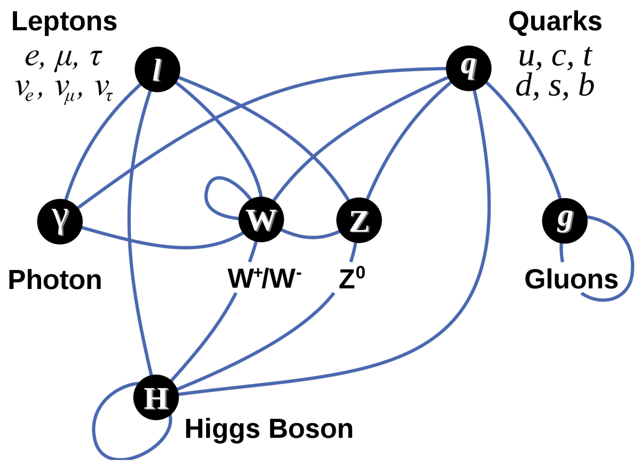

Figure 2.1: A depiction of the particles in the SM and their interactions. The first row represents the fermions, quarks and leptons; the force mediating gauge bosons are shown on the second row; and the Higgs boson is in the last row. The blue lines drawn between the particles represent their interactions at tree level.

The SM has been very successful in predicting and subsequently describing a wide range of physics. Many experiments over the course of several decades have been dedicated to testing the validity of the SM [22–27]. Also, the SM has postulated the mechanism which gives the W and Z bosons their masses while leaving the photon massless, the Higgs mechanism [28, 29]. The Higgs mechanism is responsible for the spontaneous breaking of the $SU(2)_L \times U(1)_Y$ or electroweak symmetry. To accomplish this, a $SU(2)$ scalar doublet is introduced [30]

into the corresponding Lagrangian.

$$\mathcal{L} = \mathrm{T} - \mathrm{V} = (\partial_\mu \phi_\mu)^\dagger (\partial \phi_\mu) - \mu^2 \phi^\dagger \phi - \lambda (\phi^\dagger \phi)^2 \tag{2.1}$$

$$\text{where } V(\phi) = \mu^2 \phi^\dagger \phi + \lambda (\phi^\dagger \phi)^2 \tag{2.2}$$

The potential $V(\phi)$ is the 'Mexican hat potential' shown in Figure 2.2 with $\mu^2 < 0$ and $\lambda > 0$. The minimum for ϕ is $\langle \phi \rangle = \sqrt{\frac{-\mu^2}{2\lambda}} \equiv \frac{\nu}{\sqrt{2}}$. Since the minimum is non-zero

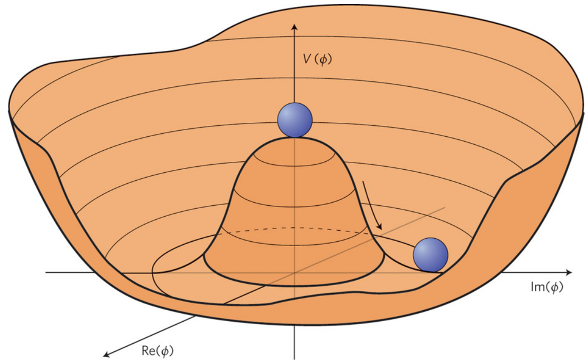

Figure 2.2: The 'Mexican hat potential' associated with the Higgs mechanism. The movement of the ball represents the spontaneous breaking of electroweak symmetry as it falls into the minimum of the potential [1].

ie.e there is a non-zero vacuum expectation value (VEV), we can choose:

$$\langle \phi \rangle = \begin{pmatrix} 0 \\ \frac{\nu}{\sqrt{2}} \end{pmatrix} \tag{2.3}$$

If we then expand ϕ about its VEV in the Lagrangian, a new scalar particle, the Higgs boson, will be introduced with $\langle H \rangle = \sqrt{\frac{m_H^2}{2\lambda}}$, where $m_H^2 \equiv \lambda \nu^2$. In addition, we will get mass terms for the W and Z bosons while leaving the photon massless. A new boson with a mass of 125 GeV was discovered by the general purpose detectors at the Large Hadron Collider (LHC) in 2012, which is consistent with the SM Higgs boson [31, 32]. Once data taking resumes in the middle of 2015, more precise measurements of the boson's quantum numbers will tell us if it remains consistent with a SM Higgs boson.

2.2 Motivation for Supersymmetry

The latest discovery of a new boson consistent with the SM Higgs is the quintessential success of the of the SM to date; however, there are still some questions that the SM is unable to answer. One of the main reasons for the introduction of supersymmetry (SUSY) is the resolution of the hierarchy problem.

The hierarchy problem, stated in the simplest of terms, tells us that the predicted mass of the Higgs as well as the mass of the new boson discovered at the LHC are much lighter than expected once corrections from quantum field theory to this mass are included. From experiments involving the weak interactions, it has been experimentally determined that the mass of the Higgs boson should be ~100 GeV; this is consistent with the measured mass of the new boson at 125 GeV. Now, let us account for the quantum corrections to this value. Figure 2.3 shows the loop corrections for fermions and scalars. These corrections are enormous and one exists for every particle that couples directly or indirectly to the Higgs. These corrections

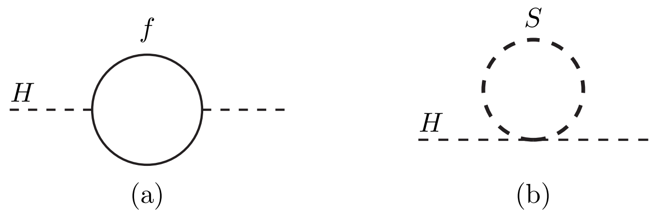

Figure 2.3: One loop corrections to the Higgs mass for (a) fermions (f) and (b) scalars (S) [2].

for fermions are of the form:

$$\Delta m_H^2 = -\frac{|\lambda_f|^2}{8\pi^2}\Lambda_{UV}^2 + ... \tag{2.4}$$

λ_f is the coupling constant of the fermion to the Higgs, and Λ_{UV} is the momentum cutoff that is used to regulate the integral and can be thought of as an energy scale in which new physics would have to enter to modify the high energy behavior of the theory. If we take λ_f as 1, for the largest correction which comes from the top quark, and Λ_{UV} as the Planck scale or 10^{18} GeV then these corrections would give a mass to the Higgs that is 30 orders of magnitude larger than expected. To solve this problem, SUSY proposes that there exists a scalar particle that also couples to the Higgs with corrections of the form:

$$\Delta m_H^2 = \frac{\lambda_S}{16\pi^2}\Lambda_{UV}^2 + ... \tag{2.5}$$

Therefore, if there were a symmetry between fermions and bosons that gives rise to two complex scalars, with $\lambda_S = |\lambda_f|^2$, that accompanied each of the quarks and leptons, then the mass of the Higgs would be in the 100 GeV range. However, these massive scalars must be $\sim$ 1 TeV if these cancellations are to occur naturally.

In addition to providing a solution to the hierarchy problem, SUSY makes two other predictions that make it a desirable theory. At higher energy scales or $\sim 10^{16}$ GeV, the electroweak and strong forces will unify to single strength as shown in Figure 2.4. Secondly, SUSY provides a natural candidate for dark matter. If the lightest stable particle in the SUSY mass spectrum does not decay to SM particles and only interacts weakly, then dark matter could be included in the supersymmetric extension to the SM [2].

2.3 Introduction to SUSY

A supersymmetry transformation is defined as an operation that changes a fermion into a boson and vice versa.

$$Q\,|\text{Boson}\rangle = |\text{Fermion}\rangle \quad Q^\dagger\,|\text{Fermion}\rangle = |\text{Boson}\rangle \tag{2.6}$$

Where $Q(Q^\dagger)$ are intrinsically complex spinors that act as the generators of supersymmetric transformations. The single particle states of supersymmetry are constructed as irreducible representations of the algebra associated with supersymmetry and are known as supermutliplets. Each supermultiplet contains both fermion and

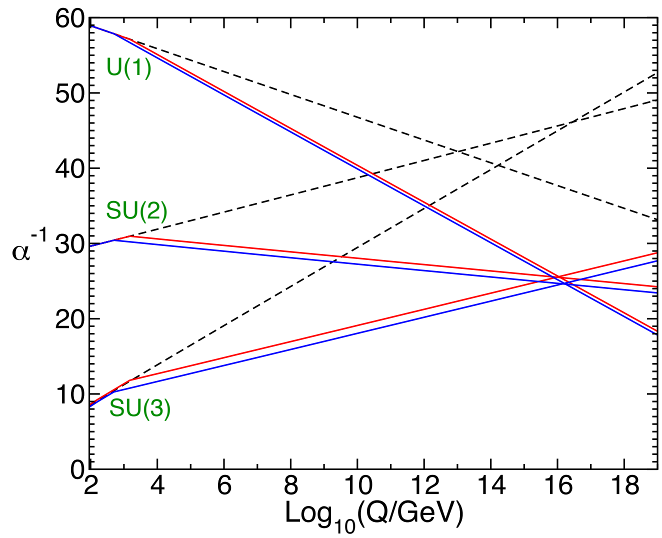

Figure 2.4: Inverse gauge couplings in the SM represented by dashed lines and the minmal supersymmetric extension to the SM represented by solid lines. The different colored lines represent variations in the masses of the SUSY particles [2]

boson members by construction. The simplest multiplet consists of a Weyl fermion and two real scalars, grouped into one complex scalar field; this multiplet is defined as a chiral multiplet. All know SM quarks, leptons, and the SM Higgs reside in chiral multiplets. There is also a vector boson multiplet which consists of one Weyl fermion and one real boson used to represent the photon, W, Z, and gluon. Lastly, there is a gravity multiplet, which consists of spin 3/2 fermions and one graviton. All multiplets available in the minimal extension to the supersymmetric standard model are listed in Figure 2.5. Note that SUSY calls for two Higgs doublets; one (H_u) gives mass to the up-type quarks and the other (H_d) gives mass to down-type quarks. Other, unlisted supersymmetric particles or sparticles arise from linear combinations of those listed in Figure 2.5. There are two linear combinations of charged winos and charged higgsinos known as charginos (denoted by $\chi^{\pm}$). There are 4 states which result from the mixing of the bino, neutral wino, and neutral higgsinos known as neutralinos

Names		spin 0	spin 1/2	$SU(3)_C,\ SU(2)_L,\ U(1)_Y$
squarks, quarks	Q	$(\widetilde{u}_L\ \ \widetilde{d}_L)$	$(u_L\ \ d_L)$	$(\ \mathbf{3},\ \mathbf{2}\ ,\ \frac{1}{6})$
(×3 families)	$\overline{u}$	$\widetilde{u}^*_R$	$u^\dagger_R$	$(\ \overline{\mathbf{3}},\ \mathbf{1},\ -\frac{2}{3})$
	$\overline{d}$	$\widetilde{d}^*_R$	$d^\dagger_R$	$(\ \overline{\mathbf{3}},\ \mathbf{1},\ \frac{1}{3})$
sleptons, leptons	L	$(\widetilde{\nu}\ \ \widetilde{e}_L)$	$(\nu\ \ e_L)$	$(\ \mathbf{1},\ \mathbf{2}\ ,\ -\frac{1}{2})$
(×3 families)	$\overline{e}$	$\widetilde{e}^*_R$	$e^\dagger_R$	$(\ \mathbf{1},\ \mathbf{1},\ 1)$
Higgs, higgsinos	H_u	$(H_u^+\ \ H_u^0)$	$(\widetilde{H}_u^+\ \ \widetilde{H}_u^0)$	$(\ \mathbf{1},\ \mathbf{2}\ ,\ +\frac{1}{2})$
	H_d	$(H_d^0\ \ H_d^-)$	$(\widetilde{H}_d^0\ \ \widetilde{H}_d^-)$	$(\ \mathbf{1},\ \mathbf{2}\ ,\ -\frac{1}{2})$

Names	spin 1/2	spin 1	$SU(3)_C,\ SU(2)_L,\ U(1)_Y$
gluino, gluon	$\widetilde{g}$	g	$(\ \mathbf{8},\ \mathbf{1}\ ,\ 0)$
winos, W bosons	$\widetilde{W}^\pm\ \ \widetilde{W}^0$	$W^\pm\ \ W^0$	$(\ \mathbf{1},\ \mathbf{3}\ ,\ 0)$
bino, B boson	$\widetilde{B}^0$	B^0	$(\ \mathbf{1},\ \mathbf{1}\ ,\ 0)$

Figure 2.5: Chiral multiplets (top) and vector multiplets (bottom). [2]

(denoted by χ^0). These are the states that are able to be experimentally determined and are those which will be of interest in the search detailed in this thesis [2].

Obviously, we have found none of the particles that I have just mentioned. If supersymmetry were a perfect symmetry, then we would have found these particles long ago as the sparticles would be of the same mass as their SM fermionic counterparts. Therefore, SUSY must be a broken symmetry, which raises the question of how? There are many proposed mechanisms for the breaking of supersymmetry, including mediation as well as explicity adding terms to the supersymmetric Lagrangian [33]. This search focuses on anomaly-mediated supersymmetry breaking.

2.4 Anomaly-Mediated Supersymmetry Breaking

The theory of Anomaly-Mediated Supersymmetry Breaking (AMSB) relies on the existence of a 'hidden sector' where SUSY is broken. Otherwise, some of the sparticles should have already been discovered [2]. This is then communicated to the visible sector where we would detect it experimentally. A schematic of how SUSY breaking is transmitted to the visible sector is shown in Figure 2.6.

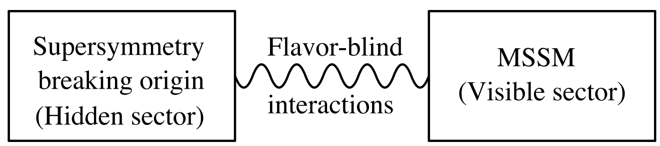

Figure 2.6: Proposed schematic for the breaking of supersymmetry [2]

The mechanism for how SUSY breaking is communicated from the hidden sector to the visible one is debated. In AMSB, the SUSY-breaking effects are transferred soley by gravity interactions since AMSB is a special case of purely gravity mediated supersymmetry [34]. In both purely gravity mediated SUSY breaking and AMSB, there are so-called anomaly-mediated contributions which arise from the super-Weyl anomaly [35], which can be thought of as an extension of scale invariance. The difference between the two theories lies in that SUSY breaking in the gravity mediated case is communicated to the observable sector at tree level by operators that are suppressed by the Planck scale. This direct, tree level interaction between the two sectors dominates over the aforementioned anomaly-mediated effects. In AMSB, there is no direct communication between the hidden sector and observable sector, and the anomaly-mediated terms are allowed to become the dominant contributions. Thus, the three gaugino masses, generated at one loop, are

$$M_i = \frac{b_i g_i^2}{16\pi^2} m_{3/2} \tag{2.7}$$

where $m_{3/2}$ is the gravitino mass, $g_i = g_1,\ g_2,\ g_3$ are the guage couplings to $U(1)$, $SU(2)$, and $SU(3)$, and b_i are the coefficients of the gauge group beta functions. The beta function encodes the dependence of a coupling parameter on the energy scale. The values of b_i are ($\frac{33}{5}$, 1, -3). From these, we can determine the following relation between the gaugino masses [3].

$$M_1 : M_2 : M_3 = 2.8 : 1 : -8.3 \tag{2.8}$$

which differs from the relation of $M_1 : M_2 : M_3 = 1 : 2 : 7$ in other gravity mediated models. This implies that the lightest chargino ($\chi_1^{\pm}$) and neutralino (χ^0) masses are nearly degenerate. They can be written following the notation of [36].

$$m_{\chi_1^{\pm}} = M_2 - \frac{M_W^2}{\mu} \sin 2\beta - \frac{M_2 M_W^2}{\mu^2} + \mathcal{O}\left(\frac{1}{\mu^3}\right), \tag{2.9}$$

$$m_{\chi^0} = M_2 - \frac{M_W^2}{\mu} \sin 2\beta - \frac{M_2 M_W^2}{\mu^2} - \frac{M_W^4 \tan^2\theta_W}{(M_1 - M_2)\mu^2} \sin^2 2\beta + \mathcal{O}\left(\frac{1}{\mu^3}\right). \tag{2.10}$$

where M_2 is one of the aforementioned gaugino masses, M_w represents the weak scale ($\sim$ 100 GeV), tanβ is the ratio of the Higgs vacuum expectation values, and μ is the Higgsino mass parameter. Allowed values for μ and M_2 are shown in Figure 2.7 for two values of tanβ.

The mass difference between the chargino and neutralino can be written as

$$\Delta m = \frac{M_W^4 \tan^2\theta_W}{(M_1 - M_2)\mu^2} \sin^2 2\beta \tag{2.11}$$

Additionally, there are one-loop corrections to the chargino mass, increasing it by $\sim$ 150 MeV; thus Δm is always greater than the pion mass [37]. The mass difference

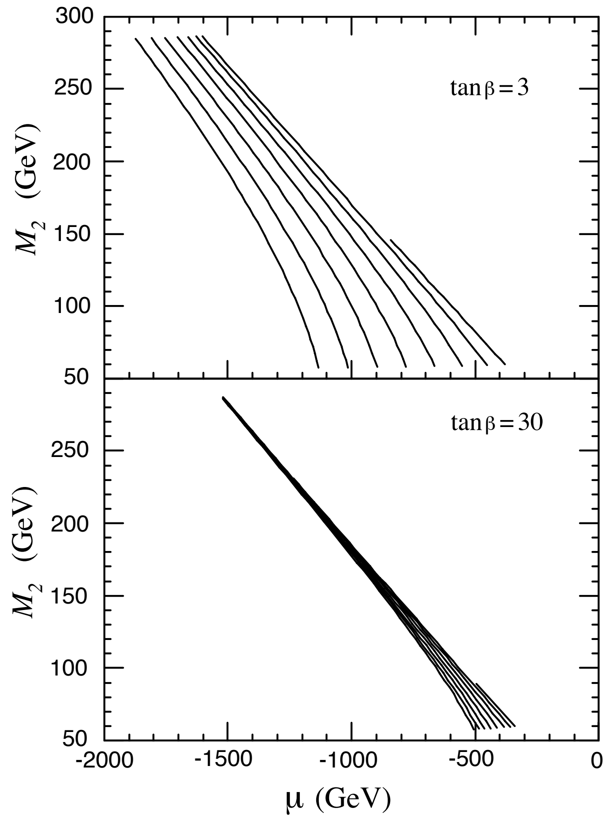

Figure 2.7: Allowed parameters in the (μ,M_2) plane for $\mu < 0$ and tanβ = 3 and 30. Similar results hold for $\mu > 0$ [3]

.

determines the chargino lifetime and is typically between 140-200 MeV.

2.5 An Experimental Signature of AMSB

The small mass difference between the chargino and neutralino gives rise to an interesting experimental signature that is exploited in this thesis. We examine the case where the chargino decays to a neutralino and a pion, $\chi_1^\pm \to \chi_1^0 \pi^\pm$. The phase space for this decay is limited by the small chargino-neutralino mass difference. Consequently, the chargino has a significant lifetime, and the daughter pion has momentum of $\approx$100 MeV, typically too low for its associated track to be identified by the

Compact Muon Solenoid (CMS). The neutralino does not interact with the detector material since it is neutral and weakly interacting; thus, it evades detection. However, the significant lifetime of the chargino does allow for it to be detected in the tracker. Therefore, we can search for the experimental signature of a 'disappearing track', a track that is identified within the tracker volume of the detector, but decays before reaching the muon system. More conventional searches are not sensitive to this signature since the chargino is long-lived enough to produce a partial track within the tracker volume. On the other hand, searches for long-lived charginos could also have missed this signature since the chargino is not long-lived enough to reach the muon system.

2.6 Experimental Status of SUSY

Experimental searches for SUSY have been done for years at LEP (the precursor to the LHC) [38, 39] as well as at the D0 [40] and CDF [41] experiments located at Fermilab. At the LHC, CMS and A Toroidal LHC ApparatuS (ATLAS) experiments continue to search for SUSY, but no experimental evidence for these particles has been found. The summary of SUSY results presented in 2014 for CMS are shown in Figure 2.8, which shows the range of sparticles masses that have been excluded. We can see that the available parameter space for sparticles to solve the hierarchy problem naturally is being squeezed. Since conventional searches are pushing the SUSY scale to higher and higher masses, experimentalists and theorists are looking into signatures that may have evaded these searches such that a natural solving of the hierarchy problem is still possible.

One way that this could occur is if the supersymmetric particles are in fact long-lived. Previous CMS analyses have searched for long-lived charged particles that reach the muon system. The experimental signature is based on anomalous ionization

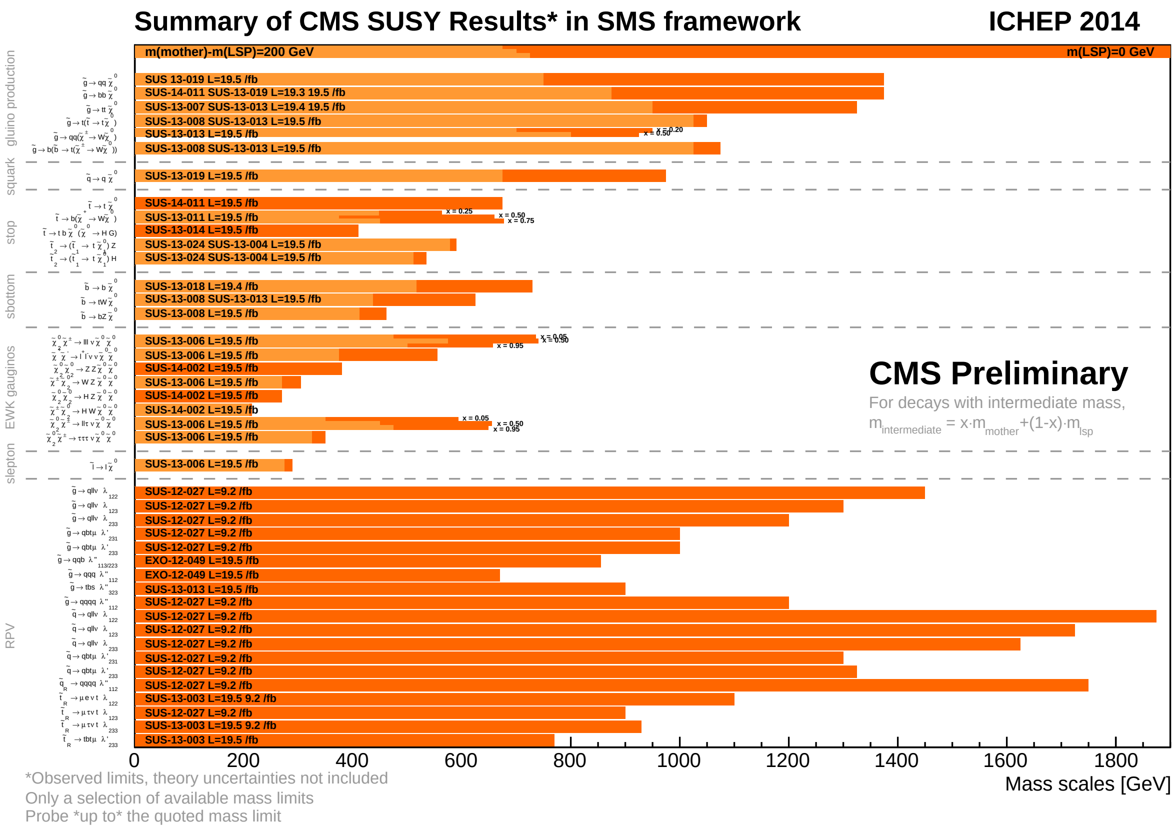

Figure 2.8: Best exclusion limits in the Simplified Model Spectra (SMS) framework. These limits were collected by CMS and presented at ICHEP conference. Branching ratios of one are assumed and values shown in this plot are to be interpreted as upper limits [4].

.

energy loss [42–44]. In Figure 2.9, the parameter points excluded in the Phenomenological Minimal Supersymmetric Model (pMSSM) by conventional SUSY searches as well as those additional points excluded by the long-lived search are shown. The pMSSM is a constrained theory of SUSY that only uses 19 parameters as opposed to the ∼100 free parameters in unconstrained theories of SUSY [45, 46]. This thesis serves to close the gap between these two types of searches.

CMS has never performed a search for long-lived particles based on the signature

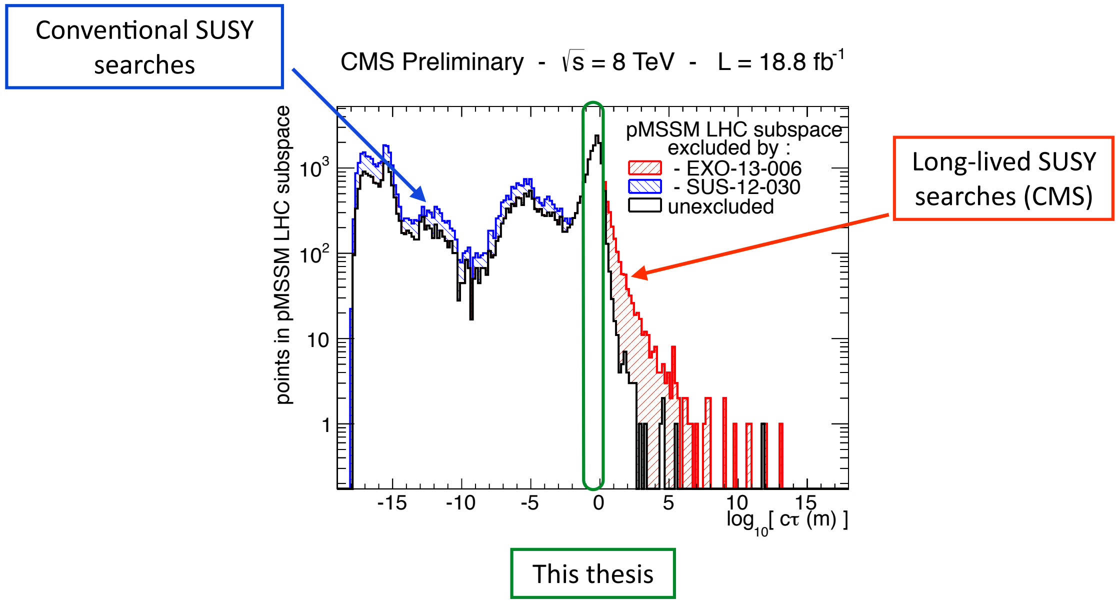

Figure 2.9: Exclusion of points in the pMSSM for conventional SUSY searches ($c\tau \lesssim 1$ mm) and long-lived searches at CMS ($c\tau \gtrsim 1$ m). This thesis closes the gap between these two searches and covers 0.1 m $\lesssim c\tau \lesssim$ 1m.

.

of a disappearing track. However, a search for disappearing tracks has been conducted by the ATLAS Collaboration and excludes at 95% confidence level (CL) a chargino in AMSB scenarios with mass less than 270 GeV and mean proper lifetime of approximately 0.2 ns [6]. The results of the ATLAS search are summarized in Figure 2.10. The search detailed in the remainder of this thesis corroborates the results presented by ATLAS. In addition, it rules out the 2σ excess that was seen in the p_T distribution, shown in Figure 2.11.

The results of this thesis form the basis for the CMS paper "Search for disappearing tracks in proton-proton collisions at sqrt (s)= 8 TeV" published in January of 2015 [47].

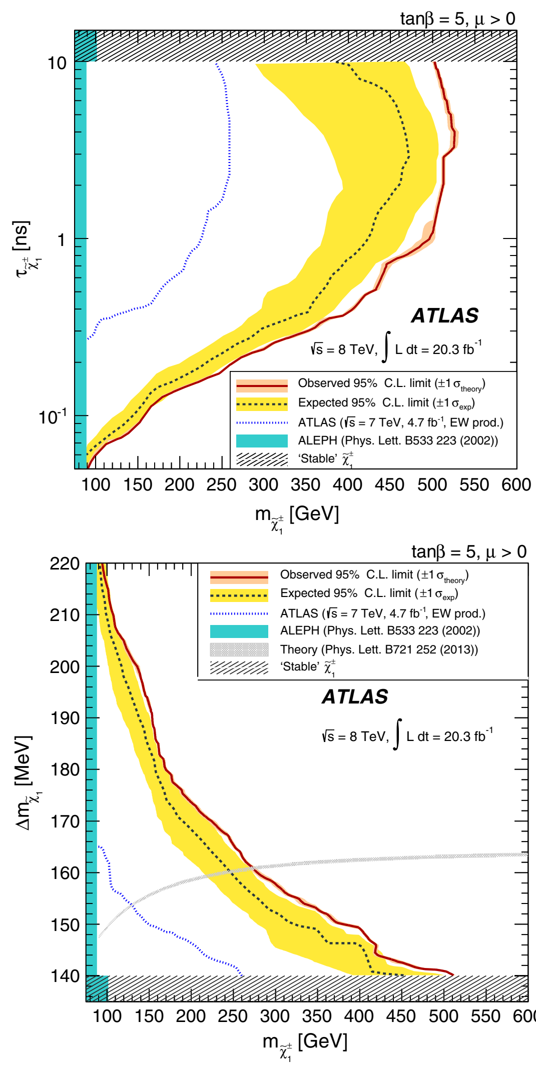

Figure 2.10: Expected and observed constraints on the allowed chargino lifetime ($\tau_{\chi_1^\pm}$) and chargino mass ($m_{\chi_1^\pm}$). Charginos that fall to the left of the solid red line are excluded at the 95% CL (top). The expected and observed constraints on the chargino mass and the mass splitting between the chargino and neutralino, $\Delta m_{\chi_1^\pm}$, in the AMSB model. The region to the left of the curve is excluded at 95% CL. The prediction for $\Delta m_{\chi_1^\pm}$ from [5] is also indicated (bottom) [6].

.

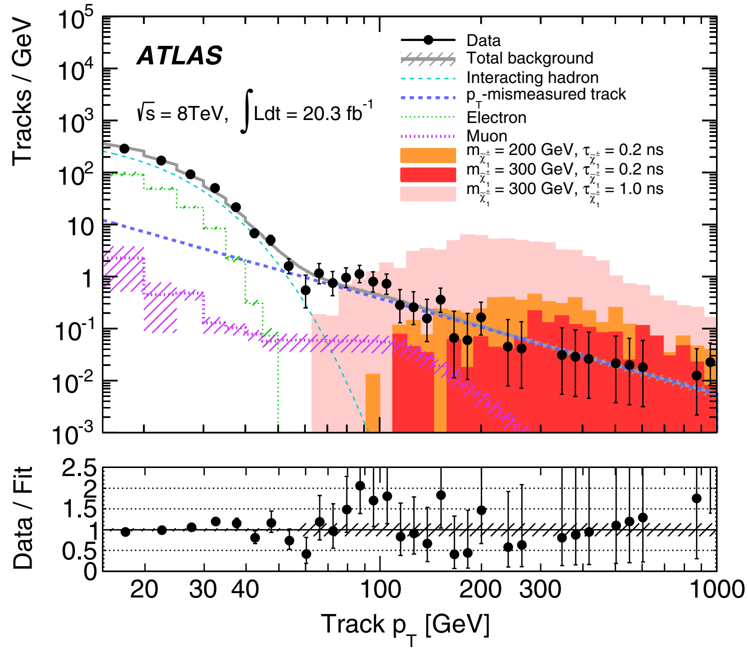

Figure 2.11: The p_T distribution of events that contain a candidate disappearing track. The solid circles show data and lines show each background track p_T spectrum obtained by the background only fit. The resulting uncertainties on the p_T spectrum for each background are indicated by the error band. The signal expectations are also shown. The ratio of the data to the background track p_T spectrum is shown at the bottom of the figure [6].

.

Chapter 3
The Large Hadron Collider

The Large Hadron Collider (LHC) is the largest particle accelerator to date. It is 27 km in circumference and is located ~ 100 m underground on the Franco-Swiss border near Geneva, Switzerland. The main physics goals of the LHC are to confirm the SM, determine the mechanism of electroweak symmetry breaking, and search for theorized BSM particles. In this chapter we will briefly discuss the LHC. An overview is given in Section 3.1, followed by a description of the injection chain in Section 3.2, and a summary of some key features in Section 3.3. Unless otherwise noted, the information in this chapter is taken from [48].

3.1 Overview

The LHC is designed to collide two oppositely circulating proton-proton (pp) beams with a center of mass energy ($\sqrt{s}$) of 14 TeV. In 2011, $\sqrt{s}$ was 7 TeV and in 2012, $\sqrt{s}$ was 8 TeV. From 2013 to 2015, the LHC was shut down for a technical stop and data taking will resume later this year with $\sqrt{s}$ of 13 TeV.

The protons that are collided by the LHC are divided into groups known as bunches. Each bunch contains approximately 10^{11} protons that are collided every

25 ns. The number of events created at the LHC per second is given by

$$N_{event} = L\sigma_{event} \tag{3.1}$$

where σ_{event} is the cross section of the event and L is the instantaneous luminosity. The instantaneous luminosity is determined by the beam parameters to be

$$L = \frac{N_b^2 n_b f_{rev} \gamma_r}{4\pi\epsilon_n \beta*} F \tag{3.2}$$

where N_b is the number of particles per bunch, n_b is the number of bunches per beam, f_{rev} is the revolution frequency, and γ_r is the relativistic gamma factor. ϵ_n is the normalized beam emittance, a measure of the spread of the beam in the plane transverse to its motion. A smaller emittance implies that the particles of the beam are squeezed into a smaller space, resulting in a higher luminosity. $\beta*$ is a measure of the transverse size of the particle beam at the collision point; it is related to the focusing strength of the magnets at those points. Lastly, F is a geometric luminosity reduction factor related to the crossing angle of the bunches when they collide.

The values for these parameters are as follows: N_b is $1.15{\times}10^{11}$ and n_b is 2808, f_{rev} is set by the LHC circumference to be 11.245 kHz, and γ_r is set by the beam energy to be 4 TeV in 2012 or 7 TeV at the design energy. ϵ_n is 3.75 μm while β^* and the maximum crossing angle are set by the magnets at the intersection points to be 0.55 and 285 μrad, respectively. The crossing angle is to avoid unwanted collisions in the part of the LHC where the two beams share a common vacuum chamber. From these, the design luminosity of the LHC is $1.0{\times}10^{34}$ cm^{2}s^{-1}, and the peak luminosity in 2012 was 7.67 $\times 10^{33}$cm^{2}s^{-1} [49].

The luminosity at the LHC does not remain constant over the course of a physics run; it decays, mainly due to beam loss from collisions. Another important source of beam loss is the scattering of protons on residual gas molecules in the beam pipe.

Other, smaller sources of beam loss are Coloumb scattering of protons traveling together or protons traveling in different bunches when crossing the interaction points. These sources of beam loss limit the lifetime of the beam to approximately 15 hours.

The time integral of the instantaneous luminosity provides a measure for how much data has been recorded by the LHC and CMS. CMS logs how much of the luminosity has been 'delivered' as well as how much has been 'recorded.' The delivered luminosity refers to the amount of luminosity that is seen by CMS. If everything worked perfectly, then the recorded and delivered luminosity would be identical. However, in some cases, CMS is unable to take data because the data acquisition chain is busy or because one of the subsystems is down. The recorded and delivered luminosity for 2012 is shown in Figure 3.1.

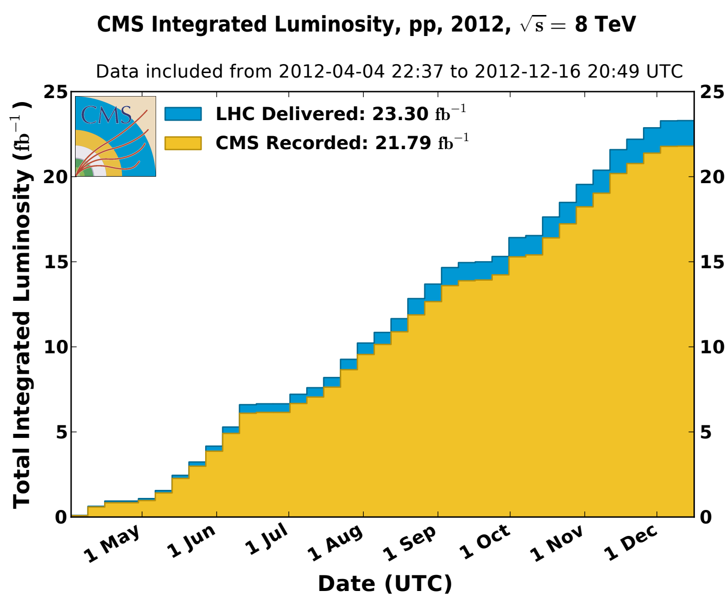

Figure 3.1: Delivered and recorded luminosity by CMS in 2012 [7]

Figure 3.2 shows the layout of the LHC. It consists of eight arcs and 8 straight sections. Each straight section is 528 m long and can be used as an insertion point. The two high luminosity experiments at the LHC, A Toroidal LHC Apparatus (ATLAS) and the Compact Muon Solenoid (CMS) are located directly opposite of each other around the LHC ring at Point 1 and Point 5 respectively. They expect to have a peak luminosity of 10^{34}cm^{2}s. At Point 8 lies a lower luminosity experiment dedicated to B physics, LHCb, which expects a peak luminosity of 10^{32}cm^{2}s. At Point 2, there is one ion experiment, A Lead Ion Colliding Experiment (ALICE), which expects 10^{27}cm^{2}s with lead-lead collisions. Points 2 and 8 are also used as the access points for injection of the beams. These experiments mark the only places where the beams cross to induce collisions. At the non-crossing points, the LHC has two RF systems at Point 4, discussed in Section 3.3.2. Lastly, two collimation systems used to clean the beams are located at Points 3 and 7. The collimation systems define the aperture sizes for the circulating beams and are designed to protect against the sources of beam loss.

3.2 Injection Chain

To produce the protons that are used for collisions, the LHC first begins with a bottle of hydrogen gas. Then the protons are sent through several machines which increase their energy in stages before being injected into the main ring.

First, the hydrogen is passed through an electric field to strip it of its electrons, and the resulting protons are injected into the linear Linac2 accelerator and accelerated to 50 MeV. Then, they are fed into the Proton Synchrotron Booster (PSB), where they are accelerated to 1.4 GeV. Next, the protons make it to the Proton Synchrotron (PS) which pushes them up to 25 GeV. After that, they encounter the Super Proton Synchrotron (SPS) and reach and energy of 450 GeV. Finally, they are injected into the main LHC ring at Points 2 and 8 where they are accelerated up to the desired

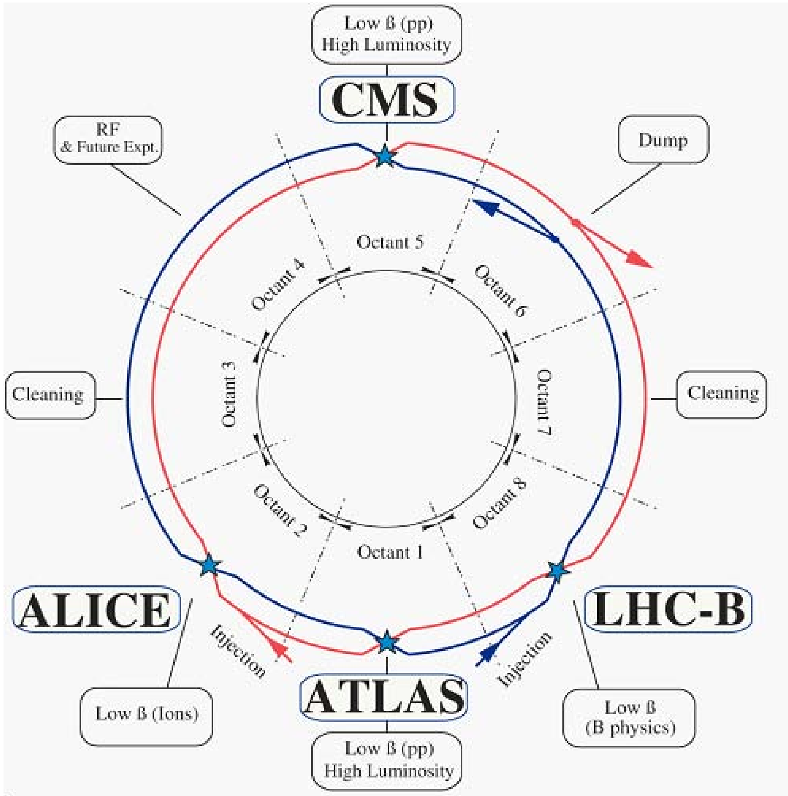

Figure 3.2: A bird's eye view of the experiments around the LHC ring. The direction of Beam 1 is clockwise and shown in red; the direction of Beam 2 is counter clockwise and shown in blue. ATLAS is located at Point 1, ALICE at Point 2, CMS at Point 5, and LHCb at Point 8.

center of mass energy (8 TeV in 2012). To accelerate the protons from 450 GeV to 8 TeV, takes approximately 20 minutes and the beams are circulated from 5 to 24 hours. The injection chain at the LHC is shown in Figure 3.3.

The fine structure of the beam can be see in Figure 3.4. Each LHC beam has 39 batches that consist of 3 or 4 trains. These trains each consist of 72 25-ns spaced bunches each, which corresponds to 2808 total bunches. At the end of each train, there is a gap that corresponds to 200 ns or 8 bunches, which allows for the SPS injection kicker rise time. At the end of each batch there is gap of 38 or 39 bunches to allow for the LHC injection kicker rise time. Lastly, after all batches, there is a

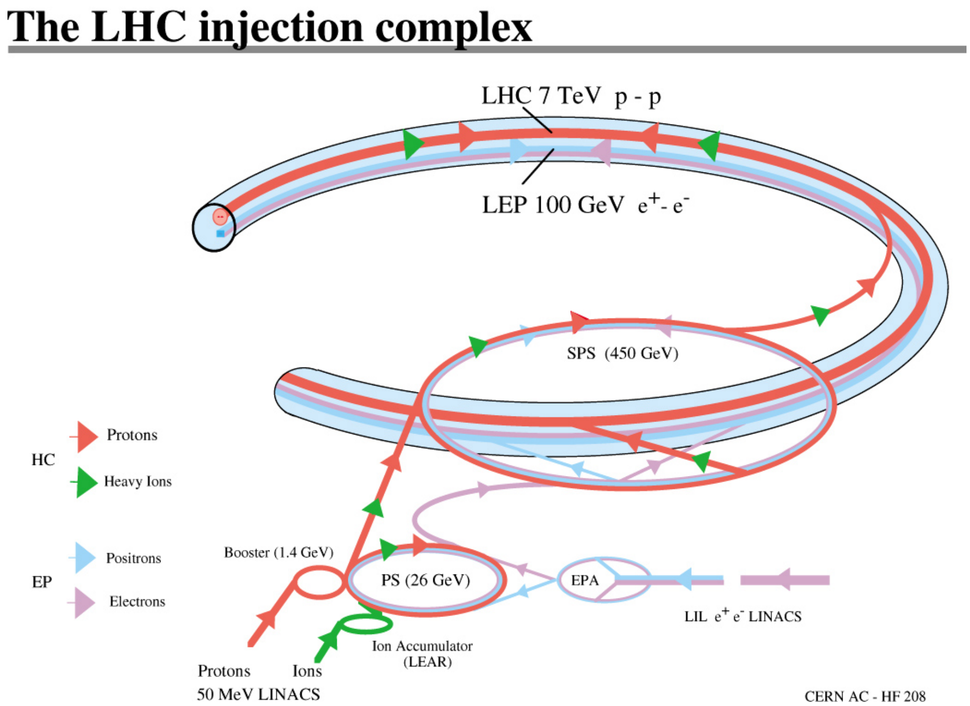

Figure 3.3: Overview of the injection complex at the LHC. [8]

gap of 119 bunches or 2.9 μs which allows for the LHC dump kicker rise time [9].

3.3 LHC Features

3.3.1 Magnets

The LHC has 1 232 twin-bore or 'two-in-one' dipole magnets around the ring to maintain the circular orbit of the protons. They consist of two beam pipes, each with its own set of superconducting coils, and are cooled to temperatures of 2K by superfluid helium and produce a magnetic field of 8 T. The two-in-one design allows for a magnetic field that points either up or down depending on the direction of the beam. Each dipole is $\sim$ 16.5 m long and weighs 27.5 tons. A cross sectional view of the dipole magnets used can be seen in Figure 3.5.

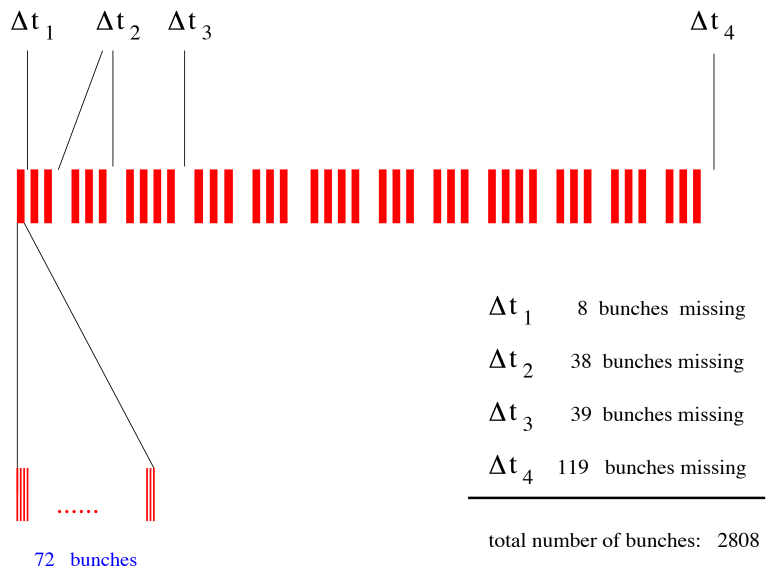

Figure 3.4: Overview of the injection complex at the LHC. [9]

In addition to dipole magnets, the LHC uses several other magnets to focus the beam. Quadrupole magnets as well as other higher order magnets are used to keep the beam from diverging in the plane transverse to its motion. Lastly, the so called 'inner triplets' are the magnets that are responsible for squeezing the beam even more before the collision point. The inner triplets reduce the size of the beam from ~ 0.2 mm to ~ 16 μm.

3.3.2 RF Cavities

The radio frequency (RF) cavities used by the LHC are designed to accelerate the bunches of protons as well as keeping the bunches tight. The RF cavities at the LHC are tuned to 400 MHz, which defines the bunch length to be $\lesssim 2$ ns. There are 8 RF cavities per beam, and as bunches pass through the cavity, the oscillating electric field is at its peak and accelerates the protons through a potential difference of 2 MV. The finite bunch length is ensured since particles that arrive a little later will receive

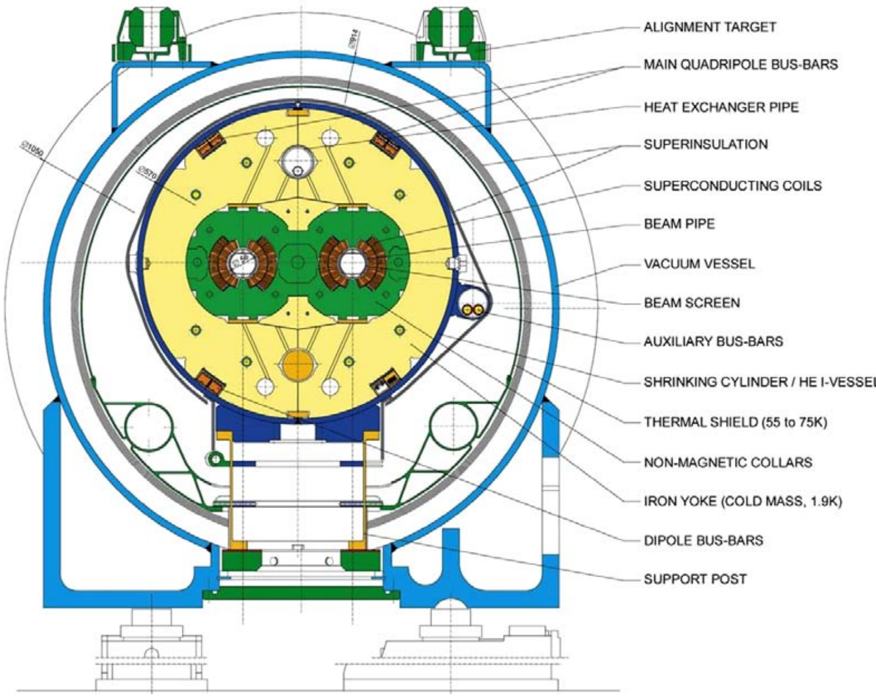

Figure 3.5: Cross sectional view of twin-bore dipole magnets at the LHC.

a slightly higher energy kick and vice versa for those particles that arrive earlier. The 450 GeV protons that arrive in the LHC ring from the SPS get a kick each time they pass through the RF cavities until they have been accelerated to the desired center of mass energy.

3.3.3 Vacuum System

The LHC has three vacuum systems: the insulation vacuum for the cryomagnets, the insulation vacuum for the helium distribution line, and the beam vacuum. The vacuum used for the insulation systems are kept at 10^{-6} mbar. The requirements on the beam vacuum are more strict. For the required beam lifetime and to decrease the background from protons colliding with other particles in the beam pipe, the beam vacuum is kept at 10^{-10}-10^{-11} mbar.

Chapter 4
The Compact Muon Solenoid

The Compact Muon Solenoid (CMS) is located at Point 5 on the LHC ring. CMS was designed to detect all known particles of the SM as well as other particles beyond the standard model (BSM) which have been postulated to exist. It is a general purpose detector, which is 21.6 m long, 14.6 m in diameter, and weighs 13,800 tons. The layout of CMS can been seen in Figure 4.1. It consists of a central barrel, in which the subdetectors are arranged in concentric layers, and outer endcaps, designed to extend the coverage of CMS.

In this section we will give an overview of the features of CMS as they pertain to this search; a more detailed description of CMS can be found in [10]. The coordinate system and subdetectors are described in Section 4.1; the layout of the trigger and how data is acquired is explained in Section 4.2; and how the information for the subdetectors is combined to define physics objects used in analyses is explained in Section 4.3. Unless otherwise noted, the information in this chapter is taken from [10].

4.1 Coordinate System and Detectors

4.1.1 Coordinate System

The coordinate system of CMS is such that the z direction is aligned with the beam, the y direction points upward, and the x axis points towards the center of the LHC

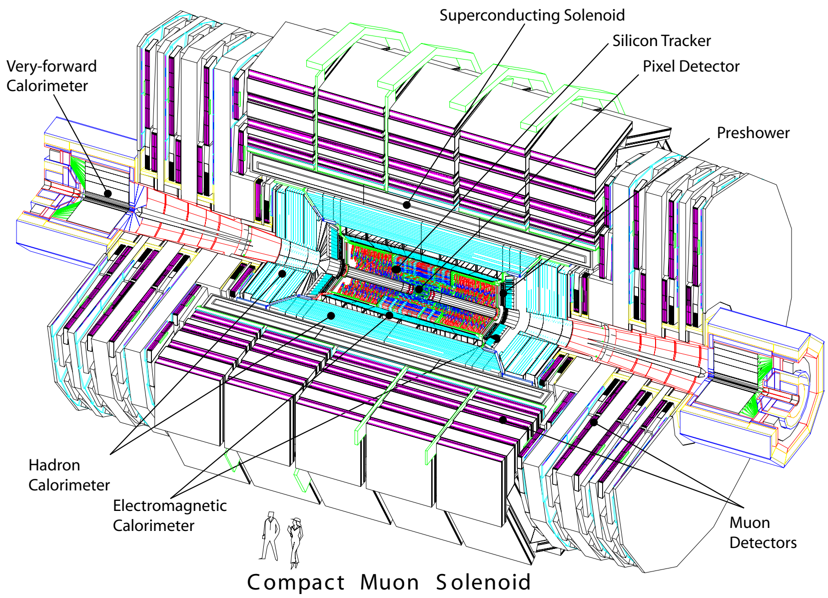

Figure 4.1: Cutaway view of CMS [10].

ring. ϕ is measured as the angle in the transverse $(x - y)$ plane, and θ is the angle measured between the beam line and the transverse plane. However, the pseudorapidity (η) is often used instead of the angle θ, where $\eta = -tan[\ln(\frac{\theta}{2})]$. Since the pseudorapidity is a Lorentz invariant quantity, it is more convenient to use than the polar angle. Now, we can define the momentum and energy transverse to the beam direction: $p_T = pcos\theta$ and $E_T = Ecos\theta$, where p and E are the magnitudes of the momentum and energy vectors. The imbalance of momentum in the transverse plane is denoted by $\not{E}_T$. The CMS coordinate system is illustrated in Figure 4.2.

4.1.2 Tracking System

At the very core of CMS is the tracking system, based entirely on silicon tracking technology. The tracker is designed to provide measurements of trajectories and vertices of charged particles emerging from the collision point. Through the measurement of

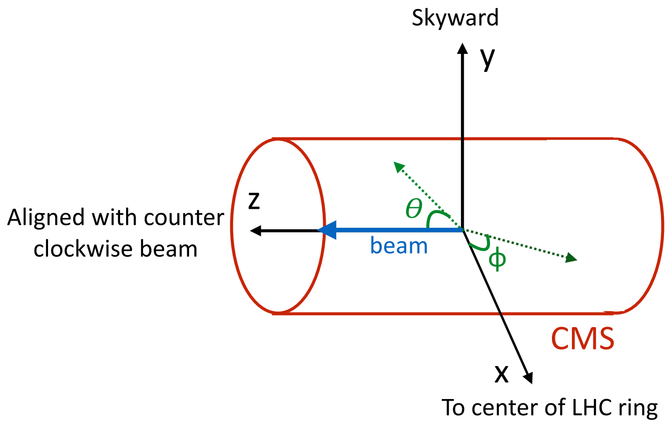

Figure 4.2: Illustration of coordinate system used at CMS [11].

their curvature in the magnetic field, the momenta of the particles can be determined. The tracker uses p-n junctions to detect ionization signals from charged particles that traverse the n-doped and p-doped materials of the silicon sensors. The sensors are reverse biased to obtain a depletion region, or a region with a strong electric field that is free of charge carriers. Thus, when a charged particle crosses the fully depleted sensor, the charge carriers that it releases drift to the anode/cathode. This ionization current, which is proportional to the ionization energy loss of the particle, is then read out by the electronics. The tracker consists of an inner pixel detector and an outer strip tracker. The pixel and strip tracker are complemented by endcaps, extending the pseudo rapidity coverage to $|\eta| < 2.5$.

At the design luminosity of the LHC, we expect approximately 1000 particles resulting from 20 pp interactions every bunch crossing (every 25 ns). Consequently, the flux of particles is largest at $r < 10$ cm. For this reason, the pixel detector was designed to keep the hit occupancy below 1%. This is accomplished with 1440 pixel modules, where each pixel sensor measures 100×150 μm^2. For 20 cm $< r <$ 110 cm, the flux of particles has decreased enough to allow for the use of 15 148 silicon strips, typically ~10 cm× ~100μm.

Pixel Detector

The pixel detector is responsible for the reconstruction of secondary vertices from b or τ decays and providing seed tracks for the outer track reconstruction. It consists of three barrel layers (BPix) at radii of 4.4, 7.3, and 10.2 cm. The barrel has two disks of pixel modules on each side (FPix). There are 66 million pixels in the BPix+FPix. This arrangement provides three hits for each pixel seed over the full pseudorapidity range. Figure 4.3 shows the layout of the pixel detector as well as the efficiency for ≥ 2 hits over the η range. The spatial resolution of the pixel detector must be fine as it is the first measurement of physics objects and has been measured to be $15-20\mu$m.

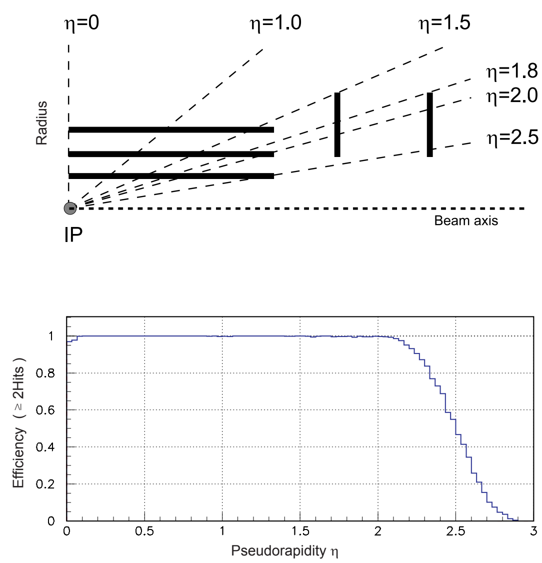

Figure 4.3: The layout of the pixel detector and the hit efficiency as a function of $|\eta|$

.

Strip Tracker

The strip tracker is composed of three different subsystems. First, the Tracker Inner Barrel (TIB) and Tracker Inner Disks (TID) extend from 20 cm $< r <$55 cm and consist of 4 barrel layers + 3 endcap disks at each end. The TIB/TID is surround by the Tracker Outer Barrel (TOB) covering a radius of up to 116 cm. The TOB consists of 6 barrel layers and extends in z between ±118cm. Lastly, the Tracker Endcaps (TEC+ and TEC−, the sign reflects the z axis location) cover 124 cm$< |z| <$282 cm and 22.5 cm$< r <$113.5 cm. Each TEC consists of 9 disks. This combination of subsystems shown in Figure 4.4 ensures at least 9 hits. In addition, the first two layers of the TIB, TID, and TOB as well as rings 1, 2, and 5 of the TEC's have a second micro-strip module mounted on the back at a stereo angle of 100 mrad. These double-sided layers ensure that $\sim$ 4 hits are two-dimensional. The resolution is 230 μm in the TIB, 530μm in the TOB and varies in the TEC.

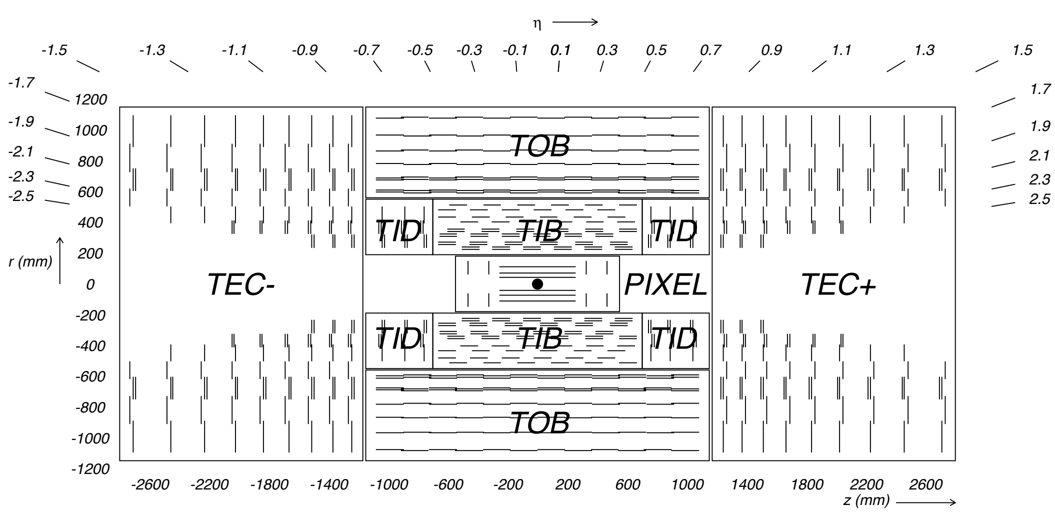

Figure 4.4: Cross section of CMS tracker. Each line is a detector module; double lines indicate back-to-back modules

.

Each silicon strip tracker module consists of one or two silicon sensors supported by a frame of carbon or graphite. A Kapton circuit layer is used to insulate the silicon sensor and provide the electrical connection to the back plane. In the case of two sensors, the strips are connected via wire bonds. Modules in the inner barrel, inner disks and rings 1-4 in the endcaps have one sensor; modules in the outer barrel and rings 5-7 of the endcaps have two sensors. Figure 4.5 shows a sample module with two sensors.

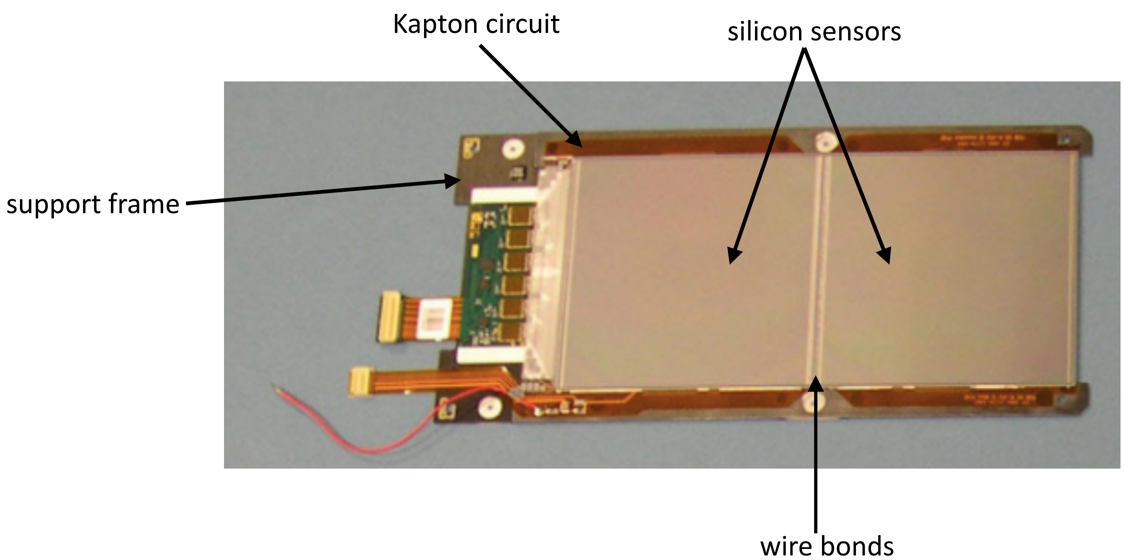

Figure 4.5: Silicon strip tracker module with two sensors [12].

4.1.3 Electromagnetic Calorimeter

Outside of the tracking system is the electromagnetic calorimeter (ECAL). The main purpose of the ECAL is to measure the energy of photons and electrons. High energy electrons predominantly lose energy in matter by bremsstrahlung, and high energy photons lose energy by pair production (the creation of an electron/positron pair). Thus, when a higher energy electron or photon enter the ECAL it will create an electromagnetic (EM) shower.

The ECAL is a hermetic calorimeter, composed of 75,848 lead-tungstate crystals. It consists of a barrel that is closed on each end by endcaps. The barrel covers pseudorapidity of $|\eta| < 1.479$ while the endcaps cover $1.479 < |\eta| < 3.0$. In the barrel, there are 1700 crystals per supermodule, arranged in 20×85 grid in $\phi \times \eta$. Two supermodules are laid end-to-end to form one row in ϕ with 18 rows completing the entire barrel. In the endcap, the remaining 14,648 crystals are divided almost evenly amongst 18 wedge-shaped sectors. In front of each endcap sits the layered preshower composed of a lead absorber followed by silicon detectors. The goal of the preshower is to distinguish between prompt photons and photons that arise from neutral hadron decay. The geometry of the ECAL can be seen in Figure 4.6.

The lead-tungstate crystals of the ECAL were chosen due to their radiation hardness, short radiation length ($X_0 = 0.89$ cm), and small Molière radius (2.2 cm). Since most EM showers can be contained in 20 X_0, a length of 230 mm, which corresponds to $25.8X_0$, for the crystals is used. A particle passing through these crystals will scintillate, and the light emitted will be collected by avalanche photodiodes in the barrel or vacuum photodiodes in the endcaps providing a measure of the particles energy. A sample crystal from the barrel and endcap with these photodetectors attached is shown in Figure 4.7.

The energy resolution, σ_E/E, extracted from 2012 $Z \to ee$ events as a function of η can be seen in Figure 4.8.

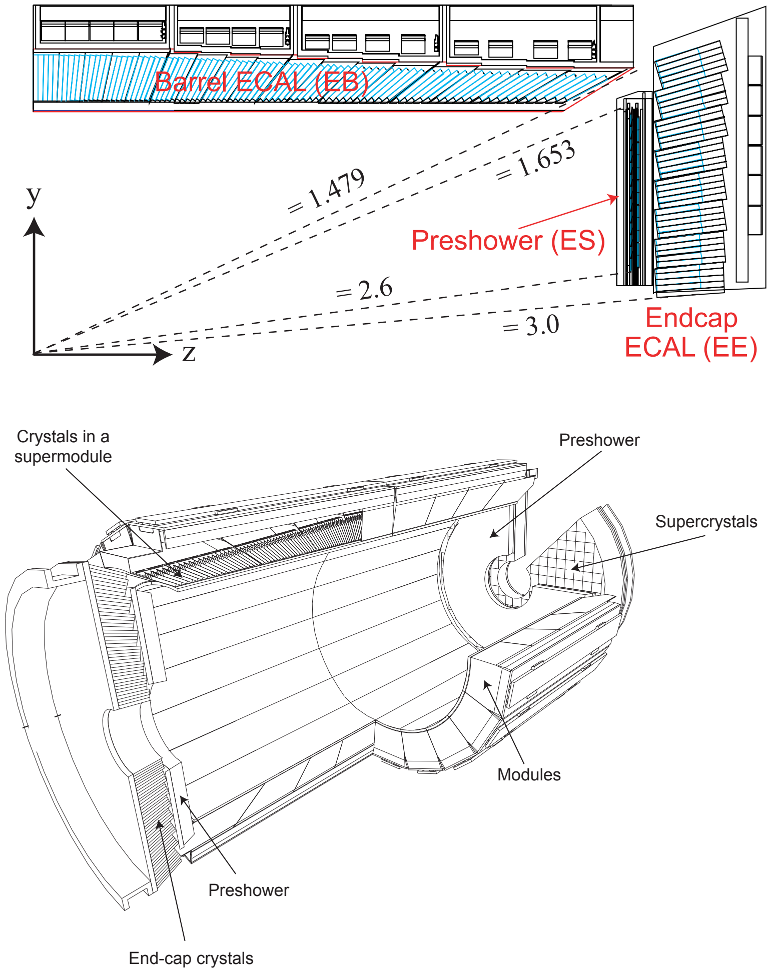

Figure 4.6: Cross sectional view of the ECAL, with η ranges of interest labeled (top). Layout of the ECAL showing the arrangement of modules, supermodules, and endcaps preceded by the preshower (bottom)

.

4.1.4 Hadronic Calorimeter

Outside of the ECAL is the hadronic calorimeter (HCAL). The HCAL is designed to reconstruct the energy of hadrons. A strongly interacting hadron will produce a hadronic shower in the HCAL through a series of inelastic nuclear interactions. By combining the information from the ECAL and HCAL, we have enough information

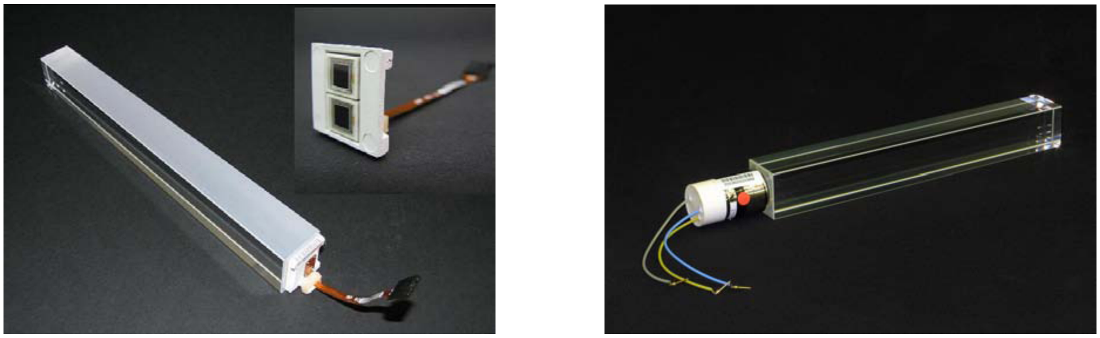

Figure 4.7: Barrel crystal with avalanche photodiode (left). Endcap crystal with vacuum photodiode (right)

.

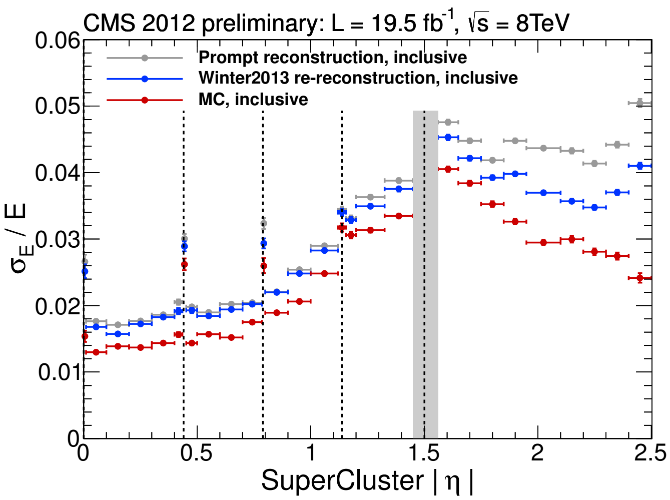

Figure 4.8: ECAL energy resolution, σ_E/E, from 2012 $Z \rightarrow ee$ events as a function of η. The vertical dashes represent cracks between the ECAL supermodules, and the gray band represents the barrel-endcap crack region. The energy resolution is degraded in these areas [13].

.

to determine the $\not{E}_T$ of the event, caused by neutral or weakly interacting particles that do not interact with the material in CMS.

The HCAL consists of the HCAL barrel (HB), HCAL endcaps (HE), HCAL outer

(HO), and HCAL forward (HF) as shown in Figure 4.9. Like the barrel of the ECAL,

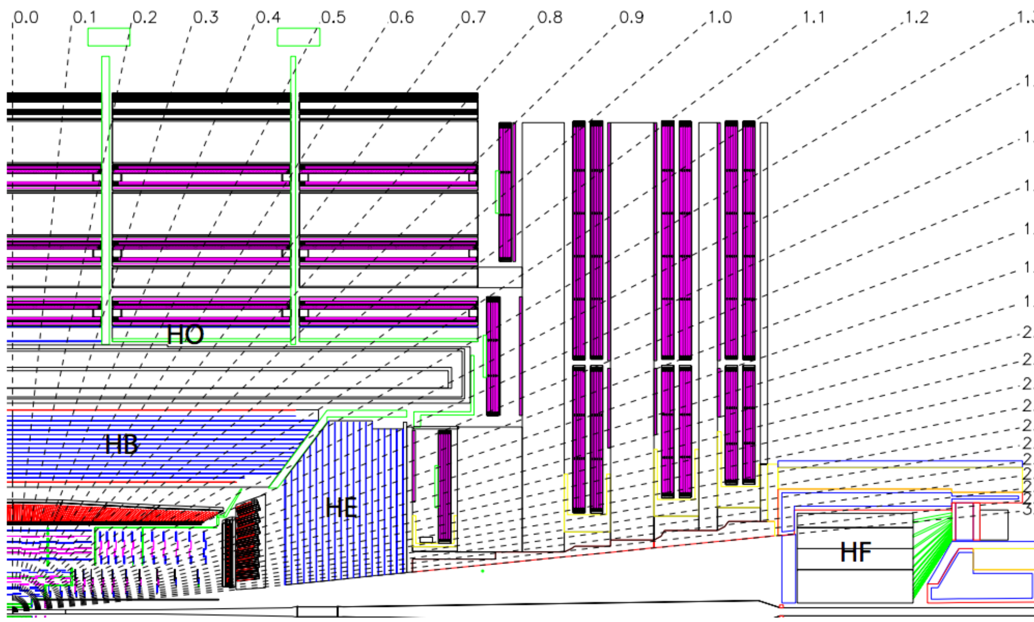

Figure 4.9: Quarter cross sectional view of HCAL

.

HB is made of 36 ϕ-wedges. Each wedge is divided into 16 along η and 4 along ϕ, yielding 64 readout towers per wedge. HE also has 36 ϕ-wedges with 38 readout towers each. Lastly, HO consists of 5 rings around HB and HE with 72 ϕ-slices per ring. HFs are positioned 11.2 m from the interaction point and are able to measure the energy of very high rapidity hadronic activity. HB, HE, and HO are sampling calorimeters consisting of alternating brass absorbers and plastic scintillators. In brass, the nuclear interaction length is 16.42 cm. Since the HCAL is ~ 9 nuclear interactions in length, 99% of the shower will be contained. The brass absorber initiates the hadronic shower and as the particles travel through the plastic scintillator, the light is read out by wavelength-shifting fibers which are connected to scintillator tiles. The light output from all tiles in a readout tower is collected and read out by hybrid photodiodes.

4.1.5 Superconducting Magnet

As the namesake of CMS implies, it was designed to measure the momentum of muons with high efficiency. This was accomplished with the choice of a superconducting solenoid, which sits just outside the calorimeter subsystems. The large bending power aids in accurately determining the momentum of muons and other charged particles.

The magnet is 12.5 m in length and 6 m in diameter and was designed to generate a uniform magnetic field of 4 T. The flux is returned by a 10,000 ton iron yoke. The return yoke is interleaved with the muon system (discussed in the next section). This setup concentrates the return field within the volume of the muon system to provide a second handle on measuring the momenta of high energy muons.

4.1.6 Muon System

Once outside the magnet, all particles with the exception of muons should have been stopped by the other subsystems. At CMS, the accurate detection of muons is of the utmost importance as muons provide a clean, distinct signature of interesting physics phenomena.

Muons that traverse CMS are measured by three different gaseous detectors: drift tubes (DTs), cathode strip chambers (CSCs), and resistive plate chambers (RPCs). Since the magnetic field is uniform within the barrel, DTs are employed in four stations and cover $|\eta| <1.2$. In each endcap, where the magnetic field is changing, 4 CSC stations are used to identify muons with $0.9 < |\eta| < 2.4$. The RPCs, present in both the barrel and the endcap are used to provide accurate first level trigger information with a timing resolution of approximately 1 ns. A cross sectional quarter view of the muon system is shown in Figure 4.10.

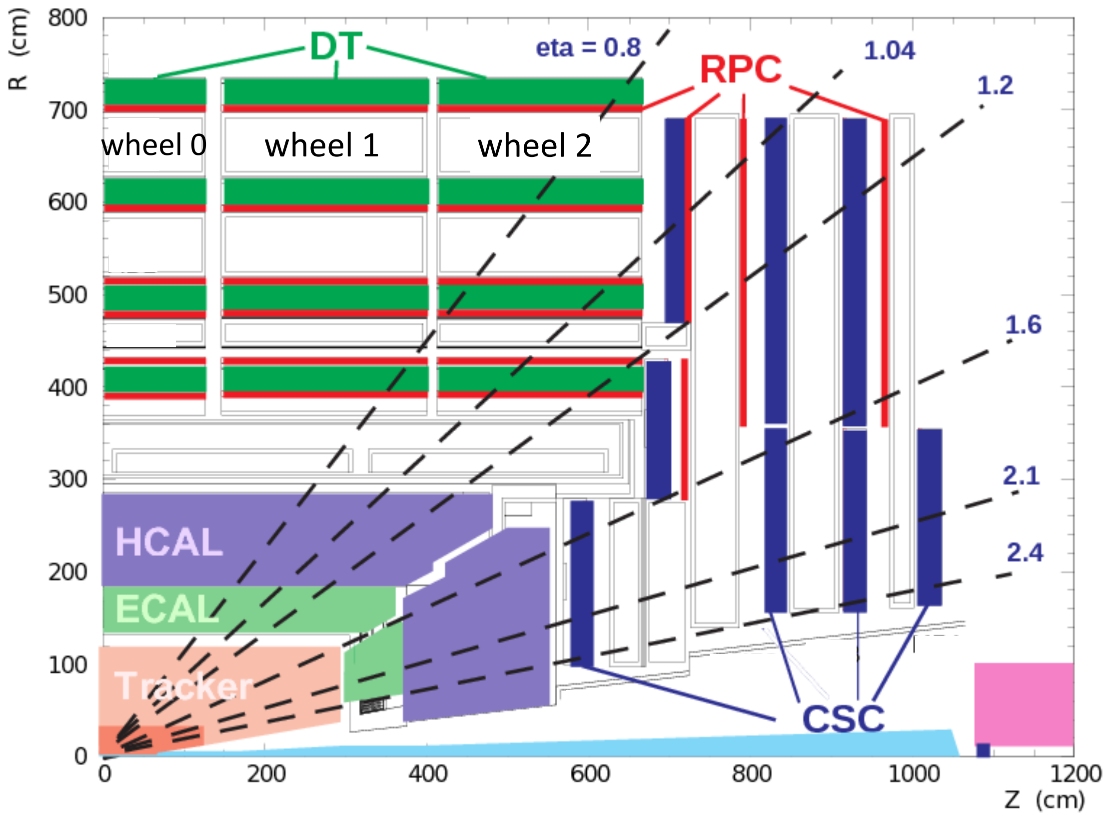

Figure 4.10: A cross sectional quarter view of the muon system of CMS [14].

.

Each DT is 2.4 m in length and 13 mm × 42 mm in cross section. It is filled with a gas mixture that is 85% Ar and 15% CO_2. An anode wire at 3600 V runs along the length of tube and and the walls are covered by electrodes held at $\sim$ 1500 V. When a muon passes through the tube, it ionizes the gas atoms. The freed electrons drift in the electric field to the anode, which is read out. The maximum drift time is 380 ns.

Each CSC consists of alternating layers of cathode strips and anode wires, and the space between two successive planes is filled with a 40% Ar, 50% CO_2, and 10% CF_4 gas mixture. A muon passes through, ionizing the gas atoms, and positive ions drift toward the anode and are read out as in the DTs. However, the induced charge on the cathode strips is also read out providing an additional measurement.

The muon reconstruction efficiency for simulated single muon events is shown in Figure 4.11 is 95-99%. The efficiency drops in regions of $|\eta| = 0.25$ and 0.8, the region between 2 DT wheels, and $|\eta| = 1.2$, the transition between the DT and CSC systems.

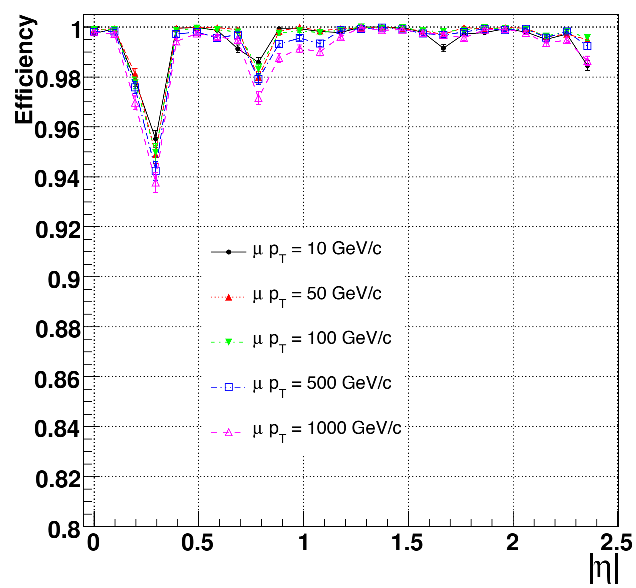

Figure 4.11: Muon reconstruction efficiency as a function of η for selected p_T values

.

4.1.7 Summary

The arrangement of subdetectors in CMS and their general purposes are summarized in Figure 4.12. This combination of technologies is chosen to reconstruct all particles with high efficiency. All particles produced in the primary collision will travel through the silicon tracker. The trajectory and momentum of charged particles will be measured here. Once outside the tracker, photons and electrons will produce an electromagnetic shower in the ECAL and stop, providing a measure of their energy. Charged and neutral hadrons will continue through the ECAL and produce a hadronic shower in the HCAL, providing a measure of their energy. Lastly, muons will continue through the HCAL, superconducting solenoid, and be detected by the muon system. Any particles not detected by these subdetectors of CMS (neutrinos or other neutral and weakly interacting particles) will leave an imbalance of energy in the transverse plane and be determined as $\not{E}_T$.

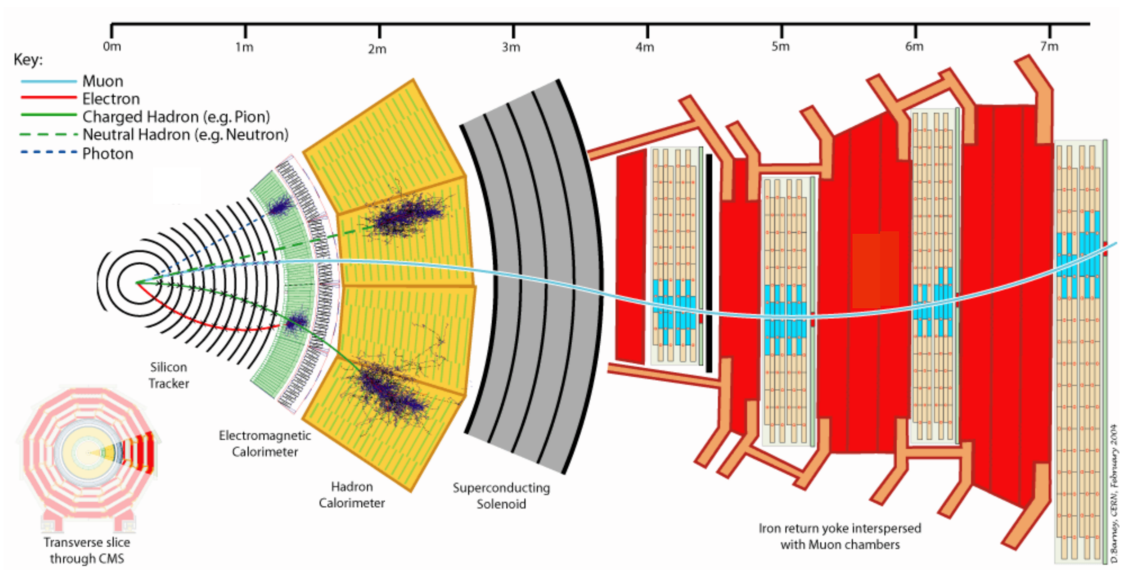

Figure 4.12: A transverse slice of CMS. All particles produced will travel through the silicon tracker. The tracker will measure the trajectory of charged particles and reconstruct the momenta. Next, photons and electrons will shower in the ECAL and deposit all of their energy. Hadrons will continue through the ECAL and produce hadronic showers in the HCAL. Muons will not be stopped by the ECAL or HCAL and will continue through the magnet to the muon system. [15]

.

4.2 Triggers and Datasets

Since it is impossible to store and analyze all events that are produced at CMS, a drastic reduction in the recorded number of events must be implemented before the data even reaches the analysts. The trigger is the first stage of event selection and cuts down the rate from 40 MHz to 300 Hz. The rate is reduced in two steps: the Level 1 (L1) trigger and then the High Level Trigger (HLT).

4.2.1 Level 1 Trigger

The L1 trigger is based on hardware and must analyze every single event that is collected by CMS. The L1 trigger has 3.2 μs after a given bunch crossing to decide whether or not to pass an event to the HLT. A schematic of the L1 architecture can be seen in Figure 4.13.

To begin, deposits in the calorimeters and/or hits in the muon system seed the Trigger Primitive Generators (TPGs). The seeded TPGs are used to calculate the E_T sums from the calorimeters and the muon track stubs, which are combined into Regional Calorimeter Triggers or muon track finders, respectively. These are then sorted based on p_T and quality. Next, the regional information is combined to form the Global Calorimeter and Global Muon Triggers. Once the Global Calorimeter and Global Muon triggers have determined the best physics object across the detector, they are finally combined into a single Global Trigger. The Global Trigger then decides if that event will be kept and further analyzed by the HLT or if it will be discarded.

4.2.2 High Level Trigger

The HLT examines all events that have passed the L1 trigger and determines whether or not they will be saved for physics analyses. Due to timing and storage constraints

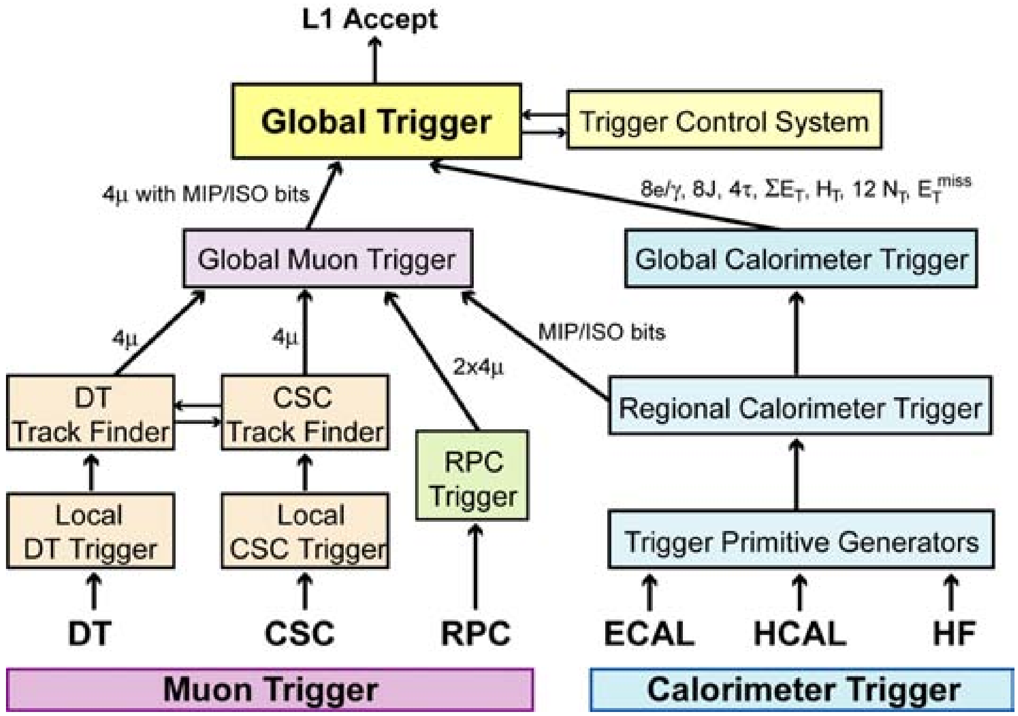

Figure 4.13: Schematic of the L1 trigger architecture.

.

the rate must be kept to approximately 300 Hz.

The HLT is designed to accept a broad range of physics events to allow for new physics phenomena. In addition, the objects within the events accepted must have a high selection efficiency with respect to the offline reconstruction of physics objects. These goals must be accomplished within the limits of computing speed and storage. To accomplish this, the HLT paths are designed to look for a minimal number of physics objects, for example, events that have only one muon. Also, the HLT algorithm will only reconstruct objects in certain regions of the detector. These regions are determined using the information from L1. Since not all objects in the event are reconstructed, the HLT conforms to the technological limitations of CMS. Each HLT path is specific to the analysis being performed; the HLT paths chosen for this search are discussed in Section 5.2.

4.2.3 Data Processing

All events recorded by the HLT are then grouped into different datasets. Each dataset contains events that pass similar HLT paths, i.e. all events that contain one muon are grouped into the `SingleMu` dataset and so forth. These datasets are then subject to several layers of data processing. The first layer of processing produces data in the RAW format. The RAW data contains the readout information from each channel of the detector, the digitized trigger primitives, and the L1 decision. It is the largest data format corresponding to $\sim$1.5 MB per event.

The next layer produces RECO data which produces the high level physics objects i.e. electrons, photons, muons, tracks, etc. It takes up much less space at $\sim$0.5 MB per event. Lastly, the analysis object data (AOD) format is a slimmed d own version of the RECO data. It keeps most information of the RECO data format, but drops the individual channel information if it is not directly related to the physics object. For the purposes of this search, the AOD format contains all event content that we need.

4.3 Object Reconstruction

In the search detailed in the remaining chapters of this thesis, the accurate reconstruction and identification of particles is crucial. Event reconstruction is the process of determining the original particles that passed through CMS, their momenta, directions, and the primary vertex (collision point) of the event. CMS uses a sophisticated algorithm, Particle Flow (PF), that attempts to build a complete description of each event within CMS. PF does this by linking the individual elements of the event (tracks, calorimeter deposits) together to identify all stable particles in the event, i.e.

electrons, muons, photons, charged hadrons, and neutral hadrons [50, 51].

4.3.1 Elements of Particle Flow

Each particle is identified using a combination of information in the event: tracks from charged particles in the tracker, the energy deposited in the calorimeters, and hits in the muon system. These building blocks used by PF must perform with high efficiency. The elements of PF that we will discuss are the iterative tracking algorithm used for track reconstruction and the calorimeter clustering algorithms implemented by CMS.

Track Reconstruction

The iterative tracking strategy [52] was chosen to reconstruct all tracks in the event with high efficiency. Iterative tracking is defined by reconstructing the tracks in the events with several steps or iterations. It begins by reconstructing the highest quality tracks in the event since they are the easiest to identify. Then, the hits associated with that track are excluded from the next iteration. The algorithm used by CMS consists of 6 iterations. In Iteration 0, the highest quality tracks are identified as those that have high p_T, are consistent with the primary vertex, and contain three pixel hits (indicating the track went through every layer of the pixel detector). In Iteration 1, any remaining prompt tracks with only two pixel hits are reconstructed. Iteration 2 picks up tracks that originate from the primary vertex but have low p_T. These first three iterations reconstruct prompt tracks from muons with 99.5% efficiency and charged hadrons with 90%. Lastly, Iterations 3-5 reconstruct the tracks that are not consistent with resulting from the primary vertex.

Each iteration consists of 4 steps.

1. Seed generation: A seed is defined as two or three hits in the pixel detector and

is used to make an initial estimate of the trajectory parameters, i.e. track p_T and position.

2. Track Finding: Multiple trajectories, consistent with extrapolating from the seed trajectory, are built using the collections of hits in the subsequent layers of the tracker. A single trajectory is chosen as the candidate track based on the track quality score, $Q = BN_{\text{found}} - PN_{\text{lost}} - \chi^2$, where N_{found} is the number of hits associated to the trajectory, N_{lost} is the number of layers between the first and last hit in which a hit is expected but not found (missing hits after the last hit on the trajectory are not included), B is a valid hit bonus set to be equal to 5, P is a missing hit penalty set to be equal to 20, and χ^2 is taken from the fit of all the hits associated to the trajectory. The trajectory with the highest quality score Q is chosen as the candidate track.

3. Track Fitting: After the candidate track has been determined in the track-finding stage, it is refitted to get a final estimate of the trajectory parameters. Also, a check is done to see if any spurious hits have been associated to the track; these outliers are removed from the track in this step.

4. Track Selection: If the track does not meet certain quality criteria, it is discarded. The track quality criteria include requirements on the number of layers a track passes through, the χ^2 of the track, and its impact parameters.

Calorimeter Clustering Algorithm

The next main building block of PF is the calorimeter clustering algorithm. It is designed to detect and measure the energy associated with photons and neutral hadrons, separate the energy from neutral particles and charged hadrons, reconstruct the energy of electrons including their associated bremsstrahlung photons, and determine the energy for charged hadrons.

In the ECAL, the energy from photons and electrons deposited in the crystals is determined using a pattern recognition algorithm. A search is performed for ECAL crystals with high energy; these are the seed clusters. The seed thresholds are 60 MeV in the barrel of the ECAL and 300 MeV in the endcap. From the seed, scans are performed in η and ϕ, and the energy from the neighboring cells is added to the energy of the seed. When a crystal with a higher energy than the initial seed is found, the clustering algorithm stops. In the case of unconverted photons or electrons that do not bremsstrahlung photons, 94% of the energy is contained in a 3×3 array of ECAL crystals and 97% in a 5×5 array. For converted photons and the photons that result from bremsstrahlung of electrons, the energy is spread along in ϕ. These clusters are associated to each other and clusters of clusters or superclusters are formed. The superclusters are then associated to the original electron or photon [53].

In the HCAL a similar seeding algorithm is used which looks for towers above a given threshold, 800 MeV. However, the energy from the neutral and charged hadrons used to form jets is reconstructed using the anti-k_T algorithm. This algorithm combines pairs of particles based on the distance between each other and the distance to the beamline. For a given collection of particles, these two distances are computed. If the distance between the two objects is smaller than the distance to the beamline, that object is considered as part of the jet. This process is repeated until the distance between two objects becomes greater than the distance to the beamline [54].

4.3.2 Physics Objects

Once the aforementioned basic elements of PF have been determined, those elements are linked together to describe a single particle.

As an electron traverses the CMS detector, it will ionize and leave tracks in the tracker as well as producing a shower in the ECAL. Therefore, an electron is identified as a charged-particle track and the ECAL energy clusters associated to that track after it has been extrapolated to the ECAL. Any possible photons resulting from bremsstrahlung are also associated to the electron. These electrons can stem either from photon conversion in the tracker material or from the decays of other particles. Photons behave similarly to electrons; however they do not leave a track in the tracker. Consequently, they are identified as those ECAL energy clusters which cannot be linked to any extrapolation of charged-particle tracks to the ECAL.

Since muons do not bremsstrahlung as often as electrons, they will travel through the ECAL without showering. Similarly, muons are not strongly interacting so they will aslo travel through the HCAL into the muon system. Thus, muons are identified as a track in the central tracker consistent with either a track or several hits in the muon system, and they must be associated with an energy deficit in the calorimeters.

Next, charged hadrons are identified as charged particle tracks which are not identified as electrons or muons. Finally, neutral hadrons are identified as HCAL energy clusters not linked to any charged hadron trajectory, or as ECAL and HCAL energy excesses with respect to the expected charged hadron energy deposit.

The identification of the particle plays an important role in the determination of the particle's direction and energy. The energy of photons is directly obtained from the ECAL measurement, corrected for zero suppression effects. The energy of electrons is determined from a combination of the track momentum at the main interaction vertex, the corresponding ECAL cluster energy, and the energy sum of all bremsstrahlung photons attached to the track. The energy of muons is obtained from the corresponding track momentum. The energy of charged hadrons is determined from a combination of the track momentum and the corresponding ECAL and HCAL energy, corrected for zero-suppression effects and for the response function of the calorimeters to hadronic showers. Finally, the energy of neutral hadrons is obtained from the corresponding corrected ECAL and HCAL energy.

For each event, the charged and neutral hadrons are groups into hadronic jets. The resulting jets are clustered using the anti-k_{t} algorithm [54], operated with a size parameter R of 0.5. The jet momentum is determined as the vectorial sum of all particle momenta in this jet, and is found in the simulation to be within 5% to 10% of the true momentum over the whole p_T spectrum and detector acceptance.

Lastly, any imbalance in the E_T of the event from neutrinos or other weakly interacting particles is accounted for. The missing transverse energy $\not\!\!E_T$ is defined as the magnitude of the vector sum of the p_T of all PF candidates reconstructed in the event.

Chapter 5
Data and Monte Carlo Samples

5.1 Data Samples

We conduct the search for disappearing tracks, i.e. those events that yield the experimental signature discussed in Section 2.5, using the `MET` data samples listed in Table 5.1. In addition, the `SingleElectron` and `SingleMu` data samples listed in Table 5.2 are used in the background predictions and assessments of their associated uncertainties. These will be discussed in detail in Chapter 8.

Table 5.1: `MET` data samples in which the search is performed.

Dataset	Integrated luminosity (fb^{-1})
`/MET/Run2012A-22Jan2013-v1/AOD`	0.686
`/MET/Run2012B-22Jan2013-v1/AOD`	4.412
`/MET/Run2012C-22Jan2013-v1/AOD`	7.055
`/METParked/Run2012D-22Jan2013-v1/AOD`	7.366
`MET`	19.5

Table 5.2: Single lepton data samples used to estimate the backgrounds.

Dataset	Integrated luminosity (fb^{-1})
/SingleElectron/Run2012A-22Jan2013-v1/AOD	0.875
/SingleElectron/Run2012B-22Jan2013-v1/AOD	4.37
/SingleElectron/Run2012C-22Jan2013-v1/AOD	7.04
/SingleElectron/Run2012D-22Jan2013-v1/AOD	7.4
SingleElectron	19.7
/SingleMu/Run2012A-22Jan2013-v1/AOD	0.876
/SingleMu/Run2012B-22Jan2013-v1/AOD	4.41
/SingleMu/Run2012C-22Jan2013-v1/AOD	7.05
/SingleMu/Run2012D-22Jan2013-v1/AOD	7.36
SingleMu	19.7

5.2 Triggers

Choosing a trigger to record these events is not straightforward. Since there is no tracking information available at L1, it is not possible for CMS to implement a dedicated disappearing track trigger path that focuses on the partial reconstructed track of the chargino. In the absence of tracking information, one can use the energy in the calorimeters as a trigger option; however, the neutral, weakly interacting neutralinos do not deposit significant energy in the calorimeters. In addition, these BSM particles are mainly produced in pairs, which causes their transverse momenta to cancel. This leaves too little $\not\!\!E_T$ in the event to provide a viable trigger option.

For these reasons, we exploit ISR (initial state radiation) in which the dichargino system recoils against the p_T of the ISR jet. The $\not\!\!E_T$ in this event is proportional to the p_T of the dichargino system and to the p_T of the ISR jet.

Therefore, we conduct the search using events that pass the logical OR of the following triggers:

- HLTMonoCentralPFJet80_PFMETnoMu95_NHEF0p95,
- HLTMonoCentralPFJet80_PFMETnoMu105_NHEF0p95, or
- HLT_MET120_HBHENoiseCleaned.

The HLTMonoCentralPFJet80_PFMETnoMu105_NHEF0p95 trigger requires at least one PF jet with $p_T > 80$ GeV and $|\eta| < 2.6$. The requirement that the fraction of the jet energy assigned to neutral hadrons in the electromagnetic calorimeter (ECAL) be less than 95% is applied to all jets in the event. Lastly, PFMetNoMu must be larger than 105 GeV, where PFMetNoMu is the particle flow $\not{E}_T$ calculated excluding the p_T of any muons in the event.

The HLTMonoCentralPFJet80_PFMETnoMu95_NHEF0p95 trigger has the same requirements as the previous trigger, but it places an additional requirement on jets in the event, i.e., should a subleading jet exist in the event with $p_T > 50$ GeV, then the difference in azimuthal angle between the leading jet and the subleading jet must be less than 2.9. Also, the threshold for PFMetnoMu is slightly lower (95 GeV). The 95 GeV threshold was in place during the 2012A and 2012B run periods, while the 105 GeV threshold was set for the 2012C and 2012D run periods.

The HLT_MET120_HBHENoiseCleaned requires that CaloMet be larger than 120 GeV and passes the HBHENoise filter, which reduces false $\not{E}_T$ from noise in the HCAL.

In addition, the following single lepton trigger paths are used for the validation and estimation of backgrounds in this search:

- HLT_IsoMu24_eta2p1 used in SingleMu
- HLT_Ele27_WP80 used in SingleElectron

The HLT_IsoMu24_eta2p1 trigger requires at least one, isolated muon with $p_T >$ 24 GeV and $|\eta| < 2.1$.

The HLT_Ele27_WP80 trigger requires at least one electron with $p_T > 27$ GeV and a working point (WP), or electron identification efficiency, of at least 80%.

5.3 Background Monte Carlo Samples

To study the backgrounds, we use simulated samples of the following standard model (SM) processes: W + jets, $t\bar{t}$, Z$\rightarrow$ $\ell\ell$ ($\ell = e, \mu, \tau$), Z$\rightarrow$ $\nu\nu$; WW, ZZ, WZ, Wγ, and Zγ boson pair production; and QCD multijet and single-top-quark production. The W + jets and $t\bar{t}$ are generated using MadGraph 5 [55] and pythia 6 [56] event generators, while single top production is modeled using powheg [57–60] and pythia 6 event generators. The Z$\rightarrow$ $\ell\ell$, boson pair productions, and QCD multijet events are simulated using pythia 6. All samples are simulated with CTEQ6L1 parton distribution functions (PDF). The full detector simulation with Geant4 [61] is used to trace particles through the detector and to model the detector response. A detailed list of these MC samples can be found in Appendix A.

In addition, we have generated several single particle samples to aid in the studies of various backgrounds. They are listed in Table 5.3.

Table 5.3: Particle gun samples.

Type	Purpose	p_T (GeV)	$\lvert\eta\rvert$	Number of Events
pion	study tau background	30	< 2.5	10,000
muon (narrow-η)	study sources of missing outer hits	100	< 0.8	3,000
muon (wide-η)	study muon inefficiency	100	< 1.4	1,000,000

5.4 Signal Monte Carlo Samples

Signal samples are simulated with pythia 6 for the processes $q\bar{q}' \rightarrow \chi_1^{\pm}\chi_1^0$ and $q\bar{q} \rightarrow \chi_1^{\pm}\chi_1^{\mp}$ in the AMSB framework. The SUSY mass spectrum in AMSB is determined by four parameters: the gravitino mass $m_{3/2}$, the universal scalar mass m_0, the ratio of the vacuum expectation values of the Higgs field at the electroweak scale $\tan\beta$, and the sign of the higgsino mass term $\mathrm{sgn}(\mu)$. Of these, only $m_{3/2}$ significantly affects the chargino mass. For this reason, we produce samples with variations of the $m_{3/2}$ parameter that correspond to chargino masses between 100 and 600 GeV. Supersymmetric particle mass spectra are calculated according to the SUSY Les Houches accord [62] with ISAJET 7.80 [63] event generator. Table 5.4 lists the SUSY parameters for the simulated samples. The branching fraction of the $\chi_1^{\pm} \to \chi_1^0\pi^{\pm}$ decay is

Table 5.4: Signal MC parameter points. Each mass point is simulated with chargino $c\tau$ of 10, 100, and 1000 cm.

m_0 (GeV)	$m_{3/2}$ (TeV)	$\tan\beta$	$\mathrm{sgn}(\mu)$	$m(\chi_1^{\pm})$ (GeV)	$\Delta(m)$ (GeV)
1500	35.1	5	+1	100.0	0.19
1500	68.9	5	+1	200.0	0.17
1500	103.7	5	+1	300.0	0.17
1500	139.0	5	+1	400.0	0.17
1500	174.4	5	+1	500.0	0.17
1500	210.3	5	+1	600.0	0.17

set to 100%. While the chargino mean proper lifetime ($c\tau$) is uniquely determined by the four parameters above, the simulation is performed with a variety of mean proper lifetime values ranging from 0.3 to 300 ns to expand the search beyond the AMSB scenario. These intermediate lifetimes are obtained by reweighting events according to exponential PDF's for the generated and target $c\tau$.

Chapter 6
Event Selection

In this chapter, we list several sets of criteria which define samples used in various aspects of the analysis. These samples are used to isolate signal events, study the various sources of background, estimate the background, and assess the uncertainties associated with the background estimates.

To eliminate backgrounds that arise fron non-collision data, all samples are first required to pass the standard CMS cleaning criteria. These criteria ensure that each analyzed event contains a good interaction vertex. Also, they ensure that if an event contains a large number of tracks, at least 10% of them are of the highest quality. The CMS cleaning criteria are:

- $vtx^{primary}$ with ≥ 4 d.o.f.
- $z^{primary}_{vtx}$ displaced from $z = 0$ by no more than 24 cm in z
- $d^{primary}_{vtx}$ displaced from $(x, y) = (0, 0)$ by no more than 2 cm in xy
- In events with ≥ 10 tracks $\geq 10\%$ must be classified as "high purity" as in [64].

6.1 Search Sample

Events in the search sample are characterized as those that contain at least one prompt, well-reconstructed track with little or no associated calorimeter energy and a large number of missing outer hits, i.e. those events with the signature of a disappearing track. Events collected by the `MET` trigger paths listed in Section 5.2, passing the event cleaning criteria listed above, and that pass the additional selection criteria described below comprise the search sample. The search sample contains two overlapping subsamples:

- A background dominated control region, referred to as the *Candidate Track* subsample
- A signal enriched region where the search for BSM events is performed, referred to as the *Disappearing Track* subsample. The *Disappearing Track* subsample is a subset of the *Candidate Track* subsample.

The criteria that define these subsamples are listed in the following subsections. The separation of signal and background provided by each of the criteria as well as the qualitative motivation for the specific value of the cut that is applied, is illustrated by "N-1" plots (or in one case N-2) in which all criteria save for the variable(s) being plotted are applied. In all such plots, the signal and MC samples (normalized to unit area) described in Section 5.3 and 5.4 are used.

6.2 Candidate Track Subsample

We define the *Candidate Track* subsample as events which pass the *Candidate Track* criteria described below. These criteria isolate well-reconstructed, prompt tracks with large transverse momentum and suppress lepton backgrounds. The *Candidate Track* criteria are:

- $\not{E}_T > 100$ GeV, near the trigger threshold, to maximize the signal acceptance, as shown in the N-1 plot in Figure 6.1.

- $\geq$ 1 jet with p_T > 110 GeV and $|\eta|$ < 2.4 that meets several noise cleaning criteria: less than 70% of its energy assigned to neutral hadrons or photons, less than 50% of its energy associated with electrons, and more than 20% of its energy carried by charged hadrons. These noise cleaning criteria eliminate unsimulated sources of background [65]. The trigger efficiency as a function of the p_T of the leading jet is $\sim$ 100% for jet p_T > 110 GeV [65].

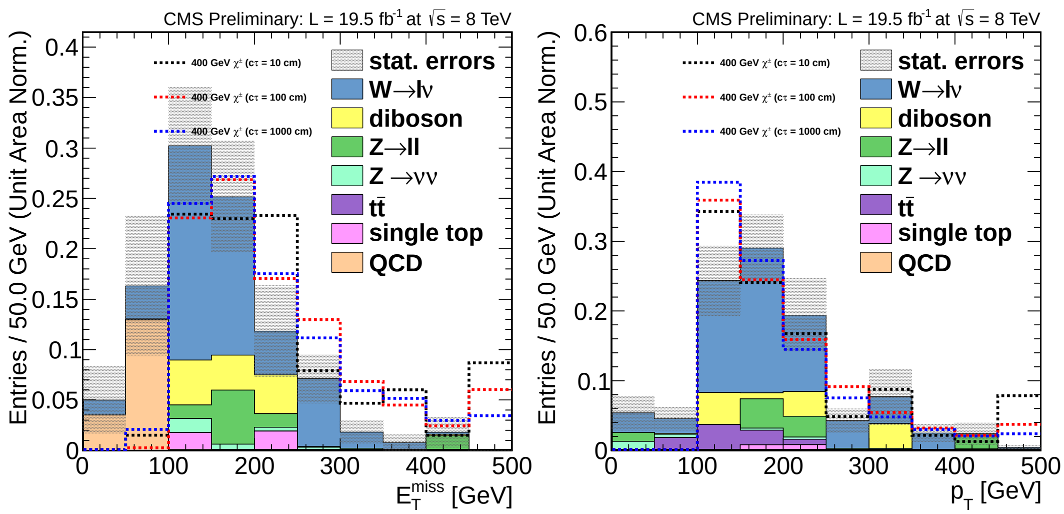

Figure 6.1: Distribution of $\not\!\!E_T$ (left) and leading jet p_T (right) after all other (N-1) *Candidate Track* criteria. We require $\not\!\!E_T$ > 100 GeV and the jet to have p_T > 110 GeV.

- Additional jets with p_T > 30 and $|\eta|$ < 4.5 are accepted, provided they meet two additional criteria. The difference in azimuthal angle, $\Delta\phi$(dijet), between any two jets in the event must be less than 2.5. The minimum $\Delta\phi$ between the $\not\!\!E_T$ vector and either of the two highest-p_T jets is required to be greater than 0.5. These additional jet criteria suppress QCD background, as shown in the N-2 and N-1 plots in Figure 6.2.

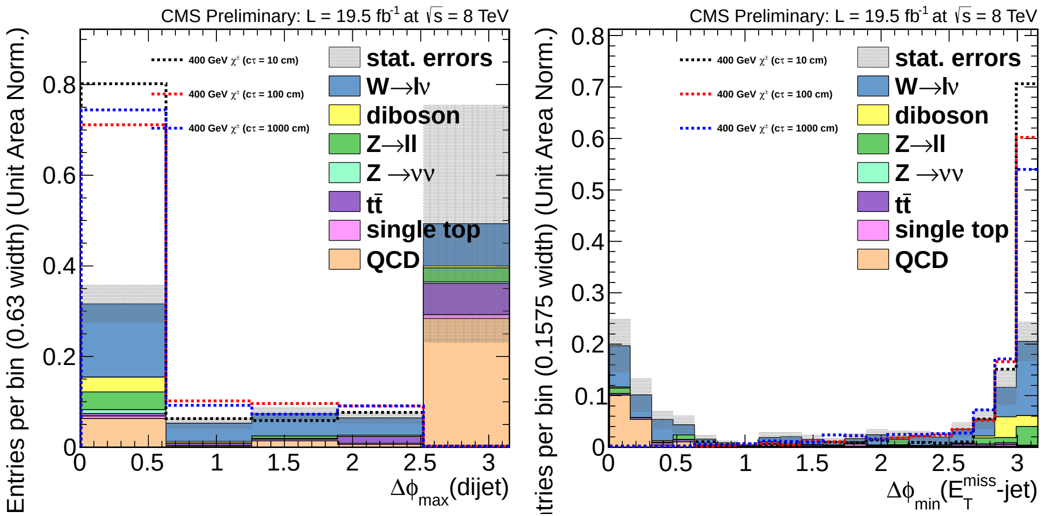

Figure 6.2: Distributions of two variables used to suppress the QCD background. The left is the maximum $\Delta\phi$ between any two jets for events passing the *Candidate Track* criteria, without the cuts on these two variables (N-2 plot). The right is the minimum $\Delta\phi$ between the $\not\!\!E_T$ and either of the two leading jets for events that additionally pass the $\Delta\phi(\text{dijet}) < 2.5$ requirement (N-1 plot). The *Candidate Track* selection requires $\Delta\phi(\not\!\!E_T\text{-jet}) > 0.5$.

- Tracks are required to have p_T >50 GeV and $|\eta| < 2.1$. Signal tracks typically have large transverse momentum, as shown in Figure 6.3.
- Tracks are required to have $|d_0| < 0.02$ cm and $|d_z|$ <0.5 cm.
- The track must have at least 7 valid hits to reduce the backgrounds associated with poorly-reconstructed tracks, as shown in N-1 plot in Figure 6.3.
- The track must not miss any hits in the layers before the last hit on the track, i.e., $N_{\text{miss}}^{\text{mid}} = 0$ and $N_{\text{miss}}^{\text{inner}} = 0$. The number of missing middle hits, $N_{\text{miss}}^{\text{mid}}$, is the number of hits expected but not found between the first and last hit associated to a track. The number of missing inner hits, $N_{\text{miss}}^{\text{inner}}$, corresponds to the lost hits prior to the first hit on the track, i.e. hits lost between the interaction point and the first hit associated to the track. Both quantities are calculated based on the

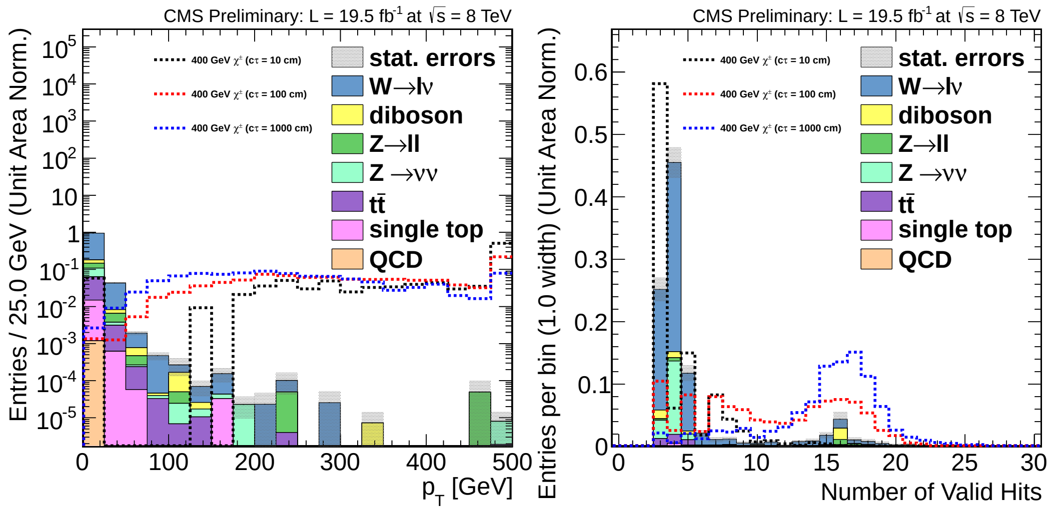

Figure 6.3: Distribution of the track p_T (left) and number of valid hits on the track (right), after all other (N-1) *Candidate Track* criteria. The *Candidate Track* selection requires $p_T > 50$ GeV and at least 7 hits.

tracker modules traversed by the track trajectory. The signal predominantly has no such missing hits, as shown in the N-1 plot in Figure 6.4.

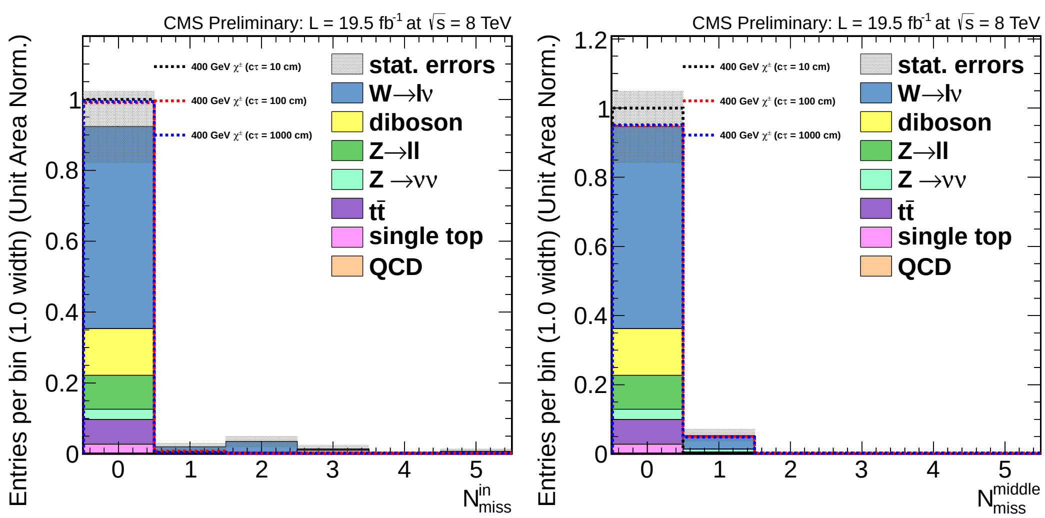

Figure 6.4: The number of missing inner (left) and middle (right) hits in tracks passing all other (N-1) *Candidate Track* criteria. The *Candidate Track* selection requires no missing inner or middle hits.

- Relative track isolation of $(\Sigma p_T^{\Delta R<0.3} - p_T)/p_T < 0.05$, where $\Sigma p_T^{\Delta R<0.3}$ is the sum of the p_T of all other tracks within a cone of $\Delta R < 0.3$ around the track. Additionally, we require that there is no subleading jet within a cone of $\Delta R < 0.5$ of the track. The background suppression of these requirements is illustrated in the N-1 plot in Figure 6.5.

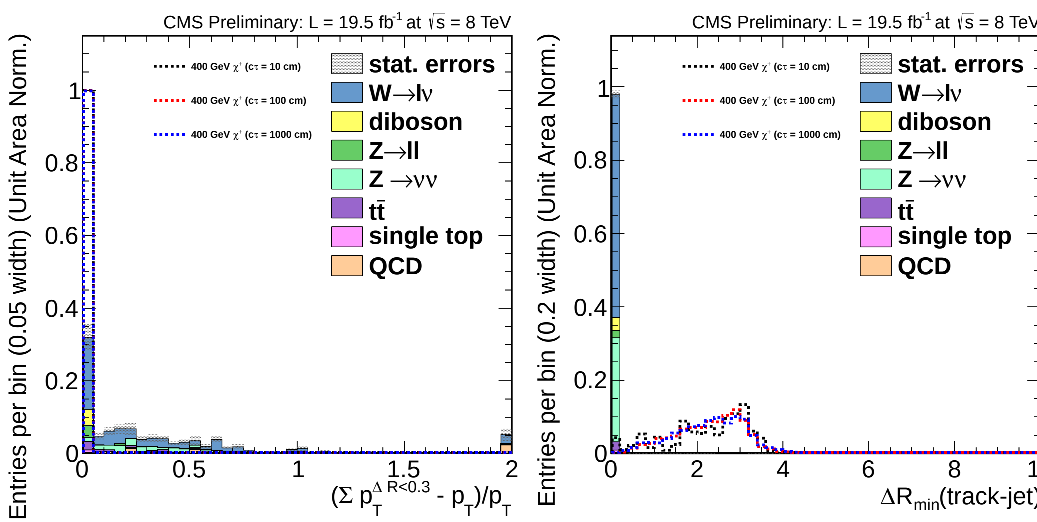

Figure 6.5: Distributions of the relative track isolation (left) and the minimum ΔR between the track and a jet (right), after all other (N-1) *Candidate Track* criteria. The *Candidate Track* selection requires relative track isolation < 0.05 and $\Delta R_{\rm min}$(track-jet)> 0.5.

- Veto any tracks within $\Delta R < 0.15$ of a reconstructed electron with $p_T > 10$ GeV. These electrons must also have at least the average score of 0 as the result of the multivariate analysis used to identify electrons.

- Veto tracks in the region between the barrel and endcap of the ECAL, 1.42$<$ $|\eta|$ $<$1.65, because some of the electron energy may be unreconstructed.

- Veto tracks within a cone of ΔR<0.05 of a dead or noisy ECAL channel; the determination of these channels is described in Section 7.2.

- Veto tracks pointed toward the intermodule gaps of the ECAL; the widths of these gaps are supplied by the ECAL Detector Performance Group (DPG). and listed in Table 6.1.

Table 6.1: Widths of ECAL intermodule gaps.

-1.14018 $< \eta <$ -1.1439
-0.791884 $< \eta <$ -0.796051
-0.44356 $< \eta <$ -0.447911
0.00238527 $< \eta <$ -0.00330793
0.446183 $< \eta <$ 0.441949
0.793955 $< \eta <$ 0.789963
1.14164 $< \eta <$ 1.13812

- Veto any tracks within $\Delta R < 0.15$ of a tracker, standalone, or global muon with $p_T > 10$ GeV.

- Veto any tracks directed towards the gap between stations 0 and 1 of the DT system, 0.15< $|\eta|$ <0.35 are rejected.

- Veto tracks in the region of 1.55< $|\eta|$ <1.85, which has a low muon reconstruction efficiency.

- Veto tracks within $\Delta R < 0.25$ of an errant CSC.

- Veto tracks within $\Delta R < 0.15$ of a hadronically decaying tau with $p_T > 30$ GeV and $|\eta| < 2.3$. These taus must also satisfy a set of loose isolation criteria; namely, the sum of all charged hadrons and photons within $\Delta R < 0.5$ of the tau candidate must be less than 2 GeV.

The electron, muon, and tau vetoes reject a large fraction of the background while retaining nearly all of the signal, as shown in the N-1 plot in Figure 6.6.

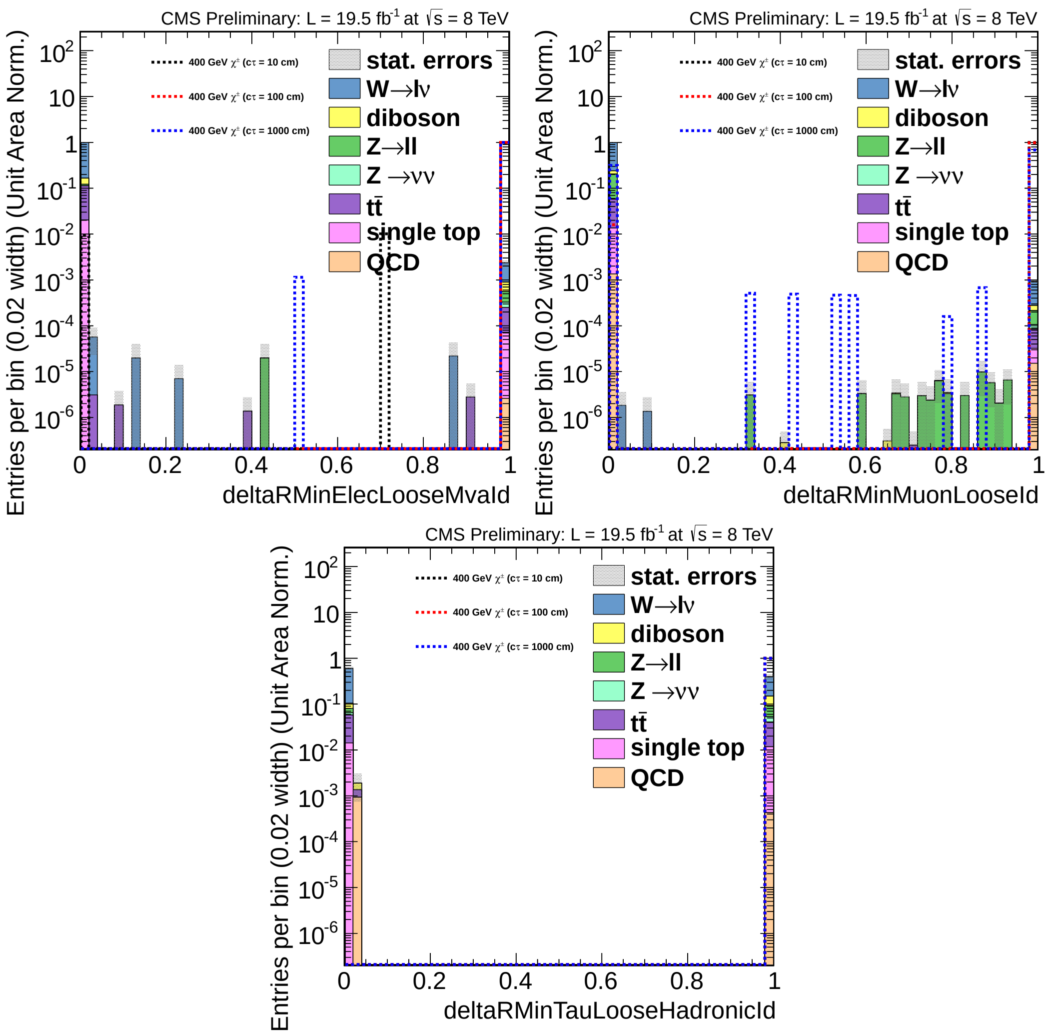

Figure 6.6: N-1 distributions of ΔR between the track and an electron (upper left), muon (upper right), or tau (lower), for events passing the *Candidate Track* criteria without the corresponding veto. Note that events in the overflow are added to the last bin and the histograms for the three samples are overlapping. The *Candidate Track* selection requires ΔR (track-lepton) > 0.15.

6.3 Disappearing Track Sample

We defined the *Disappearing Track* sample as events which pass the *Candidate Track* criteria described above as well as the *Disappearing Track* criteria listed below:

- The associated calorimeter energy $E_{\text{calo}}^{\Delta R<0.5}$ of the track must be less than 10 GeV. We compute $E_{\text{calo}}^{\Delta R<0.5}$ as the sum of the electromagnetic and hadronic calorimeter clusters within a $\Delta R < 0.5$ cone around the direction of the candidate track.[1] The effectiveness of this criteria is shown in the N-1 plot in Figure 6.7.

- The track must have ≥ 3 missing outer hits $N_{\text{miss}}^{\text{outer}}$, i.e., those after the last hit associated to the track. Similar to the calculation of missing inner and middle hits, the missing outer hits are determined from the tracker modules traversed by the track's projected trajectory. Tracks from signal have several missing outer hits as shown in the N-1 plot in Figure 6.7.

The *Candidate Track* and *Disappearing Track* subsamples are summarized in Table 6.2.

6.4 Background Estimate Samples

We use several samples to estimate, validate, and study the backgrounds to this search. These are detailed in the following subsections.

[1]To account for the effect of pile-up interactions, we follow the Muon POG prescription to apply a rho-correction of the calorimeter energy [66]: $E_{\text{calo}}^{\Delta R<0.5} = \max((E_{\text{calo}}^{\Delta R<0.5})^{\text{raw}} - A\rho_{kt6}^{calo}, 0)$, where $(E_{\text{calo}}^{\Delta R<0.5})^{\text{raw}}$ is the sum of calorimeter clusters, $A = \pi * (0.5)^2$ is the effective area of the cone in the $\eta - \phi$ plane, and ρ_{kt6}^{calo} is the density of calorimeter energy due to neutral pile-up particles. When the correction is larger than the raw energy, $E_{\text{calo}}^{\Delta R<0.5}$ is set to 0.

Table 6.2: *Candidate Track* and *Disappearing Track* subsamples

Subsample	Description	Requirements
	trigger	`HLTMonoCentralPFJet80_PFMETnoMu95_NHEF0p95`, `HLTMonoCentralPFJet80_PFMETnoMu105_NHEF0p95`, or `HLT_MET120_HBHENoiseCleaned`
Candidate Track	Missing Energy	$\not\!\!E_T > 100$ GeV
	Leading jet criteria	$p_T > 110$ GeV
		$\lvert\eta\rvert < 2.4$
		charged hadron energy fraction > 0.2
		neutral hadron energy fraction < 0.7
		charged EM energy fraction < 0.5
		neutral EM energy fraction < 0.7
	Additional jet criteria	no jet pairs with $\Delta\phi > 2.5$
		$\Delta\phi > 0.5$ - $\not\!\!E_T$ && 2 highest-p_T jets
	Track quality	$p_T > 50$ GeV
		$\lvert\eta\rvert < 2.1$
		$d_0 < 0.02$ cm
		$d_z < 0.5$ cm
		≥ 7 valid hits
		0 missing middle hits
		0 missing inner hits
	Track isolation	$(\Sigma p_T^{\Delta R<0.3} - p_T)/p_T < 0.05$
		$\Delta R > 0.5$ between track and any jet
	Lepton vetoes	!in ECAL barrel-endcap crack, $1.42 < \lvert\eta\rvert < 1.65$
		!in DT Wheel 0 gap, $0.15 < \lvert\eta\rvert < 0.35$
		!in region of larger μ reco. inefficiency $1.55 < \lvert\eta\rvert < 1.85$
		!within $\Delta R < 0.05$ of dead or noisy ECAL cluster
		!within intermodule gap of ECAL
		!within $\Delta R < 0.25$ of errant CSC
		!within $\Delta R < 0.15$ of e, $p_T > 10$ GeV && multivar. score > 0
		!within $\Delta R < 0.15$ of μ, $p_T > 10$ GeV
		!within $\Delta R < 0.15$ of τ, $p_T > 30$ GeV, $\lvert\eta\rvert < 2.3$, loose tau ID
Disappearing Track	Isolate signal	*Candidate Track* criteria (above)
		$E_{\text{calo}}^{\Delta R<0.5} < 10$ GeV
		≥ 3 missing outer hits

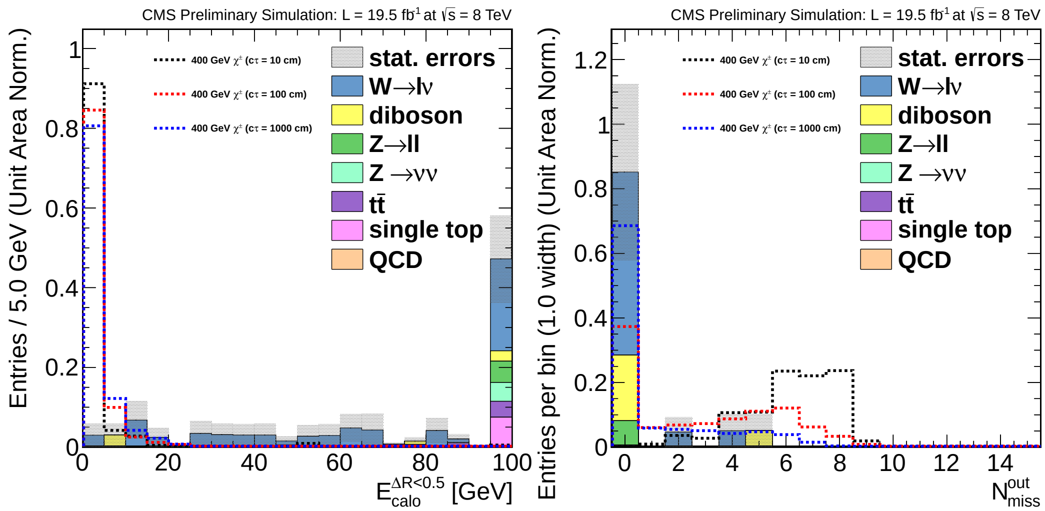

Figure 6.7: N-1 plot of calorimeter energy associated to selected tracks in the *Disappearing Track* sample (left). Overflow entries are included in the last bin. N-1 plot of the number of missing outer hits for selected tracks in the *Disappearing Track* sample. The *Disappearing Track* selection requires $E_{\text{calo}}^{\Delta R<0.5} < 10$ GeV and ≥ 3 missing outer hits.

6.4.1 Lepton control samples

Electron, *Muon*, and *Tau Control Samples* are used to estimate the lepton backgrounds in the search sample. These samples are obtained by applying all of the criteria of the *Disappearing Track* subsample, with the following modifications to the requirements placed on the track:

- In each lepton control sample, the corresponding lepton veto is removed.
- In the *Electron Control Sample* and *Tau Control Sample*, the $E_{\text{calo}}^{\Delta R<0.5} < 10$ GeV requirement is also removed because it is strongly correlated with the lepton identification.

The lepton control sample definitions are summarized in Table 6.3.

Table 6.3: Lepton control sample selection criteria. All criteria of the *Disappearing Track* subsample are required except for those listed here.

	Disappearing Track *subsample criteria removed*
Electron Control Sample	!in $\Delta R < 0.15$ of e (electron veto) $E_{\text{calo}}^{\Delta R<0.5} < 10$
Muon Control Sample	!in $\Delta R < 0.15$ of μ (muon veto)
Tau Control Sample	!in $\Delta R < 0.15$ of τ (tau veto) $E_{\text{calo}}^{\Delta R<0.5} < 10$ GeV

6.4.2 Lepton tag and probe samples

We use *Electron, Muon,* and *Tau Tag and Probe Samples* to assess the systematic uncertainty in the lepton background estimates. This tag and probe method is implemented to determine the lepton reconstruction efficiency. In each of the control samples, we require one tightly identified, isolated lepton, which serves as the tag lepton. The probe track is required to pass a set of track criteria which heavily mirrors the *Disappearing Track* selection; however, some modifications to this selection have been made to increase statistics. Lastly, the tag lepton and probe track must be opposite in sign and have invariant mass consistent with a Z$\rightarrow$ $\ell\ell$ decay. The criteria used to define the *Electron, Muon,* and *Tau Tag and Probe Samples* are listed in Tables 6.4, 6.5, 6.6, respectively.

The *Electron-ECAL Channel Tag and Probe Sample* is used to study dead/noisy ECAL channels. It has the same selection criteria as the *Electron Tag and Probe Sample* but with the veto of dead/noisy ECAL channels removed. Also, to increase statistics, the $N_{\text{miss}}^{\text{outer}}$ requirement is removed. These criteria are listed in Table 6.7.

To study the regions of low muon reconstruction efficiency, we use a *Muon Fiducial-Study Tag and Probe Sample* sample, which has the same criteria as the *Muon Tag and Probe Sample* sample but with the fiducial requirements removed and the muon

Table 6.4: *Electron Tag and Probe Sample* selection criteria.

trigger	`HLT_Ele27_WP80`
Tag electron	$p_T > 30$ GeV $\|\eta\| < 2.5$ pass tight ID $\|d_0\| < 0.02$, $\|d_z\| < 0.1$ relative isolation < 0.15 0 lost hits pass conversion veto
Probe track that passes the track criteria of *Disappearing Track* selection with some modifications, indicated by **bold face**	$\mathbf{p_T > 30}$ **GeV** $\|\eta\| < 2.1$ $d_0 < 0.02$ cm $d_z < 0.5$ cm ≥ 7 valid hits 0 missing middle hits 0 missing inner hits $(\Sigma p_T^{\Delta R<0.3} - p_T)/p_T < 0.05$ $\Delta R > 0.5$ between track and any subleading jet !in ECAL barrel-endcap crack, $1.42 < \|\eta\| < 1.65$!in DT Wheel 0 gap, $0.15 < \|\eta\| < 0.35$!in $1.55 < \|\eta\| < 1.85$!in $\Delta R < 0.05$ of dead or noisy ECAL cluster !in $\Delta R < 0.25$ of errant CSC !in $\Delta R < 0.15$ of μ !in $\Delta R < 0.15$ of τ ≥ 3 missing outer hits
Tag electron and probe track	opposite in sign $80 < m(\text{tag}, \text{probe}) < 100$ GeV

veto added. These criteria are listed in Table 6.8.

6.4.3 $Z \to \mu\mu$ *Control Sample*, $Z \to ee$ *Control Sample*, *Muon Fake Track Control Sample*, *Electron Fake Track Control Sample*, and *Kinematic Selection Sample*

The $Z \to \mu\mu$ *Control Sample*, $Z \to ee$ *Control Sample*, *Muon Fake Track Control Sample*, *Electron Fake Track Control Sample*, and *Kinematic Selection Sample* are used to estimate the background from fake tracks.

In the $Z \to \mu\mu$ *Control Sample* and $Z \to ee$ *Control Sample*, we require two

Table 6.5: *Muon Tag and Probe Sample* selection criteria.

trigger	HLT_IsoMu24_eta2p1
Tag muon	$p_T > 25$ GeV $\|\eta\| < 2.1$ passes tight ID relative isolation < 0.12
Probe track that passes the track criteria of *Disappearing Track* selection with some modifications, indicated by **bold face.**	$\mathbf{p_T > 30}$ **GeV** $\|\eta\| < 2.1$ $d_0 < 0.02$ cm $d_z < 0.5$ cm ≥ 7 valid hits 0 missing middle hits 0 missing inner hits $(\Sigma p_T^{\Delta R<0.3} - p_T)/p_T < 0.05$ $\Delta R > 0.5$ between track and any subleading jet !in ECAL barrel-endcap crack, $1.42 < \|\eta\| < 1.65$!in DT Wheel 0 gap, $0.15 < \|\eta\| < 0.35$!in $1.55 < \|\eta\| < 1.85$!in $\Delta R < 0.05$ of dead or noisy ECAL cluster !in $\Delta R < 0.25$ of errant CSC !in $\Delta R < 0.15$ of e !in $\Delta R < 0.15$ of τ $E_{\text{calo}}^{\Delta R<0.5} < 10$ ≥ 3 missing outer hits
Tag muon and probe track	opposite in sign $80 < m(\text{tag}, \text{probe}) < 100$ GeV

tightly identified, isolated leptons that are opposite in sign and have an invariant mass between 80 - 100 GeV, consistent with a Z boson decay. These criteria are listed in Tables 6.9 and 6.10.

The *Muon Fake Track Control Sample* sample is composed of events in the $Z \to \mu\mu$ *Control Sample* that contain an additional track that passes the track criteria of the *Disappearing Track* subsample selection. Similarly, the *Electron Fake Track Control Sample* sample is composed of events in the $Z \to ee$ *Control Sample* that contain an

Table 6.6: *Tau Tag and Probe Sample* selection criteria.

trigger	`HLT_IsoMu24_eta2p1`
tag muon consistent with $\tau \to \mu\nu\nu$ decay	$p_T > 25$ GeV $\|\eta\| < 2.1$ passes tight ID relative isolation < 0.12 $m_T(\mu, \not\!\!E_T) < 40$ GeV
Probe track that passes the track criteria of *Candidate Track* selection with some modifications, indicated by **bold face.**	$\mathbf{p_T > 30}$ **GeV** $\|\eta\| < 2.1$ $d_0 < 0.02$ cm $d_z < 0.5$ cm ≥ 7 valid hits 0 missing middle hits 0 missing inner hits $(\Sigma p_T^{\Delta R<0.3} - p_T)/p_T < 0.05$ $\Delta R > 0.5$ between track and any subleading jet !in ECAL barrel-endcap crack, $1.42 < \|\eta\| < 1.65$!in DT Wheel 0 gap, $0.15 < \|\eta\| < 0.35$!in $1.55 < \|\eta\| < 1.85$!in $\Delta R < 0.05$ of dead or noisy ECAL cluster !in $\Delta R < 0.25$ of errant CSC !in $\Delta R < 0.15$ of e !in $\Delta R < 0.15$ of μ
Tag muon and probe track	opposite in sign $40 < m(\text{tag}, \text{probe}) < 75$ GeV

additional track that passes the track criteria of the *Disappearing Track* subsample selection. These criteria are listed in Tables 6.11 and 6.12.

The *Kinematic Selection Sample* is defined as the events that pass only the $\not\!\!E_T$ and jet selection requirements of the *Disappearing Track* subsample. There are no track criteria applied to events in this sample. The criteria of the *Kinematic Selection Sample* is listed in Table 6.13.

Table 6.7: *Electron-ECAL Channel Tag and Probe Sample* selection criteria.

trigger	`HLT_Ele27_WP80`
Tag electron	$p_T > 20$ GeV $\|\eta\| < 2.5$ pass tight ID $\|d_0\| < 0.02$, $\|d_z\| < 0.1$ relative isolation < 0.15 0 lost hits pass conversion veto
Probe track that passes the track criteria of *Disappearing Track* selection with some modifications, indicated by **bold face**	$\mathbf{p_T > 30}$ **GeV** $\|\eta\| < 2.1$ $d_0 < 0.02$ cm $d_z < 0.5$ cm ≥ 7 valid hits 0 missing middle hits 0 missing inner hits $(\Sigma p_T^{\Delta R<0.3} - p_T)/p_T < 0.05$ $\Delta R > 0.5$ between track and any subleading jet !in ECAL barrel-endcap crack, $1.42 < \|\eta\| < 1.65$!in intermodule gaps of ECAL !in DT Wheel 0 gap, $0.15 < \|\eta\| < 0.35$!in $1.55 < \|\eta\| < 1.85$!in $\Delta R < 0.25$ of errant CSC !in $\Delta R < 0.15$ of e !in $\Delta R < 0.15$ of μ !in $\Delta R < 0.15$ of τ $E_{\rm calo}^{\Delta R<0.5} < 10$ GeV
Tag electron and probe track	opposite in sign $80 < m(\rm tag, probe) < 100$ GeV

6.4.4 $E_{\rm calo}^{\Delta R<0.5}$ and $N_{\rm miss}^{\rm outer}$ *Sideband Samples*

The $E_{\rm calo}^{\Delta R<0.5}$ *Sideband Sample* and $N_{\rm miss}^{\rm outer}$ *Sideband Sample* are used to validate the background estimate. They are depleted in signal by inverting the requirements used to isolate signal events. These samples are defined as events that pass all of the criteria of the *Candidate Track* subsample, with the following modifications:

- In both samples, the track is required to have $p_T > 30$ GeV (instead of > 50 GeV).

Table 6.8: *Muon Fiducial-Study Tag and Probe Sample* selection criteria.

trigger	HLT_IsoMu24_eta2p1
Tag muon	$p_T > 25$ GeV $\|\eta\| < 2.1$ passes tight ID relative isolation < 0.12
Probe track that passes the track criteria of *Disappearing Track* selection with some modifications, indicated by **bold face**	$\mathbf{p_T > 30}$ **GeV** $\|\eta\| < 2.1$ $d_0 < 0.02$ cm $d_z < 0.5$ cm ≥ 7 valid hits 0 missing middle hits 0 missing inner hits $(\Sigma p_T^{\Delta R<0.3} - p_T)/p_T < 0.05$ $\Delta R > 0.5$ between track and any subleading jet !in $\Delta R < 0.15$ of e !in $\Delta R < 0.15$ of μ !in $\Delta R < 0.15$ of τ $E_{\text{calo}}^{\Delta R<0.5} < 10$ ≥ 3 missing outer hits
Tag muon and probe track	opposite in sign $80 < m(\text{tag}, \text{probe}) < 100$ GeV

Table 6.9: $Z \to \mu\mu$ *Control Sample* selection criteria.

trigger	HLT_IsoMu24_eta2p1
Two muons	$p_T > 25$ GeV $\|\eta\| < 2.5$ pass tight ID relative isolation < 0.12 $\|d_0\| < 0.02$ cm, $\|d_z\| < 0.02$ cm opposite in sign $80 < m(\mu\mu) < 100$ GeV

Table 6.10: $Z \to ee$ *Control Sample* selection criteria.

trigger	`HLT_IsoMu24_eta2p1`
Two electrons	$p_T > 25$ GeV $\lvert\eta\rvert < 2.5$ pass tight ID relative isolation < 0.15 $\lvert d_0\rvert < 0.02$ cm, $\lvert d_z\rvert < 0.1$ cm opposite in sign $80 < m(ee) < 100$ GeV

- In the $E_{\text{calo}}^{\Delta R<0.5}$ *Sideband Sample*, the associated calorimeter energy of the track must be greater than 10 GeV.
- In the $N_{\text{miss}}^{\text{outer}}$ *Sideband Sample*, the track is required to have ≤ 2 missing outer hits.

The definitions of the $E_{\text{calo}}^{\Delta R<0.5}$ and $N_{\text{miss}}^{\text{outer}}$ *Sideband Samples* are summarized in Tables 6.14 and 6.15.

6.4.5 Selection summary

The samples obtained with these selections and their use in the analysis are summarized in Table 6.16.

Table 6.11: *Muon Fake Track Control Sample* selection criteria.

trigger	HLT_IsoMu24_eta2p1
Two muons	$p_T > 25$ GeV $\|\eta\| < 2.5$ pass tight ID relative isolation < 0.12 $\|d_0\| < 0.02$ cm, $\|d_z\| < 0.02$ cm opposite in sign $80 < m(\mu\mu) < 100$ GeV
Track that passes track criteria of *Disappearing Track* subsample	$p_T > 50$ GeV $\|\eta\| < 2.1$ $d_0 < 0.02$ cm $d_z < 0.5$ cm ≥ 7 valid hits 0 missing middle hits 0 missing inner hits $(\Sigma p_T^{\Delta R<0.3} - p_T)/p_T < 0.05$ $\Delta R > 0.5$ between track and any subleading jet !in ECAL barrel-endcap crack, $1.42 < \|\eta\| < 1.65$!in DT Wheel 0 gap, $0.15 < \|\eta\| < 0.35$!in $1.55 < \|\eta\| < 1.85$!in $\Delta R < 0.05$ of dead or noisy ECAL cluster !in intermodule gap of ECAL !in $\Delta R < 0.25$ of errant CSC !in $\Delta R < 0.15$ of e !in $\Delta R < 0.15$ of μ !in $\Delta R < 0.15$ of τ $E_{\text{calo}}^{\Delta R<0.5} < 10$ ≥ 3 missing outer hits

Table 6.12: *Electron Fake Track Control Sample* selection criteria.

trigger	HLT_IsoMu24_eta2p1
Two electrons	$p_T > 25$ GeV $\|\eta\| < 2.5$ pass tight ID relative isolation < 0.15 $\|d_0\| < 0.02$ cm, $\|d_z\| < 0.1$ cm opposite in sign $80 < m(ee) < 100$ GeV
Track that passes track criteria of *Disappearing Track* subsample	$p_T > 50$ GeV $\|\eta\| < 2.1$ $d_0 < 0.02$ cm $d_z < 0.5$ cm ≥ 7 valid hits 0 missing middle hits 0 missing inner hits $(\Sigma p_T^{\Delta R<0.3} - p_T)/p_T < 0.05$ $\Delta R > 0.5$ between track and any subleading jet !in ECAL barrel-endcap crack, $1.42 < \|\eta\| < 1.65$!in DT Wheel 0 gap, $0.15 < \|\eta\| < 0.35$!in $1.55 < \|\eta\| < 1.85$!in $\Delta R < 0.05$ of dead or noisy ECAL cluster !in intermodule gap of ECAL !in $\Delta R < 0.25$ of errant CSC !in $\Delta R < 0.15$ of e !in $\Delta R < 0.15$ of μ !in $\Delta R < 0.15$ of τ $E_{\rm calo}^{\Delta R<0.5} < 10$ ≥ 3 missing outer hits

Table 6.13: *Kinematic Selection Sample* selection criteria.

Missing Energy	$\not\!\!E_T > 100$ GeV
Leading jet criteria	$p_T > 110$ GeV $\|\eta\| < 2.4$ charged hadron energy fraction > 0.2 neutral hadron energy fraction < 0.7 charged EM energy fraction < 0.5 neutral EM energy fraction < 0.7
Additional jet criteria	no jet pairs with $\Delta\phi > 2.5$ $\Delta\phi > 0.5$ - $\not\!\!E_T$ && 2 highest-p_T jets

Table 6.14: $E_{\text{calo}}^{\Delta R<0.5}$ *Sideband Sample* selection criteria.

All requirements of the *Candidate Track* subsample, but with two modified track criteria:
$p_T > 30$ GeV
$E_{\text{calo}}^{\Delta R<0.5} > 10$ GeV

Table 6.15: $N_{\text{miss}}^{\text{outer}}$ *Sideband Sample* selection criteria.

All requirements of the *Candidate Track* subsample, but with two modified track criteria:
$p_T > 30$ GeV
$N_{\text{miss}}^{\text{outer}} \leq 2$

Table 6.16: Selections employed in the analysis.

Sample	Purpose	Definition	Dataset
Candidate Track	study track quality cuts	Table 6.2	`MET`
Disappearing Track	search sample	Table 6.2	`MET`
Lepton Control	bkgd. estimate	Table 6.3	`MET`
Lepton Tag & Probe	bkgd. est. syst. uncertainty	Tables 6.4 to 6.6	`SingleMu/Elec.`
Electron-ECAL Channel Tag and Probe	study dead/noisy ECAL channels	Table 6.7	`SingleElec`
Muon Fiducial-Study Tag and Probe	study muon inefficiency regions	Table 6.8	`SingleMu`
$Z \to \mu\mu$, $Z \to ee$ *Control*	fake track bkgd. estimate	Tables 6.9 and 6.10	`SingleMu/Elec.`
Muon/Electron Fake Track Control	fake track bkgd. estimate	Tables 6.11 and 6.12	`SingleMu/Elec.`
Kinematic Selection Sample	fake track bkgd. estimate	Table 6.13	`SingleMu`
$E_{\text{calo}}^{\Delta R<0.5}$, $N_{\text{miss}}^{\text{outer}}$ *Sideband*	bkgd. estimate validation	Tables 6.14 and 6.15	`MET`

Chapter 7
Background Characterization

The physics sources of background in the search sample arise from SM processes that produce an electron, muon, or tau that is not reconstructed; consequently, the track is not associated to the lepton, and it survives the corresponding lepton veto. In addition, there is an instrumental source of background from "fake tracks", i.e. false trajectories that cannot be associated to a single, charged particle.

In the following sections we examine the sources of both physics and instrumental backgrounds to this search. We consider how a disappearing track signature may be produced, that is, a high-momentum ($p_T > 50$ GeV), isolated track without hits in the outer layers of the tracker and with little associated energy (< 10 GeV) deposited in the calorimeters. Various mechanisms that lead to tracks with missing outer hits are described, and the reconstruction limitations that impact each background category are investigated.

7.1 Algorithmic sources of missing outer hits

In this section, sources of missing outer hits that arise from choices made by the default CMS tracking algorithms are identified. These allow a particle that traverses all of the layers of the tracker to produce a track with missing outer hits, thereby mimicking our signal. We investigate these algorithmic effects with the muon (narrow-

η) single particle sample listed in Table 5.3. We require $|\eta| < 0.8$ to ensure that the muon trajectory traverses all the layers of the tracker barrel. In this sample of 3,000 events, 11.1% produce tracks with at least one missing outer hit. While these algorithmic sources of missing outer hits were studied with muons, they nevertheless impact the tracks produced by any particle, i.e. they contribute to the background from each of the physics sources as will be described in Sections 7.2, 7.3, and 7.4.

As discussed in Section 4.3.1, CMS uses an iterative tracking strategy that chooses the reconstructed track from a myriad of possible track trajectories based on which trajectory has the highest quality score. Recall, the quality score is defined as $Q = BN_{\text{found}} - PN_{\text{lost}} - \chi^2$, where N_{found} is the number of hits associated to the trajectory, in which a hit is expected but not found (missing hits after the last hit on the trajectory are not included), B is a valid hit bonus set to be equal to 5, P is a missing hit penalty set to be equal to 20, and χ^2 is taken from the fit of all the hits associated to the trajectory. Intuitively, it would seem that a trajectory without missing outer hits would always have a higher quality score than a trajectory with missing outer hits. However, we have found that there are several ways for a trajectory with missing outer hits to have a higher quality score than the trajectory without missing outer hits and thus, be chosen as the reconstructed track. The predominant mechanisms by which this occurs are that the trajectory with missing outer hits has a smaller χ^2 or a larger N_{lost}, resulting in a larger quality score Q. Therefore, the trajectory with missing outer hits is chosen as the reconstructed track.

The algorithmic sources that contribute to the 11.1% of muon tracks with at least one missing outer hit are summarized below:

- 7.3%: The muon passes through the wire bonds of the strip tracker module. The wire bonds between the two silicon sensors is inactive material, so a charged particle passing through it will not produce a recorded hit. Such a lost hit would count toward N_{lost}. Figure 7.1 shows the normalized local y-position of the intersection of the track trajectory with a module, for the cases where no simulated hit is produced. These are predominantly within $|y| < 0.02$; the wire bonds are at $y = 0$.

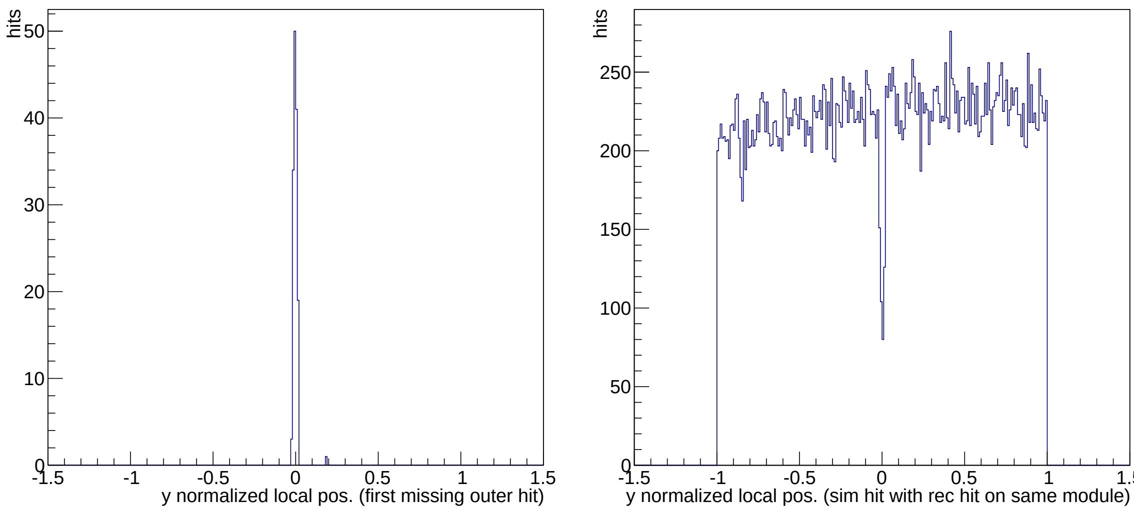

Figure 7.1: The normalized local y-position of the intersection of a track trajectory with a module, when no simulated hit is produced (left), and the position of simulated hits for which a hit is reconstructed (right), in the muon (narrow-η) single particle sample.

- 2.7%: An alternate trajectory with fewer missing outer hits is found, but its χ^2 is larger than that of the selected trajectory, leading to a lower quality score. The minimum difference in quality score between the track and an alternate trajectory is shown in Figure 7.2.
- 0.7%: The last hit on the track is mistakenly removed during the track fitting step of the iterative tracking. This is due to an error in the track-hit association software [67]. The software is designed to smooth the track by removing spurious

hits, but in some cases it removes the last hit instead of an outlier.

- 0.4%: No trajectory without missing outer hits is found. These tracks contribute to the last bin of the histogram in Figure 7.2.

The algorithms that select the best candidate track trajectory could be modified to eliminate most of the missing outer hits from these sources. Such modifications would require reprocessing all of the data, so we did not implement them for this analysis.

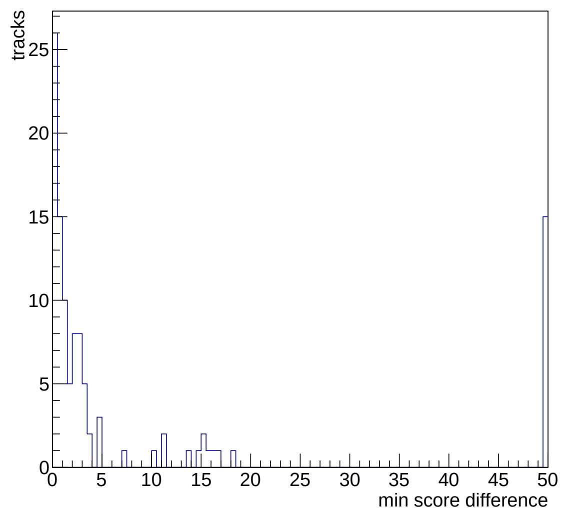

Figure 7.2: The minimum difference in the quality score Q between the reconstructed track and an alternate trajectory that uses the same pixel seed, for tracks in the muon (narrow-η) single particle sample with a missing outer hit not due to a glue joint or track smoothing bug. Tracks for which no alternate trajectories are found contribute to the last bin of this histogram.

7.2 Electrons

We reject any tracks matched to an identified electron, but an electron may fail to be identified if its energy is not fully recorded by the ECAL. This can happen if the electron is directed towards an ECAL channel that is dead/noisy. When this occurs, these unreconstructed electrons can pass the $E_{\text{calo}}^{\Delta R<0.5} < 10$ criterion. To avoid a background from these electrons, we reject tracks within a cone of ΔR<0.05 of a dead/noisy ECAL channel. To study these channels, we use events in the *Electron-ECAL Channel Tag and Probe Sample* defined in Table 6.7. The list of 1222 ECAL channels which were classified as dead or noisy at any point during the 2012 run is supplied by the ECAL DPG. These known dead/noisy ECAL channels as well as the comparison of this map with data events in the *Electron-ECAL Channel Tag and Probe Sample* are shown in Figure 7.3. Most clusters in η,ϕ for the data coincide with known dead or noisy ECAL channels.

D

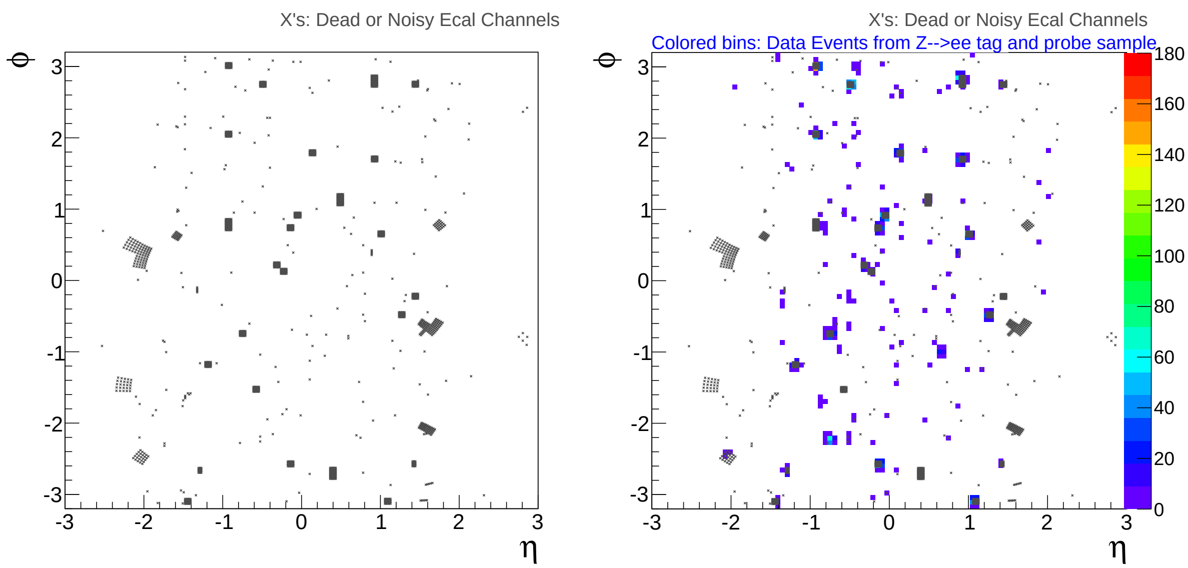

Figure 7.3: Distribution of ϕ versus ECAL detector η for the dead/noisy ECAL channels, denoted by x's (left). The map of dead/noisy ECAL channels overlaid with the ϕ versus ECAL detector η distribution of the probe track (right). The probe track is selected from the *Electron-ECAL Channel Tag and Probe Sample* defined in Table 6.7. Most clusters in η, ϕ for the data coincide with a known dead or noisy ECAL channel.

Figure 7.4 shows the η,ϕ distribution for the probe track in the same sample after vetoing tracks within $\Delta R < 0.05$ of any dead/noisy ECAL channel. Even after this requirement, some clusters are still present in the data that do not coincide with known dead or noisy ECAL channels. In the η,ϕ distribution of probe tracks, we classify any bin with at least 3 data events as a 'hot spot' and add it to the map of dead or noisy ECAL channels. There are 12 such coordinates added; these are listed in Table 7.1. After all other selection criteria, the signal is 88%-94% efficient for the veto of tracks directed toward dead/noisy ECAL channels.

In addition, electrons may also fail to be reconstructed and pass the $E_{\mathrm{calo}}^{\Delta R<0.5} < 10$ requirement if they are directed toward the overlap region between the barrel and endcap of the ECAL. We require that the track not have pseudorapidity of $1.42 < |\eta| < 1.65$, the region of the barrel-endcap overlap. For the same reason, we veto tracks that fall within the pseudorapidity ranges corresponding to intermodule gaps of the ECAL. These pseudorapidity ranges are listed in Table 6.1.

Table 7.1: ECAL detector η, ϕ coordinates added to the map of dead or noisy ECAL channels.

η	ϕ
1.35	-0.288
0.81	-1.696
0.81	0.736
-0.75	-2.272
-0.75	-2.208
0.69	-2.272
-0.69	-2.208
0.51	-0.224
0.63	-1.056
0.63	-0.992
0.69	-1.056
0.69	-0.992

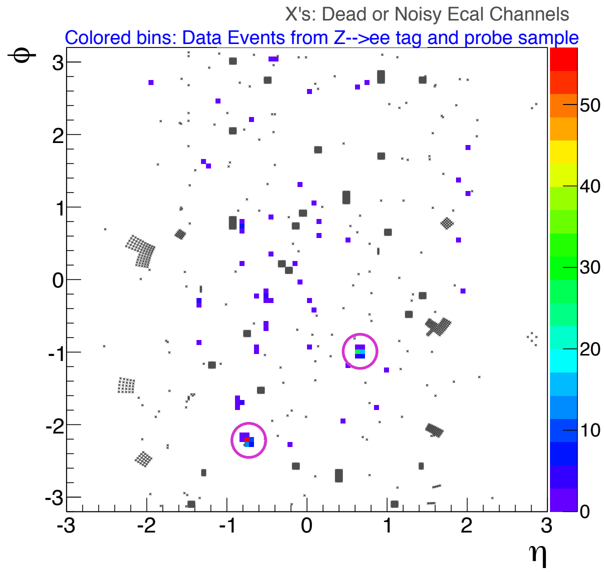

Figure 7.4: The map of dead or noisy ECAL channels (denoted by x's) overlaid with the distribution of ϕ versus ECAL detector η in the *Electron-ECAL Channel Tag and Probe Sample* defined in Table 6.7. Additionally, we have vetoed events in which the probe track is within $\Delta R < 0.05$ of a dead/noisy ECAL channel present in the list supplied by the ECAL DPG. Some clusters are still present in the data where a known dead or noisy ECAL channel is not found, two of which have been circled in magenta.

Lastly, a track from an electron can pass the $N_{\text{miss}}^{\text{outer}} \geq 3$ criterion by having missing outer hits due to the algorithmic sources described in Section 7.1 or due to bremsstrahlung in the tracker. A high-energy bremsstrahlung photon can change the electron momentum such that subsequent hits are not associated with the original track. A typical event display is shown in Figure 7.5.

7.3 Muons

To reduce the background from muons, we veto tracks that are matched to a muon meeting loose identification criteria. However, some muons evade this veto. For this to happen, a muon must fail to be reconstructed as a global, standalone, or tracker

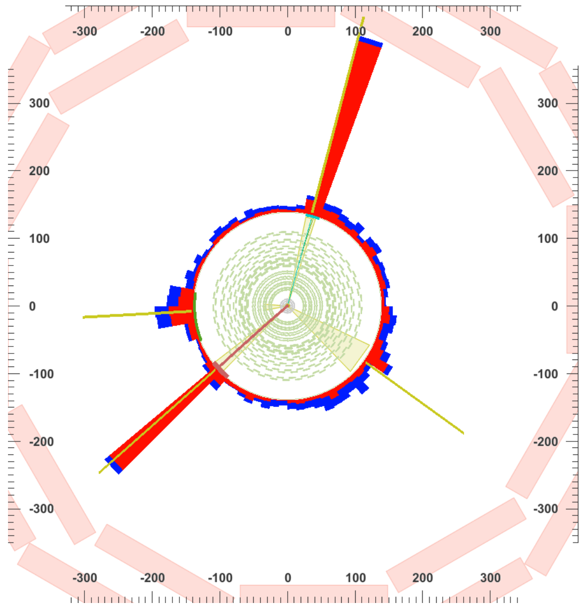

Figure 7.5: An event display for a $Z \to ee$ event in the *Electron Tag and Probe Sample*. The highlighted electron has a p_T of 40 GeV and lost 95% of its energy due to bremsstrahlung. The electron track is missing five outer hits. A reconstructed photon with a p_T of 15 GeV is also present in the event.

muon. Global and standalone muons require a reconstructed track in the muon system alone. A tracker muon requires a reconstructed tracker track (with $p_T > 0.5$ GeV and $p > 2.5$ GeV) that is matched to at least one segment in the DT or CSC muon detectors. The track and muon segment are considered matched if they pass at least one of two criteria:

- $\Delta X < 3.0$ cm, where ΔX is the absolute difference in the local x position propagated from the track, and the local x position of the muon segment, or
- $\sigma_X < 4.0$, where $\sigma_X = \Delta X / \sqrt{(\sigma_X^{\text{segment}})^2 + (\sigma_X^{\text{track}})^2}$ is the significance of the difference in local x position.

We investigate how a muon may fail to be reconstructed as a tracker muon with the muon (wide-η) single particle sample listed in Table 5.3. There are 68 events out of one million in which no muon is reconstructed, corresponding to an inefficiency of 6.8×10^{-5}. We examine these 68 events in an event display, and classify their signatures into several categories:

- 6 events: An ECAL deposit of at least 10 GeV is produced. This is consistent with a $\mu \to e\nu\nu$ decay. An example event is shown in Figure 7.6.

- 29 events: An HCAL deposit of at least 10 GeV is produced. An example event is shown in Figure 7.7.

- 19 events: One or more DT or CSC muon segments are produced but fail the tracker muon quality criteria ($\Delta X < 3$ cm or $\sigma_X < 4$). An example event is shown in Figure 7.8.

- 14 events: There are no ECAL or HCAL deposits greater than 10 GeV and no DT or CSC segments are recorded. An example event is shown in Figure 7.9.

The contributions of these signatures are summarized in Table 7.2.

Signature	Relative contribution
ECAL deposit > 10 GeV	9%
HCAL deposit > 10 GeV	43%
DT or CSC muon segments, but fail ($\Delta X < 3$ cm or $\sigma_X < 4$)	28%
no DT or CSC segments	21%

To reduce the background from unreconstructed muons, we apply fiducial cuts to reject candidate tracks in geometrical regions where the muon inefficiency is larger than average. We study these regions in the *Muon Fiducial-Study Tag and Probe Sample.*

- Tracks with $0.15 < |\eta| < 0.35$ are eliminated to avoid the gap between Wheel 0 and Wheel 1 of the DT stations, as shown in Figure 7.10.

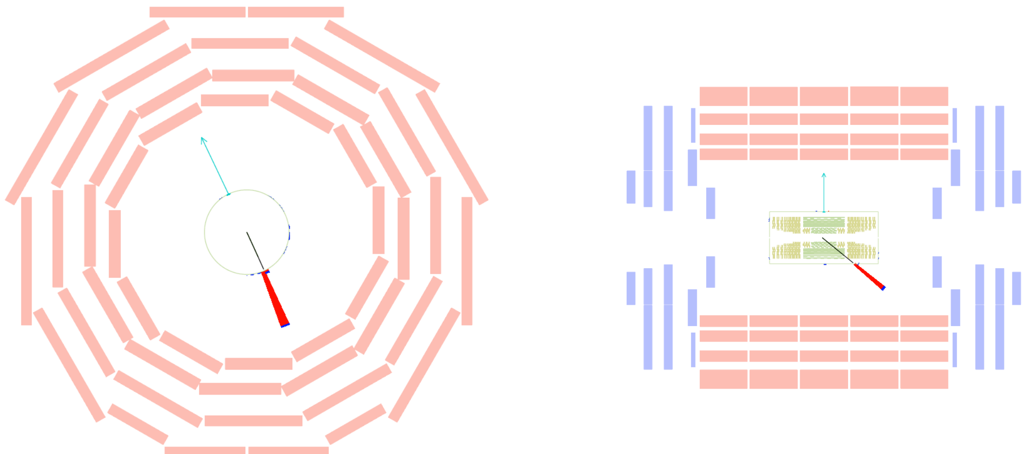

Figure 7.6: A simulated p_T =100 GeV muon single particle event, in which the muon decays and produces an ECAL deposit of 84 GeV.

- Tracks with 1.55< $|\eta|$ <1.85 are rejected. This region also has larger muon inefficiency, as shown in Figure 7.10.
- Tracks that are within $\Delta R < 0.25$ of a bad CSC are rejected. The list of bad CSC's over the course of the 2012 run is provided by the CSC DPG. The regions excluded by this veto are shown in Figure 7.11.

Because muons deposit minimum-ionizing energy clusters in the calorimeter, a substantial fraction pass the $E_{\text{calo}}^{\Delta R<0.5} < 10$ requirement. A muon may pass the $N_{\text{miss}}^{\text{outer}} \geq 3$ criterion as a consequence of the algorithmic sources of missing outer hits described in Section 7.1.

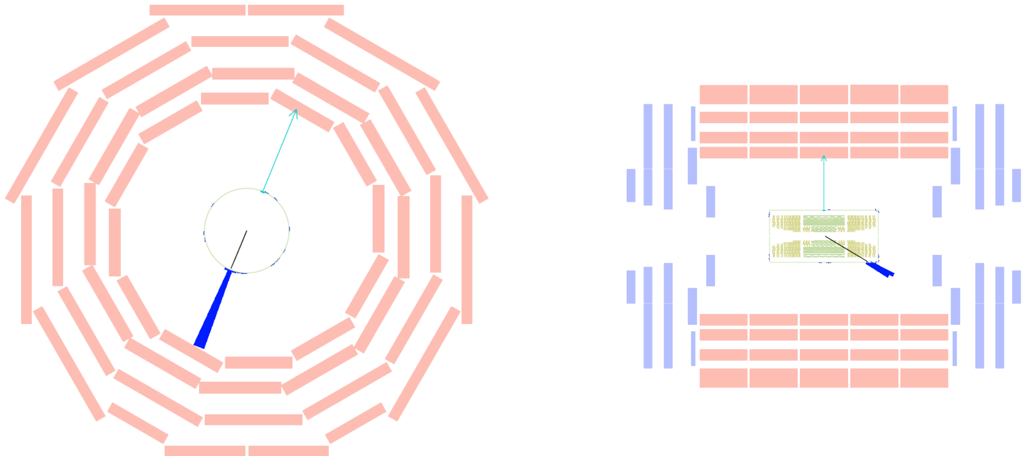

Figure 7.7: A simulated p_T =100 GeV muon single particle event, in which the muon produces a secondary electromagnetic shower. An HCAL deposit of 116 GeV is recorded.

7.4 Taus

The tau leptons that contribute to the *Candidate Track* sub-sample are predominantly single-prong decays, $\tau \to \pi\nu$, because the track isolation requirement effectively rejects taus that decay to three charged particles.

For these remaining taus to survive the tau veto, the tau must have a large reconstructed p_T and very little energy deposited in the calorimeters, $E_{\mathrm{calo}}^{\Delta R<0.5}$. Since most taus deposit an energy in the calorimeters that is on the order of their reconstructed p_T, this mismatch causes the tau to fail the tau reconstruction. This imbalance is the result of the discrepancy between the generated track p_T and the reconstructed track p_T.

In addition to failing the tau reconstruction, the pion from the $\tau \to \pi\nu$ decay

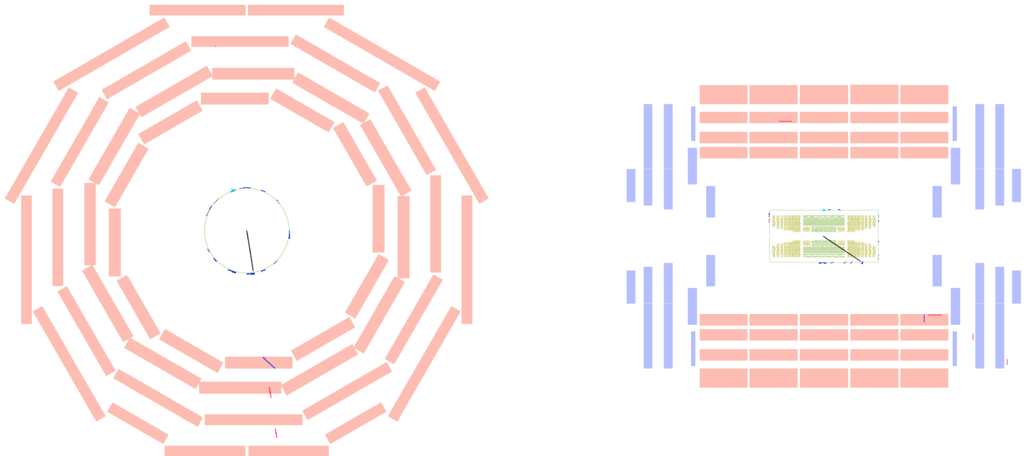

Figure 7.8: A simulated muon single particle event, in which a generated muon with p_T =100 GeV produces a DT segment (blue) that fails the matching criteria: $\Delta X = 9.3$ cm and $\sigma_X = 17.7$. RPC hits (magenta) are also recorded.

could also pass the $E_{\text{calo}}^{\Delta R<0.5} < 10$ GeV criterion. For this to happen, a pion must have a low true p_T (e.g. $p_T \sim 20$ GeV). Such a pion will fail the $p_T > 50$ GeV requirement, provided its p_T is accurately measured. However, if the p_T of the pion is significantly mismeasured, then it may pass this track p_T cut. In the latter case, the pion can mimic the signal since it has a large reconstructed p_T and little $E_{\text{calo}}^{\Delta R<0.5}$. One such event is displayed in Figure 7.13.

This class of background is studied using the pion single particle sample listed in Table 5.3. We first study how the p_T resolution changes with the number of hits on the track. After generating the pion single particle events, we remove all hits on the track after the 5th, 6th, or 7th valid hit and repeat the reconstruction of the sample. We then compare the tracks that are missing a substantial number of outer hits and tracks that have a large number of valid hits. We find that tracks with

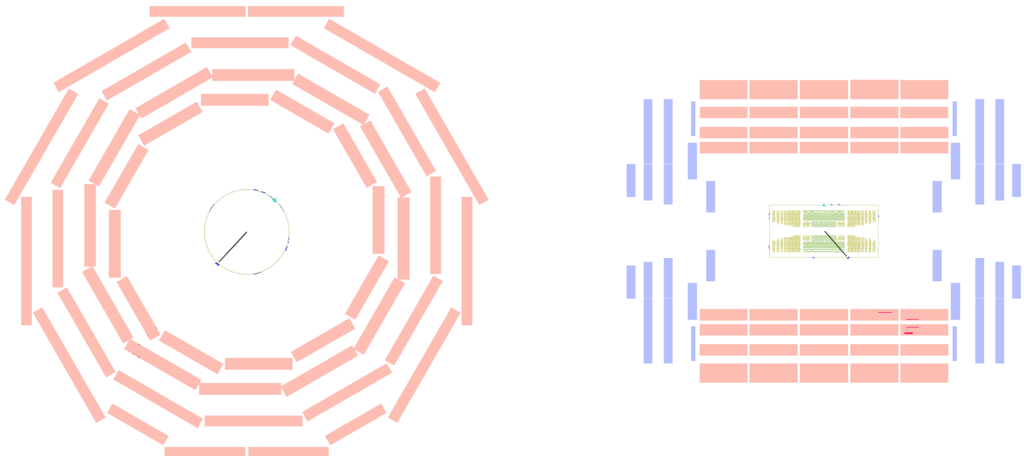

Figure 7.9: A simulated p_T =100 GeV muon single particle event, in which no DT or CSC segment is recorded. RPC hits (magenta) are produced.

a larger number of missing outer hits are much more likely to have a p_T which is significantly mismeasured than tracks with few missing outer hits. Figure 7.14 shows the distribution of reconstructed p_T for tracks with exactly 5 valid hits, exactly 6 hits, and exactly 7 hits.

Next, we study how the number of missing outer hits affects $E_{\text{calo}}^{\Delta R<0.5}$. Since the amount of energy that a track deposits in the calorimeters is only a function of the generated p_T of the pion, the $E_{\text{calo}}^{\Delta R<0.5}$ distribution is independent of the number of missing outer hits. Figure 7.14 shows the distribution of $E_{\text{calo}}^{\Delta R<0.5}$ for pion tracks with 5 hits, 6 hits, and 7 hits.

The p_T resolution increases the greater the lever arm used to measure the curvature such that tracks with 7 hits have a better p_T resolution. As shown in Figure 7.14, the number of tracks with poorer p_T resolution decreases as the number of valid hits

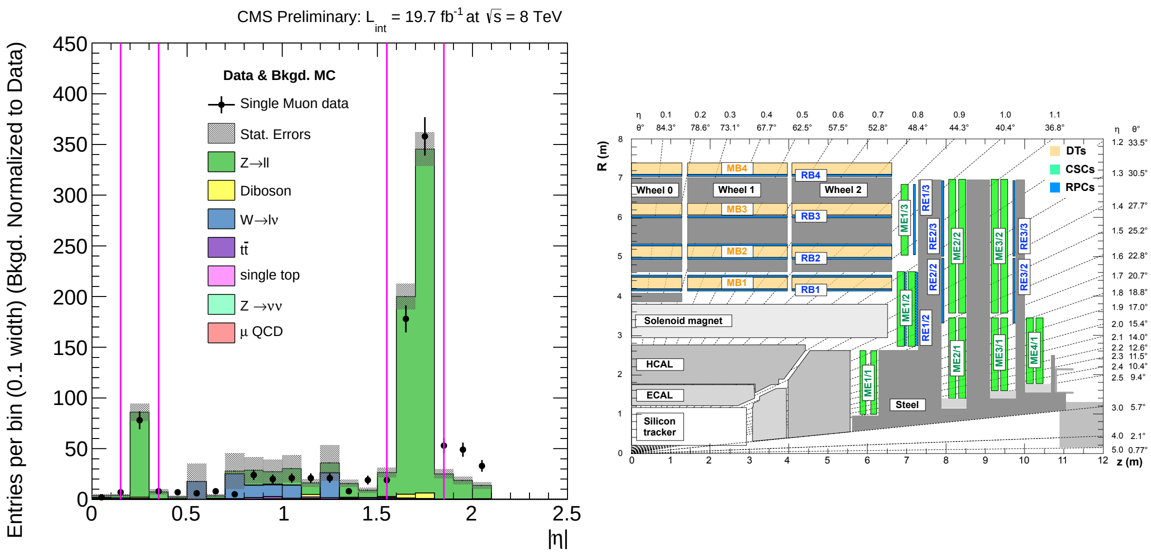

Figure 7.10: Top: Distribution of $|\eta|$ of probe tracks in *Muon Fiducial-Study Tag and Probe Sample*. The regions in $|\eta|$ that are excluded are defined by the magenta lines. Bottom: layout of one-quarter of the CMS muon system.

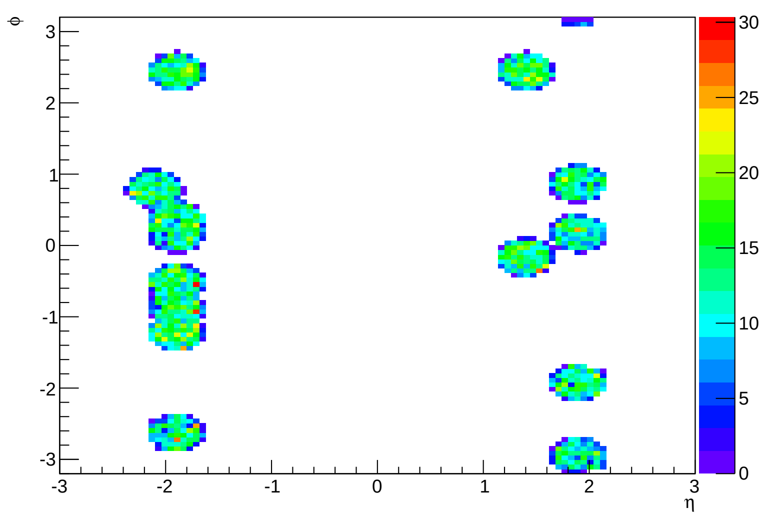

Figure 7.11: Regions within $\Delta R < 0.25$ of a bad CSC, in which candidate tracks are rejected.

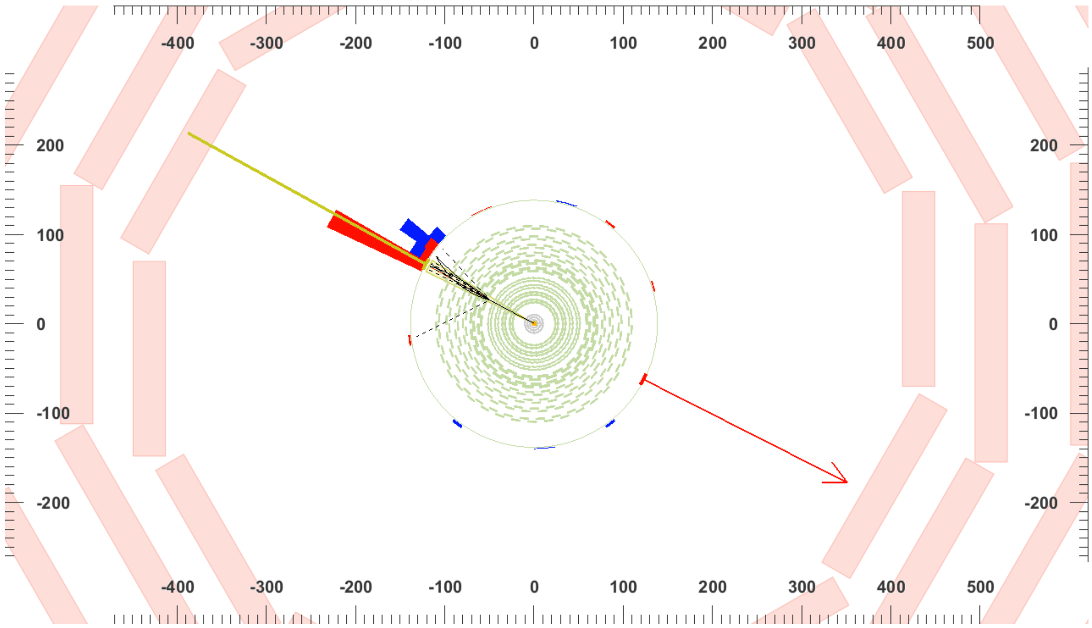

Figure 7.12: An event display of a pion single particle event in which the pion undergoes a nuclear interaction. The black tracks are simulated tracks indicating an interaction with the tracker material. This track is missing 4 outer hits.

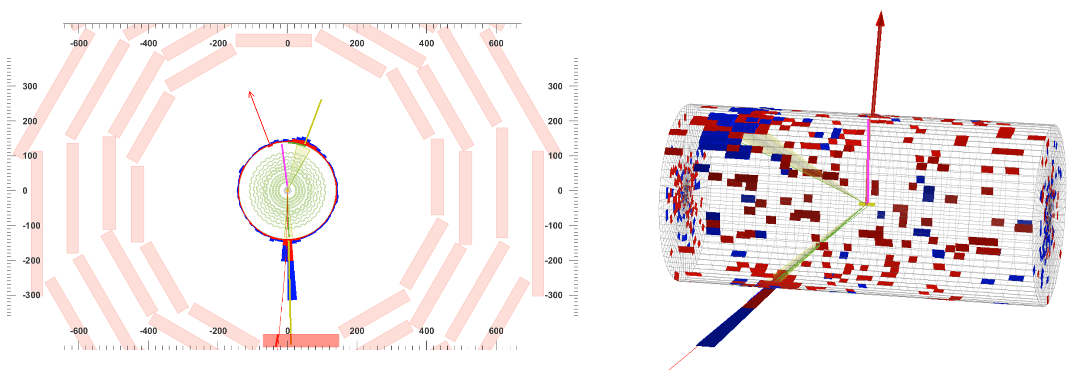

Figure 7.13: A $W \to \tau\nu$ event in which the tau decay products include a charged pion. The pion track has been highlighted in magenta. The reconstructed p_T of the track is 74.8 GeV, but the generated p_T is only 15.2 GeV. $E_{\text{calo}}^{\Delta R<0.5}$ is 8.1 GeV. Since the p_T has been mismeasured, this track passes the *Disappearing Track* criteria.

is increased. Since this background is predominantly for tracks that have 5 or 6 valid hits, we require at least 7 valid hits in the *Candidate Track* sub-sample to eliminate this background.

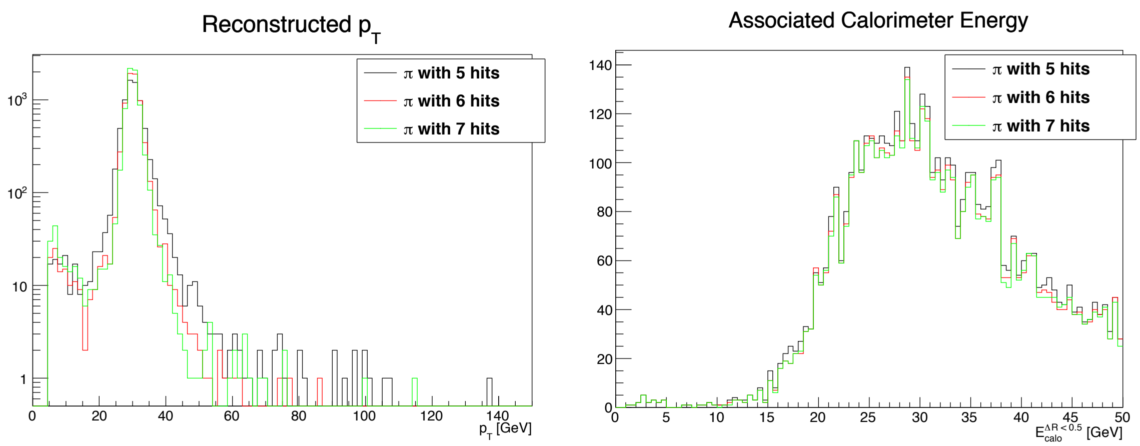

Figure 7.14: Reconstructed p_T for tracks from the pion single particle sample, with generated p_T of 30 GeV (left). $E_{\text{calo}}^{\Delta R<0.5}$ spectrum for tracks from the pion single particle sample (right).

Lastly, a pion from a $\tau \to \pi\nu$ decay can pass the $N_{\text{miss}}^{\text{outer}}$ criterion if it undergoes a nuclear interaction. An example event display is shown in Figure 7.12.

7.5 Fake Tracks

Fake tracks are formed from combinations of hits that are not produced by a single particle and can easily mimic a disappearing track.

To obtain a sample of fake tracks in W→lν+jets events, we require events that contain a track that is not matched to any generated particle . The track must also pass a modified *Candidate Track* criteria where the $|d_0|$, N_{hits}, and $N_{\text{miss}}^{\text{middle}}$ requirements have been removed. Most of these tracks have only three or four valid hits, as shown in Figure 7.15 and are effectively rejected by the *Candidate Track* selection criterion of $N_{\text{hits}} \geq 7$. Fake tracks typically have many missing outer hits and little associated calorimeter energy, as shown in Figure 7.16. Thus, those that survive the *Candidate Track* criteria also unfortunately pass the additional *Disappearing Track* criteria with high efficiency.

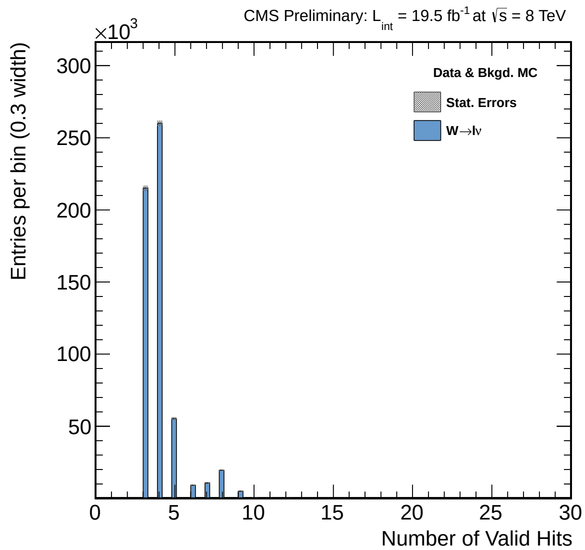

Figure 7.15: The number of valid hits, for fake tracks passing the *Candidate Track* criteria without the $|d_0|$, N_{hits}, and $N_{\text{miss}}^{\text{middle}}$ requirements.

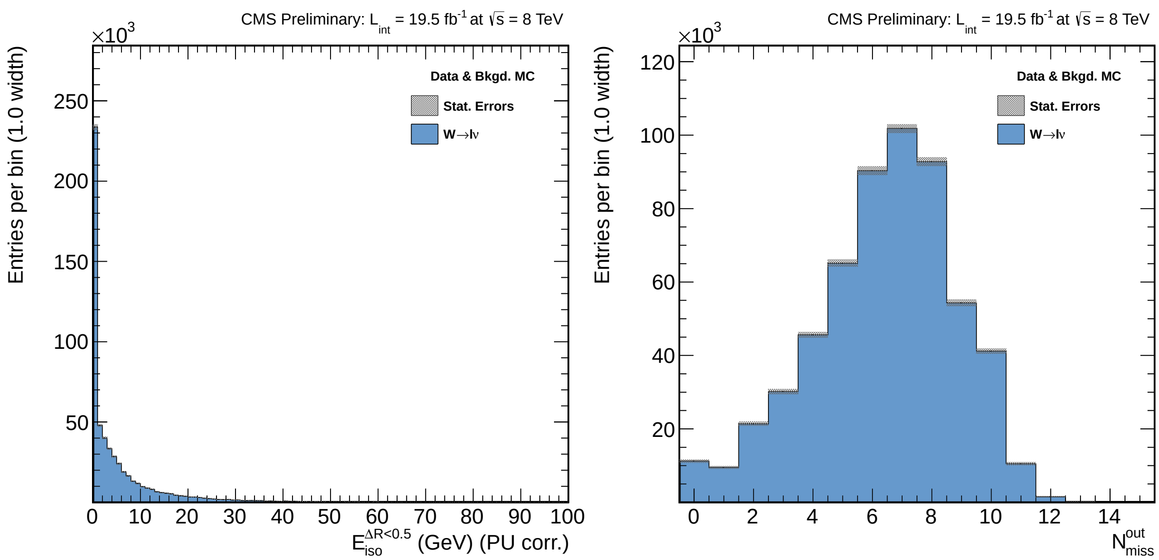

Figure 7.16: Distributions of $E_{\rm calo}^{\Delta R<0.5}$ and $N_{\rm miss}^{\rm outer}$ for fake tracks passing the *Candidate Track* criteria without the $|d_0|$, $N_{\rm hits}$, and $N_{\rm miss}^{\rm middle}$ requirements.

Chapter 8

Background estimates and associated systematic uncertainties

For each of the background sources described in Sections 7.2 to 7.5 the yield in the *Disappearing Track* subsample is estimated. The dominant source of background in this search arises from $W \to \ell\nu$ events.

One of the critical variables used to isolate signal from the lepton backgrounds, $N_{\rm miss}^{\rm outer}$, is not well-modeled by the Monte Carlo (MC). Therefore, to estimate the contributions of these backgrounds we have developed a data/MC hybrid background estimation method that does not depend on the MC for the simulation of $N_{\rm miss}^{\rm outer}$. We only rely on the MC to simulate the lepton inefficiency, i.e. the probability to survive the lepton veto, and, for electrons and taus, the probability to pass the $E_{\rm calo}^{\Delta R<0.5}$ requirement. The efficiency to pass the $N_{\rm miss}^{\rm outer}$ cut and all other selection criteria is taken directly from the data.

We estimate the lepton backgrounds as the product of the data yield in the *Lepton Control Samples* and the lepton inefficiency determined by MC. The lepton inefficiency is computed as the ratio of the number of events with a track matched to the given lepton in the *Disappearing Track* subsample to that in the corresponding control sample. We expect the MC to simulate the lepton inefficiency with reasonable accuracy. We assess its agreement with the data by using a standard tag and probe method to obtain samples of probe tracks produced by a known particle. We use the data/MC comparison of the lepton inefficiency in the lepton tag and probe samples to assess the systematic uncertainty in the simulated inefficiency in the search sample. The lepton background estimates and their associated uncertainties are discussed in detail in Sections 8.1 to 8.6

The fake track background is estimated with a method that is entirely data-driven. We estimate the fake track background as the product of the data yield in the *Kinematic Selection Sample* and the fake track rate determined in data as the probability of event to contain a reconstructed fake track that passes the *Disappearing Track* selection. We assess the uncertainty on the fake track estimate by comparing the fake track rate in *Muon Fake Track Control Sample* and *Electron Fake Track Control Sample* to that in the search sample for tracks that have exactly 5 valid hits. These are discussed in detail in Sections 8.7 and 8.8.

8.1 Electrons

After applying the electron veto as well as the fiducial cuts motivated in Section 7.2, the background from electrons is largely rejected. The remaining electron background is estimated as $N^e = N^e_{ctrl} P^e$, where N^e_{ctrl} is the data yield in the *Electron Control Sample* and P^e is the electron inefficiency determined with MC. The inefficiency P^e is the probability for a track from an electron to survive the electron veto and the $E_{\text{calo}}^{\Delta R<0.5}$ cut, after passing all other *Disappearing Track* criteria. No events with a track matched to an electron are present in the MC *Disappearing Track* subsample. We determine P^e with the W→lν+jets MC, which comprises 84% of the *Electron Control Sample* as shown in Figure 8.1. The upper limit on the electron inefficiency is determined with the MC to be $P^e < 6.3 \times 10^{-5}$, based on the yields given in Table 8.1.

The data yield in the *Electron Control Sample* is $N^{e}_{ctrl} = 7785$ events. From these inputs, we compute the 68% C.L. upper limit of the electron background estimate to be $N_e < 0.49_{stat}$ events, as given in Table 8.2. We assess the systematic uncertainty on this estimate in the following section.

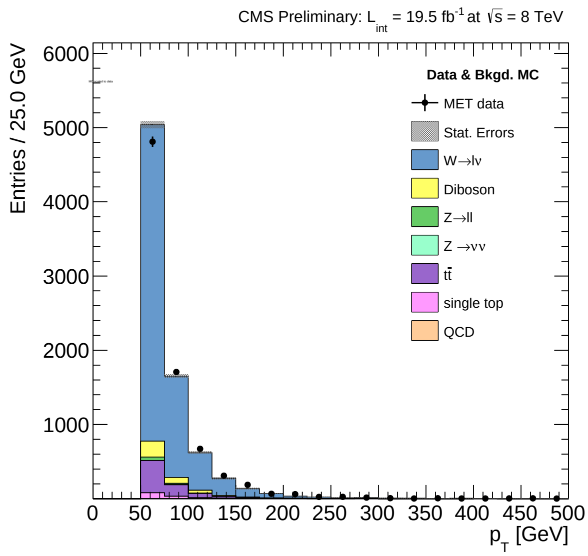

Figure 8.1: The transverse momentum of tracks in the *Electron Control Sample*. The MC has been normalized to the yield of the data.

Table 8.1: Electron inefficiency derived from the unweighted yields of W→lν+jets MC events in the *Disappearing Track* subsample and *Electron Control Sample*.

$N^{e}_{\rm ctrl}$ (MC)	18104
N^{e} (MC)	< 1.1
$P^{e} = N^{e}/N^{e}_{\rm ctrl}$	$< 6.3 \times 10^{-5}$

Table 8.2: Electron background estimate.

N^e_{ctrl} (data)	7785
P^e (MC)	$< 6.3 \times 10^{-5}$
N^e	< 0.49

8.2 Electron estimate systematic uncertainty

To assess the systematic uncertainty in P^e, the electron inefficiency is calculated in the *Electron Tag and Probe Sample* sample. In this sample, the electron inefficiency is computed as $P^e = N^{e,\text{T\&P}}/(2N^{e,\text{T\&P}}_{\text{ctrl}})$, where $N^{e,\text{T\&P}}_{\text{ctrl}}$ is the number of events in the *Electron Tag and Probe Sample* sample, and $N^{e,\text{T\&P}}$ is the number of those events that contain a probe track that is produced by an electron and that survives the electron veto and the $E^{\Delta R<0.5}_{\text{calo}}$ requirement. A factor of 2 is included in the inefficiency calculation to account for the possibility of either of the electrons to fail the identification. Figure 8.2 shows that the sample retains 99% purity even after the electron veto and $E^{\Delta R<0.5}_{\text{calo}}$ cuts are applied. P^e is $(1.70 \pm 0.25) \times 10^{-5}$ in the data and $(1.98 \pm 0.26) \times 10^{-5}$ in the MC. The values used to calculate P^e are shown in Table 8.3. The ratio of P^e between data and MC in the *Electron Control Sample* is 0.86 ± 0.17. The systematic uncertainty is taken as the largest one-sigma difference of this ratio from unity, or 31%.

The upper limit including statistical and systematic uncertainties is calculated according to Cousins and Highland [68], namely, for 0 observed events,

$$U_{\text{stat+syst}} = U_{\text{stat}}(1 + U_{\text{stat}}\sigma^2/2) \tag{8.1}$$

where U_{stat} is the upper limit excluding the systematic uncertainty, and σ is the relative systematic uncertainty. From this formulation we arrive at a final electron background estimate of $N_e < 0.50_{\text{stat+syst}}$ events.

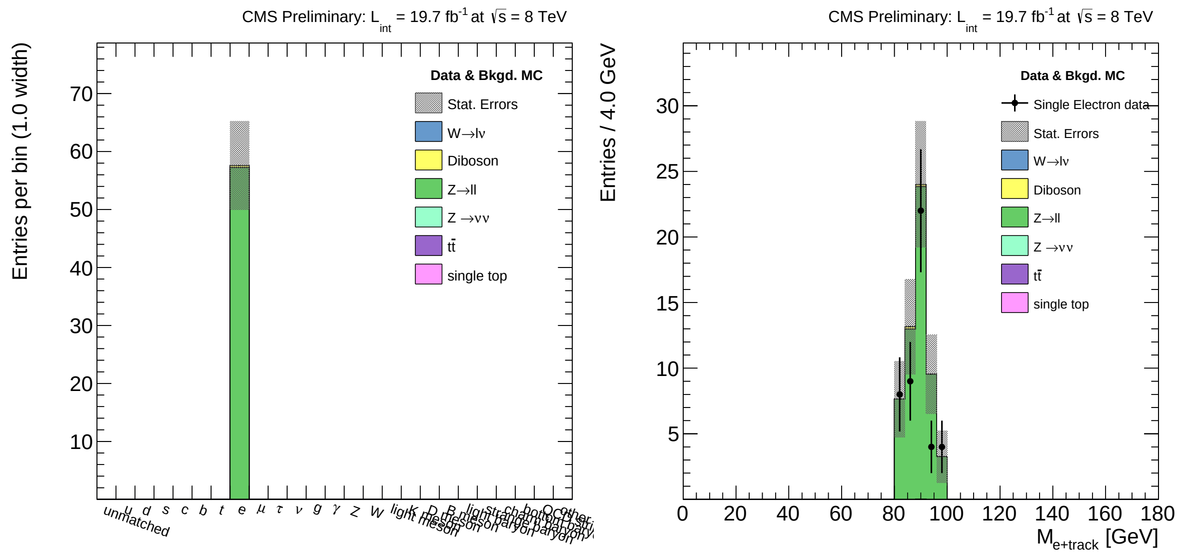

Figure 8.2: The identity of the generated particle matched to the candidate track (left), and invariant mass of the tag electron and probe track (right), for events in the *Electron Tag and Probe Sample* sample for which the probe track survives the electron veto and the $E_{\rm calo}^{\Delta R<0.5}$ cut.

Table 8.3: Electron inefficiency determined with the *Electron Tag and Probe Sample*.

	Data	MC
$N_{\rm ctrl}^{e,\rm T\&P}$: Total yield	$(1.384 \pm 0.001) \times 10^6$	$(1.457 \pm 0.001) \times 10^6$
$N^{e,\rm T\&P}$: Probe track passes e veto and $E_{\rm calo}^{\Delta R<0.5}$ cut	47.0 ± 6.9	57.6 ± 7.6
$P^e = N^{e,\rm T\&P}/(2N_{\rm ctrl}^{e,\rm T\&P})$	$(1.7 \pm 0.25) \times 10^{-5}$	$(1.98 \pm 0.26) \times 10^{-5}$

8.3 Muons

After applying the muon veto as well as the fiducial cuts motivated in Section 7.3, the background from muons is largely rejected. The remaining muon background is estimated as $N^\mu = N_{\rm ctrl}^\mu P^\mu$, where $N_{\rm ctrl}^\mu$ is the data yield in the *Muon Control Sample*, and P^μ is the muon inefficiency calculated by the MC. The muon inefficiency P^μ is defined as the probability of a track from a muon to survive the muon veto after passing all other *Disappearing Track* criteria. We determine P^e with the W→lν+jets

MC, which comprises 85% of the *Muon Control Sample* as shown in Figure 8.3. There is one unweighted W→lν+jets MC event in the *Disappearing Track* subsample. The muon inefficiency is determined to be $P^{\mu} = (1.6^{+3.6}_{-1.3}) \times 10^{-4}$, based on the ratio of the muon yields in the *Disappearing Track* subsample and the *Muon Control Sample* given in Table 8.4. The number of data events in the *Muon Control Sample* is $N^{\mu}_{\rm ctrl} = 4138$ events, as given in Table 8.5. From these inputs, the muon background estimate is determined to be $N^{\mu} = 0.64(^{+1.5}_{-0.53})_{\rm stat}$ events. We assess the systematic uncertainty on this estimate in the following section.

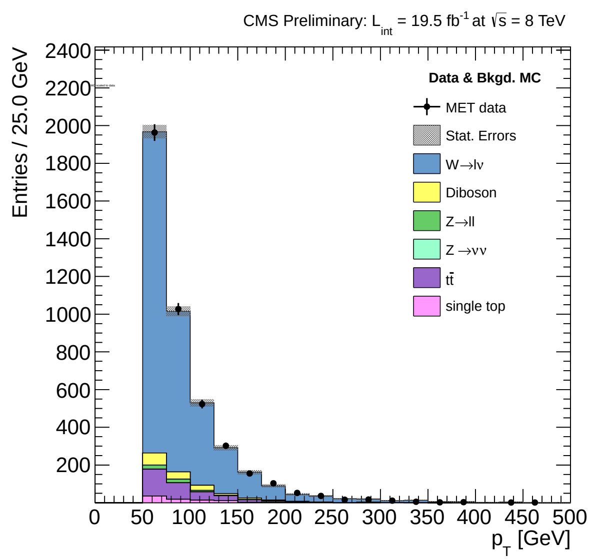

Figure 8.3: The transverse momentum of tracks in the *Muon Control Sample*. The MC has been normalized to the yield of the data.

8.4 Muon estimate systematic uncertainty

The systematic uncertainty in the MC simulation of P^{μ} is assessed based on the difference between data and MC in the muon inefficiency calculated in the *Muon*

Table 8.4: Muon inefficiency derived from the unweighted yields of W→lν+jets MC events in the *Disappearing Track* subsample and the *Muon Control Sample*.

N^{μ}_{ctrl} (MC)	6421
N^{μ} (MC)	$1.0^{+2.3}_{-0.83}$
$P^{\mu} = N^{\mu}/N^{\mu}_{\text{ctrl}}$	$(1.6^{+3.6}_{-1.3}) \times 10^{-4}$

Table 8.5: Muon background estimate.

N^{μ}_{ctrl} (data)	4138
P^{μ} (MC)	$(1.6^{+3.6}_{-1.3}) \times 10^{-4}$
N^{μ}	$0.64^{+1.5}_{-0.53}$

Tag and Probe Sample. In this sample, the muon inefficiency is computed as $P^{\mu} = N^{\mu,\text{T\&P}}/(2N^{\mu,\text{T\&P}}_{\text{ctrl}})$, where $N^{\mu,\text{T\&P}}_{\text{ctrl}}$ is the number of events in the *Muon Tag and Probe Sample*, and $N^{\mu,\text{T\&P}}$ is the number of those events that contain a probe track that is produced by a muon and that survives the muon veto. A factor of 2 is included in the inefficiency calculation to account for the possibility of either of the muons to fail the identification. In the *Muon Tag and Probe Sample*, over 99% of the probe tracks are matched to muons. The probe tracks that survive the muon veto are still predominantly matched to muons, as shown in Figure 8.4. The non-muon contamination predicted by the MC is subtracted from both the data and MC yields to obtain the number of tracks matched to a muon. The muon inefficiencies are compared in Table 8.6. P^{μ} is $(1.87 \pm 0.53) \times 10^{-5}$ in the data and $(2.26 \pm 0.61) \times 10^{-5}$ in the MC. The ratio of P^{μ} between data and MC in the *Muon Tag and Probe Sample* is 0.83 ± 0.32. The systematic uncertainty in P^{μ} is taken as the largest one-sigma deviation from unity in the ratio of the inefficiencies, which is 50%.

Adding this systematic uncertainty to the central value determined above, we arrive at a final muon background estimate of $N^{\mu} = 0.64(^{+1.47}_{-0.53})_{\text{stat}} \pm 0.32_{\text{syst}}$ events.

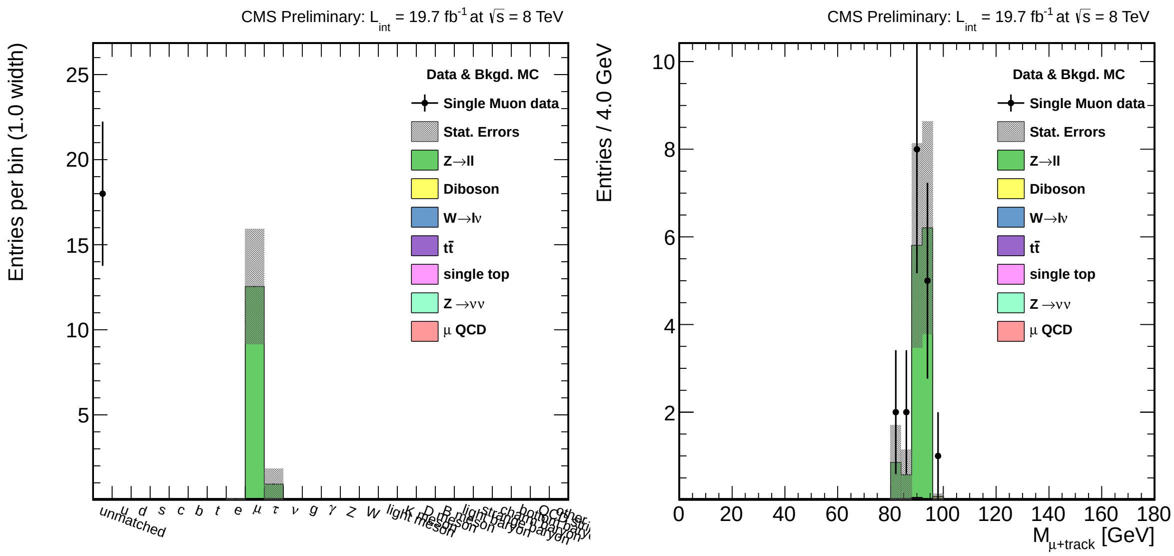

Figure 8.4: The identity of the generated particle matched to the candidate track (left), and invariant mass of the tag muon and probe track (right), for events in the *Muon Tag and Probe Sample* for which the probe track survives the muon veto.

Table 8.6: Muon inefficiency, determined with the *Muon Tag and Probe Sample*, with and without the μ veto applied to the probe track.

	Data	MC
$N^{\mu,\mathrm{T\&P}}_{\mathrm{ctrl}}$: Total yield	376693.0 ± 614.0	276786.0 ± 499.0
$N^{\mu,\mathrm{T\&P}}$: Probe track passes μ veto	15.0 ± 3.9	13.5 ± 3.5
non-μ yield	0.92 ± 0.92	0.92 ± 0.92
$N^{\mu,\mathrm{T\&P}}$: μ yield	14.1 ± 4.0	12.5 ± 3.4
$P^{\mu} = N^{\mu,\mathrm{T\&P}}/(2N^{\mu,\mathrm{T\&P}}_{\mathrm{ctrl}})$	$(1.87 \pm 0.53) \times 10^{-5}$	$(2.26 \pm 0.61) \times 10^{-5}$

8.5 Taus

As discussed in Section 7.4, the potential source of background from single prong tau decays in which the p_T of the pion is mismeasured is significantly reduced after requiring at least 7 valid hits for each candidate track. Any remaining tau background is estimated as $N^{\tau} = N^{\tau}_{ctrl} P^{\tau}$, where N^{τ}_{ctrl} is the yield in the *Tau Control Sample* and

P^τ is the tau inefficiency. The inefficiency P^τ is the probability of a track from a tau to survive the tau veto and the $E_{\mathrm{calo}}^{\Delta R<0.5} < 10$ GeV requirement, after passing all other *Disappearing Track* criteria. We determine P^τ with the W→lν+jets MC, which comprises 75% of the *Tau Control Sample*, as shown in Figure 8.5. The upper limit on the tau inefficiency is calculated to be $P^\tau \leq 0.019$, as shown in Table 8.7. The data yield in the *Tau Control Sample* is $N^\tau_{ctrl} = 29$ events. From these inputs, we compute the central value of the tau background estimate to be $N_\tau < 0.55_{\mathrm{stat}}$ events, as given in Table 8.8. We assess the systematic uncertainty on this estimate in the following section.

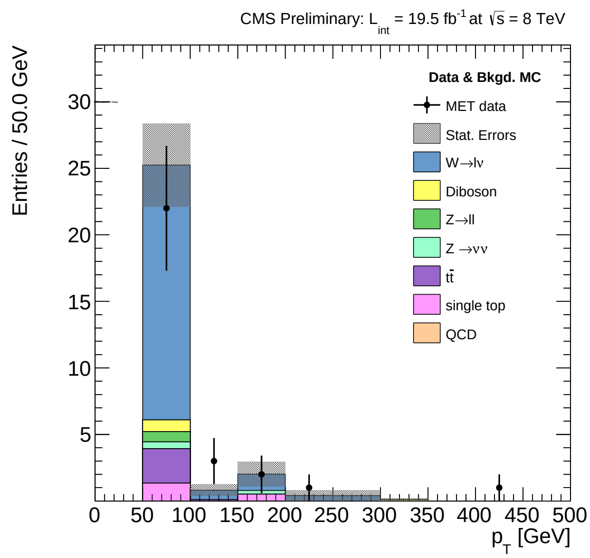

Figure 8.5: The transverse momentum of candidate tracks in the *Tau Control Sample*. The MC has been normalized to the yield of the data.

Table 8.7: Tau inefficiency derived from the unweighted yields of W→lν+jets MC events in the *Disappearing Track* subsample and the *Tau Control Sample*.

$N^{\tau}_{\rm ctrl}$ (MC)	60
N^{τ} (MC)	< 1.1
$P^{\tau} = N^{\tau}/N^{\tau}_{\rm ctrl}$	< 0.019

Table 8.8: Tau background estimate.

$N^{\tau}_{\rm ctrl}$ (data)	29
P^{τ} (MC)	< 0.019
N^{τ}	< 0.55

8.6 Tau estimate systematic uncertainty

The systematic uncertainity in the tau inefficiency is assessed by calculating P^{τ} in the *Tau Tag and Probe Sample*. In this sample, the tau inefficiency is computed as $P^{\tau} = N^{\tau,\rm T\&P}/(2N^{\tau,\rm T\&P}_{\rm ctrl})$, where $N^{\tau,\rm T\&P}_{\rm ctrl}$ is the number of events in the *Tau Tag and Probe Sample* sample, and $N^{\tau,\rm T\&P}$ is the number of those events that contain a probe track which survives the tau veto. A factor of 2 is included in the inefficiency calculation to account for the possibility of either of the taus to fail the identification. The impurity from jet contamination is taken from MC (see Figure 8.6). After subtracting the non-tau contribution, P^{τ} is found to be 0.187 ± 0.016 in data and 0.150 ± 0.006 in the MC. The values used to calculate P^{τ} are shown in Table 8.9. The ratio of P^{τ} between data and MC is 1.25 ± 0.12. The relative systematic uncertainty in P^{τ} is taken as the largest one-sigma difference from unity in the ratio, which is 36%. Using the Cousins and Highland [68] prescription, we determine the tau background estimate upper limit including statistical and systematic uncertainties, which is $N_{\tau} < 0.57_{\rm stat+syst}$ events.

Table 8.9: Tau inefficiency determined with the *Tau Tag and Probe Sample*. The non-tau contribution is predominantly from jet contamination and is taken from the MC.

	Data	MC
$N^{\tau,\mathrm{T\&P}}_{\mathrm{ctrl}}$: Total yield	5188 ± 72	5880 ± 126
$N^{\tau,\mathrm{T\&P}}$: Probe track passes τ veto	1420 ± 38	1340 ± 79
non-τ yield	452 ± 74	452 ± 74
$N^{\tau,\mathrm{T\&P}}$: τ yield	972.2 ± 83	885 ± 28
$P^{\tau} = N^{\tau,\mathrm{T\&P}}/N^{\tau,\mathrm{T\&P}}_{\mathrm{ctrl}}$	0.187 ± 0.016	0.150 ± 0.006

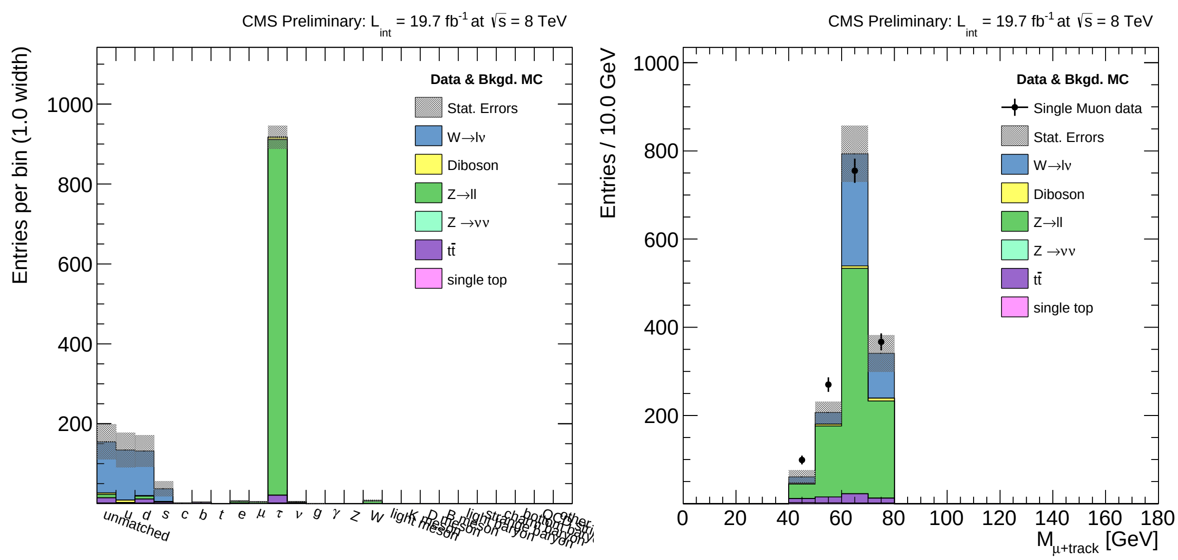

Figure 8.6: The identity of the generated particle matched to the probe track (left) and the invariant mass of the tag muon and probe track (right). Both figures correspond to events in the *Tau Tag and Probe Sample* sample in which the probe track survives the tau veto. The tau purity is 69%.

8.7 Fake tracks

The fake track background is estimated entirely from the data. It is calculated as $N^{\mathrm{fake}} = N^{\mathrm{kin}} P^{\mathrm{fake}}$, where N^{kin} is the number of events in the *Kinematic Selection Sample* and P^{fake} is the fake track rate, defined as the probability of an event to contain a reconstructed fake track that passes the *Disappearing Track* selection.

The fake track rate P^{fake} is determined as the fraction of events in the $Z \to \mu\mu$ *Control Sample* and in the $Z \to ee$ *Control Sample* that contain a track that passes the *Disappearing Track* criteria. We calculate the fake track rate as $P^{\text{fake}} = N^{\text{fake}}_{\text{ctrl}}/N^{Z\to ll}$, where $N^{\text{fake}}_{\text{ctrl}} = 2$ is the sum of the number of events in the *Muon Fake Track Control Sample* and *Electron Fake Track Control Sample*. Likewise, $N^{Z\to ll}$ is the sum of the number of events in the $Z \to \mu\mu$ *Control Sample* and $Z \to ee$ *Control Sample*. It is found to be $P^{\text{fake}} = (2.0^{+2.7}_{-1.3}) \times 10^{-7}$, as given in Table 8.10. The data yield in the *Kinematic Selection Sample* is $N^{\text{kin}} = 1.77 \times 10^6$ events as shown in Table 8.11. From these inputs, we compute the central value of the fake track background estimate to be $N_{\text{fake}} = 0.36(^{+0.47}_{-0.23})_{\text{stat}}$ events. We assess the systematic uncertainty on this estimate in the following section.

Table 8.10: Determination of the fake track rate P^{fake} from the yield in the *Muon Fake Track Control Sample* and *Electron Fake Track Control Sample*, with and without the requirement of a *Disappearing Track*.

$N^{\text{Z}\to\text{ll}}$	9.84×10^6
$N^{\text{fake}}_{\text{ctrl}}$	2.0
$P^{\text{fake}} = N^{\text{fake}}_{\text{ctrl}}/N^{\text{Z}\to\text{ll}}$	$(2.0^{+2.7}_{-1.3}) \times 10^{-7}$

Table 8.11: Fake track background estimate.

$N^{\text{fake}}_{\text{ctrl}}$ (data)	1.77×10^6
P^{fake} (data)	$(2.0^{+2.7}_{-1.3}) \times 10^{-7}$
N^{fake}	$0.36^{+0.47}_{-0.23}$

8.8 Fake track estimate systematic uncertainty

The fake track rate P^{fake} is small for the *Disappearing Track* selection, but increases dramatically for tracks with fewer than 7 associated hits. The distribution of the number of valid hits associated to fake tracks that have at least 3 associated hits and that pass all other *Disappearing Track* criteria is shown in Figure 8.7. The tracks with 4 hits are the dominant contribution. The fake track rate for tracks with exactly 4 hits is consistent among various MC samples, as shown in Figure 8.8. Because the fake track rate is similar in events with different underlying physics processes, it is expected to be similar in the $Z \to \mu\mu$ *Control Sample*, $Z \to ee$ *Control Sample*, and in the *Kinematic Selection Sample*. The fake track rate for fake tracks with between 3 and 6 hits is consistent between these samples, as shown in Figure 8.9. We use the bin for tracks with 5 hits to assess the systematic uncertainty in the fake track background estimate. The purity of the sample of fake tracks is assessed for tracks with 4 hits based on $\Delta\phi$, the difference in azimuthal angle between the candidate track momentum and the $\not{E}_T$ vector. This angle is uniform for fake tracks that are uncorrelated with the physics process of the event. Figure 8.10 shows that in the *Disappearing Track* subsample modified to require exactly 4 hits, the data and background have a uniform distribution of $\Delta\phi$, while the signal tracks more commonly have $\Delta\phi$ close to 0. In the *Muon Fake Track Control Sample* modified to require exactly 4 hits, the difference in azimuthal angle between the candidate fake track and the dimuon pair shown in Figure 8.11 is also uniform.

As mentioned previously, we use tracks with 5 hits to assess the systematic uncertainty. The fake track rate for tracks with five hits is $(9.06 \pm 2.3) \times 10^{-6}$ in the *Kinematic Selection Sample* and $(10.2 \pm 1) \times 10^{-6}$ in the composite $Z \to \mu\mu$ *Control Sample* and $Z \to ee$ *Control Sample.*The ratio between the rates in these two samples is 0.89 ± 0.24. The largest one-sigma deviation from unity in the ratio of these fake track rates, 35%, is taken as the systematic uncertainty in the fake track background estimate.

Adding this systematic uncertainty to the central value determined above, we arrive at a final fake track background estimate of $N_{\text{fake}} = 0.36(^{+0.47}_{-0.23})_{\text{stat}} \pm 0.13_{\text{syst}}$ events.

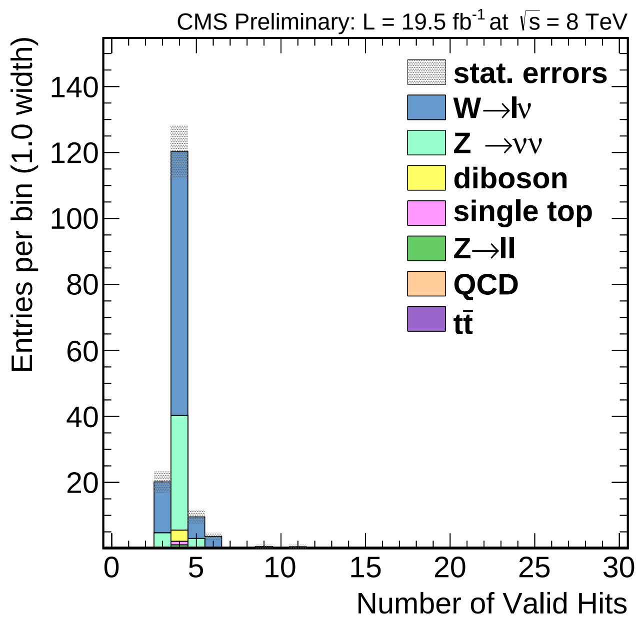

Figure 8.7: The number of valid hits associated to fake tracks with at least 3 hits that pass all other *Disappearing Track* subsample criteria.

8.9 Background estimate validation

The methods used to estimate the backgrounds in the *Disappearing Track* subsample are tested in the *Candidate Track* subsample and in the $E_{\text{calo}}^{\Delta R<0.5}$ and $N_{\text{miss}}^{\text{outer}}$ sideband samples. In each sample, the backgrounds are estimated using the methods described above. In addition to the raw event yields, the p_T distribution is also obtained for each

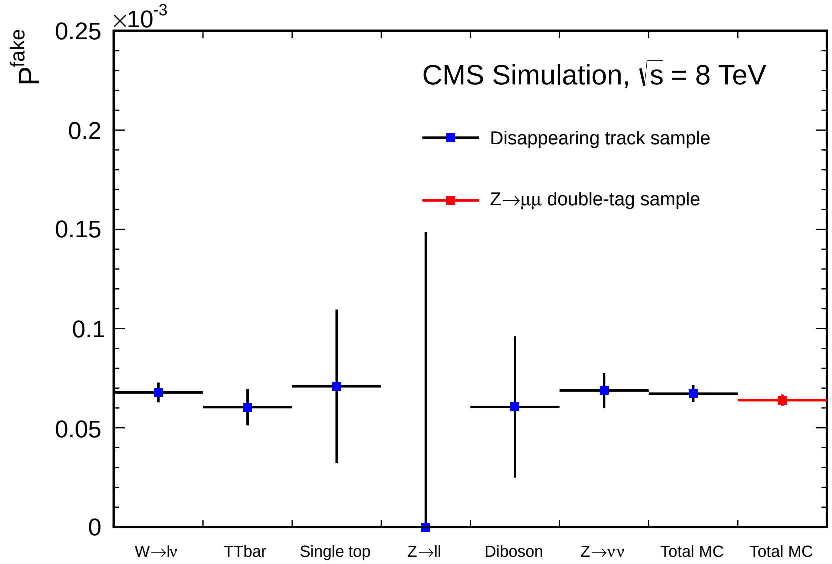

Figure 8.8: The fake track rate P^{fake} for tracks with exactly four associated hits in samples that pass all other criteria of the *Disappearing Track* subsample and the *Muon Fake Track Control Sample*.

background category. For the lepton backgrounds, the shape of the p_T distribution is taken from the corresponding lepton control sample. For the fake track background, the shape of the p_T distribution is taken from that of the tracks in the *Muon Fake Track Control Sample*. The shapes of the p_T distributions are normalized by the estimated background yield.

The p_T distribution of the data in the *Candidate Track* subsample is compared with the estimated backgrounds in Figure 8.12. The p_T distributions of the data in the sideband samples are compared with the estimated backgrounds in Figure 8.13. The data yields and estimates in each of these samples are consistent within the uncertainties, as shown in Table 8.12.

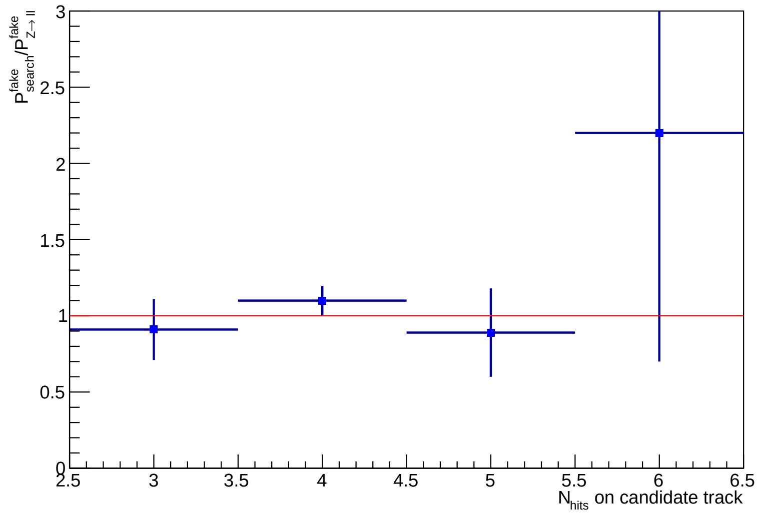

Figure 8.9: The ratio of the fake track rate P^{fake} in data between the *Kinematic Selection Sample* and the $Z \to ll$ *Control Sample*, for different numbers of hits on the fake track.

Table 8.12: The data yields and estimated backgrounds in the *Candidate Track* subsample and sideband samples.

Sample	data	estimate	data/estimate
Candidate Track sample	59	49.0 ± 5.7	1.20 ± 0.21
$E_{\text{calo}}^{\Delta R<0.5}$ sideband sample	197	195.4 ± 13.0	1.01 ± 0.10
$N_{\text{miss}}^{\text{outer}}$ sideband sample	112	102.9 ± 8.8	1.09 ± 0.14

8.10 Summary of background systematic uncertainties

The systematic uncertainties in the estimates of the backgrounds are summarized in Table 8.13.

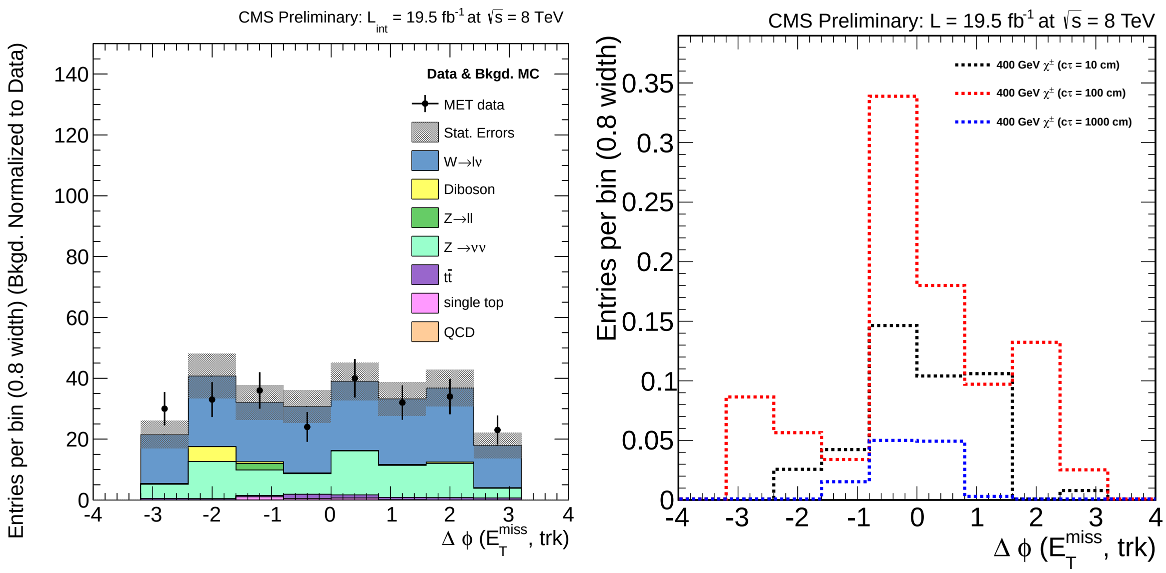

Figure 8.10: The difference in azimuthal angle between the candidate fake track and the $\not\!\!E_T$ vector, for the tracks with 4 hits in events that pass all other *Disappearing Track* subsample criteria. The MC is normalized to the area of the data.

Table 8.13: The fractional systematic uncertainties in the background estimates.

	Systematic uncertainty
electron estimate	31%
muon estimate	50%
tau estimate	36%
fake track estimate	35%

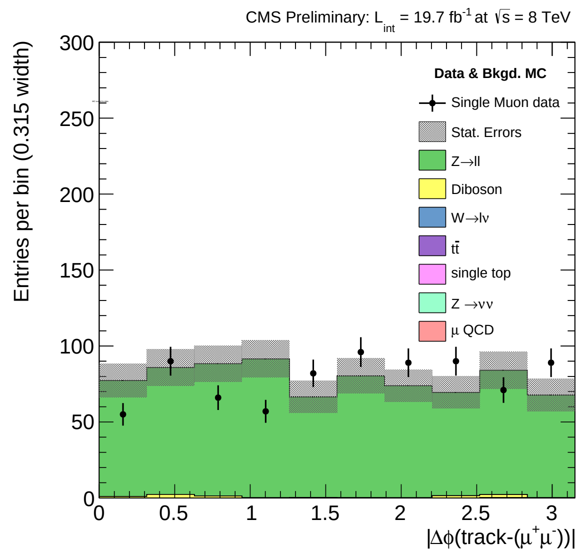

Figure 8.11: The difference in azimuthal angle between the candidate fake track and the dimuon pair, for tracks with 4 hits in events that pass all other *Muon Fake Track Control Sample* criteria. The MC is normalized to the area of the data.

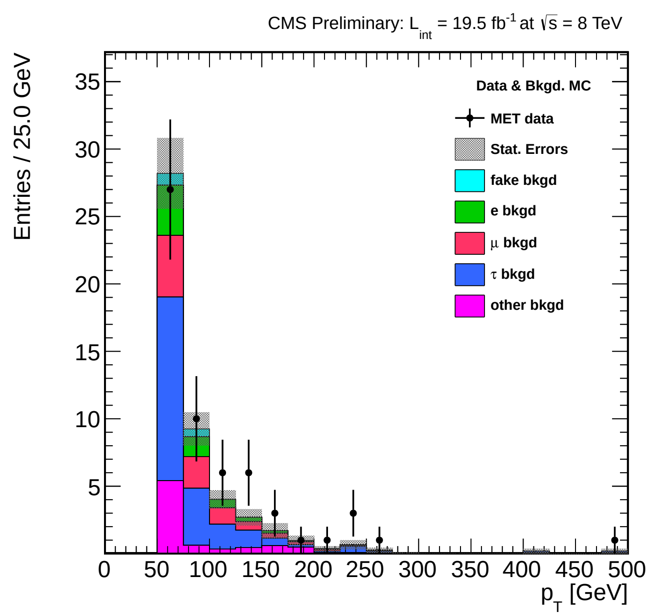

Figure 8.12: The transverse momentum of tracks in the *Candidate Track* subsample. The data are compared with the background estimate.

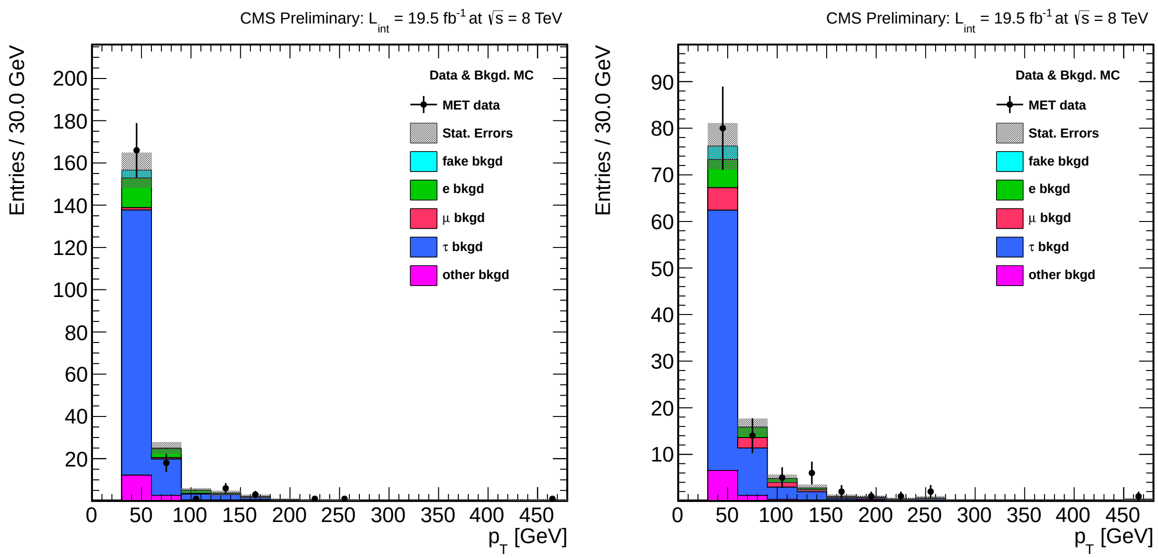

Figure 8.13: The transverse momentum of tracks in the $E_{\mathrm{calo}}^{\Delta R<0.5}$ sideband sample (left), and in the $N_{\mathrm{miss}}^{\mathrm{outer}}$ sideband sample (right) The data are compared with the background estimate.

Chapter 9
Additional systematic uncertainties

In this section, we study the remaining sources of systematic uncertainty in the analysis, namely the integrated luminosity and the signal efficiency.

The integrated luminosity of the 8 TeV pp collision data is measured with a pixel cluster counting method, for which the uncertainty is 2.6% [69].

9.1 Initital state radiation

As discussed in Section 5.2, we trigger on events in which the dichargino system recoils from one or more ISR jets, and the resultant $\not\!\!E_T$ is directly proportional to the p_T of the dichargino system, as shown in Figure 9.1.

To asess the systematic uncertainty associated with the simulation of ISR, we compare the recoil from ISR jets in data with Pythia 6 MC in a $Z \to \mu\mu$ +jets sample, a study similar to that presented in [70]. We select $Z \to \mu\mu$ +jets events by requiring two tightly identified, isolated leptons that are opposite in sign and have an invariant mass between 80–100 GeV, consistent with a Z boson decay. In addition, we require at least one loosely identified jet with $p_T > 30$ GeV. The data are taken from the `/DoubleMuParked/Run2012*-22Jan2013-v1/AOD` datasets, and a $Z \to \mu\mu$ MC sample generated with Pythia 6 is used:

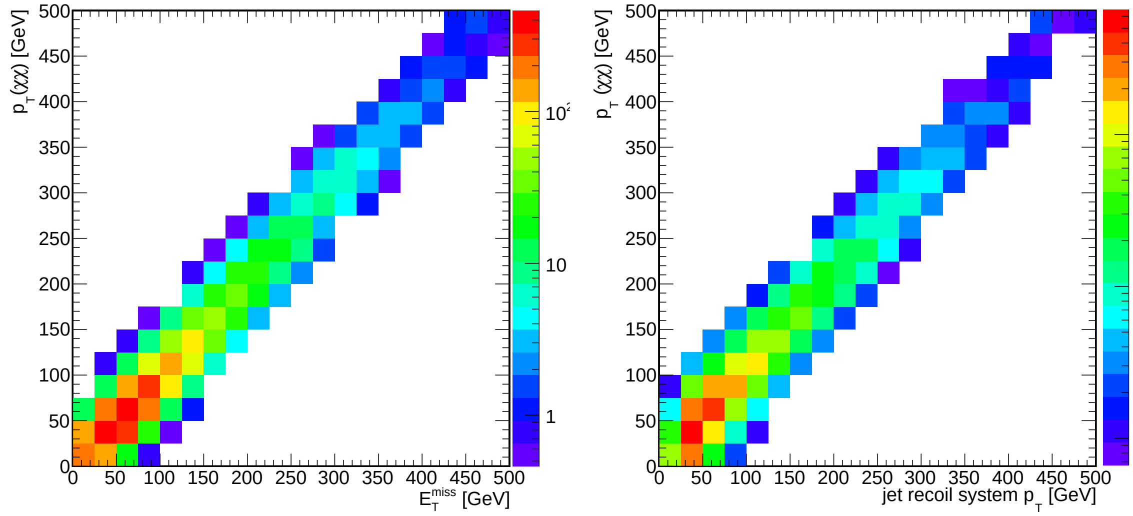

Figure 9.1: The p_T of the $\chi\chi$ system versus $\not\!\!E_T$ (left) and versus the jet recoil p_T (right), for generated events with a chargino mass of 247 GeV and lifetime of 1 ns that contain at least one jet passing the jet criteria defined in Section 6.2.

`/DYToMuMu_M_20_TuneZ2star_8TeV_pythia6_v2/Summer12_DR53X-PU_S10_START53_V7A-v1/AODSIM`

The other MC samples are the same as those listed in Table A.1. The MC is normalized to the yield of the data to focus on shape differences. In this $Z \to \mu\mu$ +jets sample Pythia predicts a softer dimuon p_T spectrum than that measured in the data, as shown in Figure 9.2. The ratio of data to MC in the dimuon p_T spectra is used to reweight the signal MC.

We define the systematic as the difference between the original signal efficiency, ϵ_{orig}, and the signal efficiency after reweighting, ϵ_{rwtd}. ϵ_{orig} is fraction of generated events that pass the *Disappearing Track* selection, and ϵ_{rwtd} is the fraction of generated events that pass the *Disappearing Track* selection after being reweighted by the ratio of data to MC in the $Z \to \mu\mu$ +jets sample. The difference in efficiencies is 3–11%, which is taken as the systematic uncertainty.

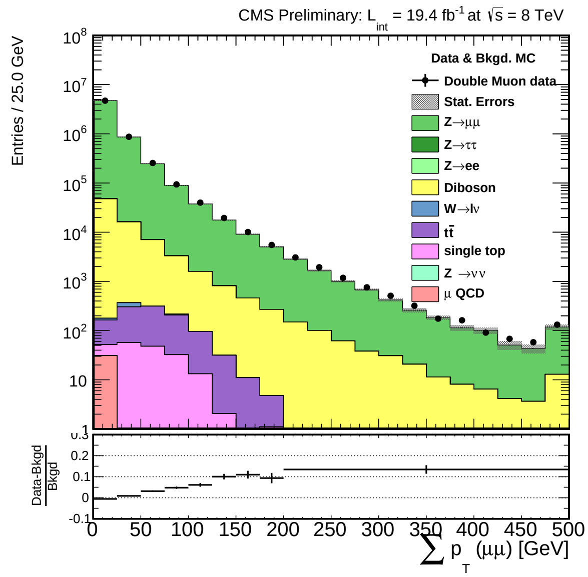

Figure 9.2: The distribution of the p_T of the dimuon system in the $Z \to \mu\mu$ +jets ISR sample; the MC yield has been normalized to that of the data. Events in the overflow have been added to the last bin.

9.2 Trigger efficiency

The uncertainty associated with the trigger efficiency is assessed by comparing the measured and predicted trigger effiency in a $W \to \mu\nu$ control sample. We first require all events to pass the `HLT_IsoMu24_eta2p1` trigger. Next, we apply all of the offline criteria of the *Candidate Track* subsample, excluding the muon veto and $\not\!\!E_T$ cut. In addition, we require exactly one muon in the event, to reduce the contamination from $Z \to \mu\mu$. Finally, we require that the difference in azimuthal angle between the muon and any jet in the event be less than 2.7, which is motivated by the HLT trigger filter in `HLT_MonoCentralPFJet80_PFMETnoMu95_NHEF0p95`. This filter requires the difference in azimuthal angle between the leading jet and any subleading jet to be less than 2.9, as discussed in Section 5.2. In a significant number of events, the muon and the jet are back to back, and the muon is classified as a jet. Without the

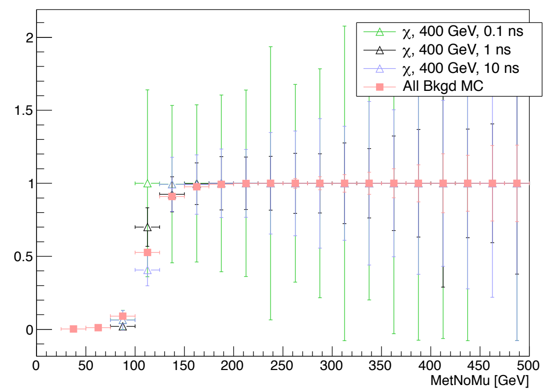

Figure 9.3: Trigger efficiency as a function of PFMetNoMu, calculated for the signal MC in the *Disappearing Track* sub-sample without the $\not\!\!E_T$ requirement, and for the background MC in the $W \to \mu\nu$ control sample. All background MC listed in Table A.1 are included with the dominant (90%) contribution coming from $W \to \mu\nu$ MC.

$|\Delta\phi(\text{muon, any jet})| < 2.7$ cut, these events fail this trigger filter and bias the trigger efficiency. After this selection, the sample is primarily composed of $W \to \mu\nu$ events, with 90% purity.

As shown in Figure 9.3, $W \to \mu\nu$ and signal have similar trigger efficiencies as a function of PFMetNoMu. In Figure 9.4, we compare the trigger efficiency in `SingleMu` data and background MC for events that pass the aforementioned cuts. The ratio of the trigger efficiency in data and simulation, as a function of PFMetNoMu, is applied as a reweighting factor to the signal events. The resultant change in the signal efficiency is 1–8%, which is taken as the systematic uncertainty associated with the trigger efficiency.

The trigger efficiency as a function of the p_T of the leading jet is $\sim 100\%$ for jet $p_T > 110$ GeV [65]. Since the offline selection requires the leading jet p_T to be greater than 110 GeV, a separate systematic uncertainty for the trigger efficiency as function of jet p_T is not calculated.

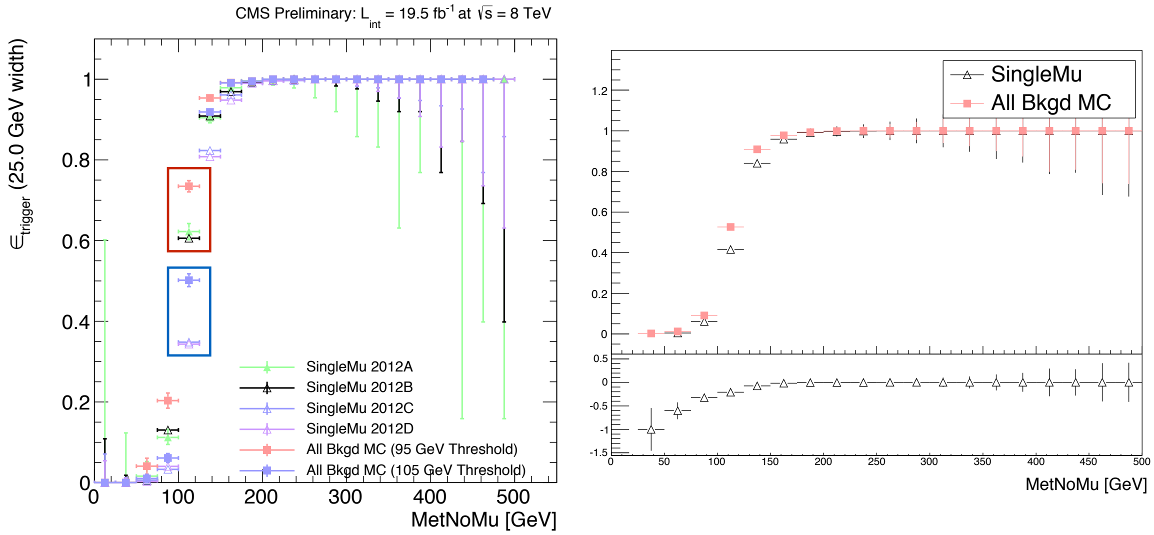

Figure 9.4: Left: Trigger efficiency as a function of PFMetNoMu, calculated for the `SingleMu` data and all background MC. In 2012A and 2012B, the lower threshold trigger, `HLT_MonoCentralPFJet80_PFMETnoMu95_NHEF0p95`, is available, and in 2012C and 2012D, the higher threshold trigger, `HLT_MonoCentralPFJet80_PFMETnoMu105_NHEF0p95` is used. Since this higher threshold trigger was not available in the background MC, we emulated this trigger using information stored in our ntuples. The details of the trigger emulation can be found in Appendix B. The largest difference between the lower threshold trigger and data has been boxed in red, and the largest difference between the higher threshold trigger and data has been boxed in blue. Right: Trigger efficiency for all `SingleMu` data and all background MC as a function of PFMetNoMu. This ratio is used to reweight the signal MC.

9.3 Jet energy scale, jet energy resolution, PDF, and pileup

We assess uncertainties due to the jet energy scale and resolution according to the official recommendations of the Jet/MET Group [71, 72]. The jet energy is varied up and down by one standard deviation. The signal yields change by less than 0–7% from the variations in the jet energy scale. For the uncertainty on jet energy resolution, the data/MC resolution correction factors are varied up and down by one sigma; the resultant uncertainty is 1–5%.

We assess the uncertainty associated with the parton distribution function (PDF) by following the official PDF4LHC recommendation [73, 74]. Events are reweighted with up/down variations of the eigenvectors of the CTEQ6.6, MSTW08, and NNPDF2.0 PDF set. The resultant acceptance uncertainties are between 1–10%.

The uncertainty associated with the modeling of the number of pile-up interactions is assessed with the recommended CMS procedure. The signal samples are reweighted to match target pile-up distributions in which the numbers of inelastic interactions are shifted up and down by the uncertainty. The variation in the signal acceptance is 0–2%.

9.4 Modeling of $E_{\text{calo}}^{\Delta R<0.5}$, $N_{\text{miss}}^{\text{outer}}$, $N_{\text{miss}}^{\text{inner}}$, and $N_{\text{miss}}^{\text{mid}}$

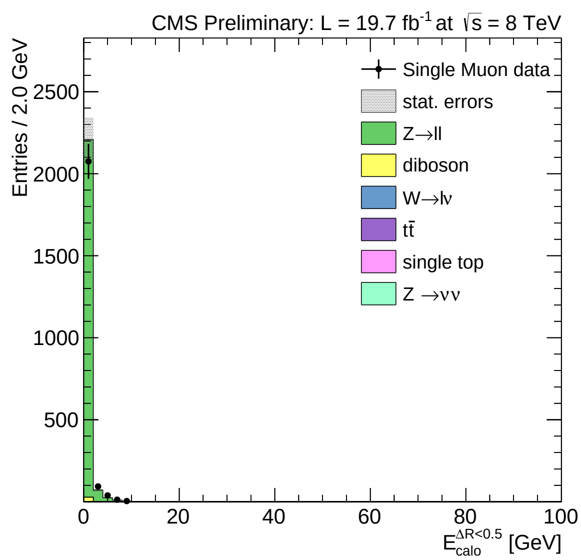

Figure 9.5: Distribution of $E_{\text{calo}}^{\Delta R<0.5}$ in the *Muon Fake Track Control Sample* with exactly 4 hits on the candidate track, after reweighting data and MC by the distribution of the signal MC (chargino with mass 400 GeVand lifetime 1 ns) in the *Disappearing Track* subsample.

The systematic uncertainty associated with the simulation of $E_{\text{calo}}^{\Delta R<0.5}$ is assessed by comparing the predicted and measured distributions in the *Muon Fake Track Control Sample*, as shown in Figure 9.5. In this sample, the efficiency of the $E_{\text{calo}}^{\Delta R<0.5} <$ 10 GeV requirement is larger for the data than for the simulation. The relative difference, 6%, is taken as the uncertainty associated with modeling $E_{\text{calo}}^{\Delta R<0.5}$.

The uncertainty associated with the modeling of $N_{\text{miss}}^{\text{outer}}$ is assessed by varying the $N_{\text{miss}}^{\text{outer}}$ distribution of the signal MC by 11%, the disagreement between data and MC in the $N_{\text{miss}}^{\text{outer}}$ distribution in a control sample of muon tracks. Since muons are predominantly affected by the algorithmic sources of missing outer hits described in Section 7.1, they reflect how well the $N_{\text{miss}}^{\text{outer}}$ distribution is modeled in MC. After this variation, the signal yields change by 0–7%.

We assess the systematic uncertainty in the signal efficiency associated with the simulation of missing inner and middle hits by comparing data and MC in the *Muon Control Sample*, with the cuts on missing inner and middle hits removed. The *Muon Control Sample* is used because the distribution of the number of missing middle and inner hits is similar for signal and for muons. The efficiencies to pass the requirements of zero missing inner and middle hits are shown in Tables 9.1 and 9.2. The ratio of the efficiency in data to that in MC is taken as the systematic uncertainty. These uncertainties are 3% for missing inner hits and 2% for missing middle hits.

Table 9.1: The efficiency to pass the missing inner hits requirement, for events in the *Muon Control Sample*.

	$\epsilon(N_{\text{miss}}^{\text{inner}} == 0)$
data	0.956 ± 0.005
MC	0.984 ± 0.004
data/MC	0.972 ± 0.006

Table 9.2: The efficiency to pass the missing middle hits requirement, for events in the *Muon Control Sample*.

	$\epsilon(N_{\mathrm{miss}}^{\mathrm{mid}} == 0)$
data	0.919 ± 0.005
MC	0.936 ± 0.004
data/MC	0.982 ± 0.006

9.5 Track reconstruction efficiency

The uncertainty in the track reconstruction efficiency is assessed with a tag and probe study [75]. The track reconstruction efficiency is measured for probe muons, which are reconstructed using information from the muon system only. We assign the uncertainty as the largest difference between data and simulation, which is 2%. However, we also conducted our own study of the track reconstruction efficiency as a function of the number of hits. We performed a modified tag and probe study using W$\rightarrow \mu\nu$ MC. In typical tag and probe studies, the number of expected hits associated with the probe track is not known. For this study, the tag is the original muon track with all hits, and the probe is the same muon track with all hits after the 5th valid hit removed. After removing hits from the track, we rerun the offline reconstruction algorithm. The systematic uncertainty is assessed by comparing the number of global muons and stand alone muons before and after removing hits from the track. The number of stand alone muons is unaffected, but if the corresponding tracker track is not reconstructed, it will not be considered a global muon. One such event is shown in Figure 9.6. The resulting uncertainty is 4%. However, the *Candidate Track* selection requires at least 7 valid hits. When the study is repeated removing hits after the 7th valid hit as opposed to the 5th valid hit, the uncertainty reduces to 1%. Since this is smaller than the aforementioned 2%, the standard uncertainty on the efficiency of track reconstruction, we use the larger as the value for this systematic uncertainty.

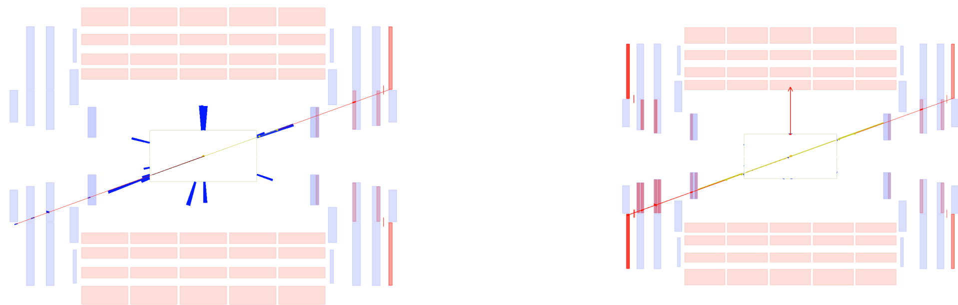

Figure 9.6: Left: A muon particle gun event in which no hits have been removed from the track. The event contains 2 global muons. Right: The same event after removing all hits after the 5th valid hit. The muon hits are unaffected. The event has one global muon and one stand alone muon.

9.6 Summary

The systematic uncertainties on the signal efficiency are summarized in Table 9.3.

Table 9.3: Summary of signal systematic uncertainties for charginos with masses in the range 100–600 GeV and $c\tau$ of 10–1000 cm

Jet radiation (ISR)	3–11%
Jet energy scale / resolution	0–7%
PDF	1–10%
Trigger efficiency	1–8%
$N_{\mathrm{miss}}^{\mathrm{outer}}$ modeling	0–7%
$N_{\mathrm{miss}}^{\mathrm{inner}}$, $N_{\mathrm{miss}}^{\mathrm{mid}}$ modeling	2–3%
$E_{\mathrm{calo}}^{\Delta R<0.5}$ modeling	6%
Pile-up	0–2%
Track reconstruction efficiency	2%
Total	9–22%

Chapter 10
Results and Interpretation

We observe two events in the search sample which is consistent with the expected background. In the absence of an excess, we set limits on the total production cross section of chargino-chargino and chargino-neutralino production, i.e. $q\bar{q}' \rightarrow \chi_1^{\pm}\chi_1^0$ and $q\bar{q} \rightarrow \chi_1^{\pm}\chi_1^{\mp}$. These limits allow us to exclude certain ranges of parameter space explored by the theoretical models to which we are sensitive.

In Section 10.1, we will detail the calculation used for the upper limit, then in Section 10.2, we will show the exclusion contours and the quoted upper limit.

10.1 Upper Limit Calculation

The upper limits are calculated using the procedure outlined in [76]. This procedure uses the CL_S method with a profile likelihood test statistic. First, we will discuss the signal efficiency, which is used as an input to the limit setting machinery, in Section 10.1.1. Then, the CL_S method and profile likelihood test statistic will be discussed in Section 10.1.2.

10.1.1 Signal Efficiency × Acceptance

To calculate the expected number of signal events, we must determine the signal acceptance × efficiency, $\mathcal{A} \times \epsilon$. Acceptance refers to likelihood of a chargino to be contained within the fiducial extent of CMS, and the efficiency is the likelihood for those accepted events to pass the remainder of the selection criteria.

For this search, $\mathcal{A}$ refers to those events with $\not\!\!E_T > 100$ GeV containing a chargino with $p_T > 50$ GeV and $|\eta| < 2.1$ divided by the number of generated events. ϵ is the fraction of those events which pass the remainder of *Disappearing Track* criteria. $\mathcal{A} \times \epsilon$ for some representative mass and lifetimes are listed in Table 11.1. A detailed signal MC cutflow for two mass hypotheses can be found in Appendix C.

Table 10.1: $\mathcal{A} \times \epsilon$ for signal events.

Chargino mass [GeV]	300	300	300	500	500	500
Chargino $c\tau$ [cm]	10	100	1000	10	100	1000
$\not\!\!E_T > 100$ GeV, $p_T > 50$ GeV, $\lvert\eta\rvert < 2.1$	4.1%	11%	40%	4.7%	13%	45%
Remaining *Disappearing Track* criteria	0.13%	1.0%	0.27%	0.095%	1.4%	0.47%

10.1.2 Profile Likelihood and CL$_S$

Now that we have calculated the expected number of signal events, we must decide if the observed data coincide with the signal + background hypothesis (chargino production) or with the background only hypothesis (the Standard Model). To determine this, we first define the test statistic; the chosen test statistic compresses all information used to discriminate between the two hypotheses, signal + background and background-only, into one number. Next, we generate distributions of the test statistic in the signal + background and background-only hypotheses. Then, we can decide which hypothesis is more compatible with the observed data.

Following the notation of [76] ,the signal + background hypothesis is defined as: $\mu s + b$, where μ is a dimensionless parameter used to characterize the signal strength, s is the expected number of signal events, and b is the expected number of background events. s is calculated using the samples discussed in Section 5.4 and the signal efficiency discussed in Section 10.1.1, and b corresponds to the background estimates detailed in Chapter 8. In the case of $\mu = 0$, we have the background-only hypothesis, defined simply as b.

To determine if the data are more in agreement with the signal + background hypothesis or the background only hypothesis, we use the Neyman-Pearson lemma [77], which states that the most appropriate test statistic to discriminate between two hypotheses is the ratio of their likelihood functions. The likelihood function for the signal + background hypothesis is defined as

$$\mathcal{L}(data|\mu, \theta) = \prod_{i=1}^{N} \frac{\mu s_i(\theta) + b_i(\theta)}{n_i!} e^{-\mu s_i(\theta) - b_i(\theta)} p(\tilde{\theta}|\theta) \tag{10.1}$$

where N is the number of bins contained in the input histogram that is used to set the limits. Since this search is a relatively simple counting experiment, we calculate the limits using a histogram that has only one bin, the observed number of events; therefore, N is simple equal to one. Then, *data* can be the observed data or pseudo-data generated with MC (toys), $s_i(\theta)$ is the expected number of signal events, $b_i(\theta)$ is the expected number of background events, n_i is the number of events in bin i, and θ represents all nuisance parameters (parameters that are not directly under investigation in the search, but still impact the result). $p(\tilde{\theta}|\theta)$ is the product of probability distribution functions ($pdf s$) for the nuisance parameters and $\tilde{\theta}$ is the default value of the nuisance parameter. For this search, the nuisance parameters consist of the additional systematic uncertainties as discussed in Chapter 9 and the statistical + systematic uncertainties on the background predictions as detailed in Chapter 8. The additional systematic uncertainties and the systematic uncertainties on the background predictions are modeled with log-normal distributions while the statistical uncertainties on the background predictions are modeled using gamma distributions. Log-normal distributions are recommended in the case of multiplicative corrections or efficiencies while the gamma distributions are recommended to model the statistical uncertainty in samples of limited statistics [78]. Similarly, the likelihood function for the background-only hypothesis is defined as

$$\mathcal{L}(data|0,\theta) = \prod_{i=1}^{N} \frac{b_i(\theta)}{n_i!} e^{-b_i(\theta)} p(\tilde{\theta}|\theta) \tag{10.2}$$

Note, that in Equations (10.1) and (10.2), the likelihood functions depend on μ as well as the nuisance parameters, θ. Since μ is the only parameter of interest in this search, we can instead use profile likelihoods [79]. $\mathcal{L}(data|\mu,\theta)$ becomes $\mathcal{L}(data|\mu,\hat{\theta_\mu})$, where $\hat{\theta_\mu}$ is the value of θ that maximizes $\mathcal{L}(data|\mu,\hat{\theta_\mu})$ for a specified value of μ, i.e. the conditional maximum-likelihood. Now we can define the test statistic as the profile likelihood ratio

$$\tilde{q_\mu} = -2ln \frac{\mathcal{L}(data|\mu,\hat{\theta_\mu})}{\mathcal{L}(data|\hat{\mu},\hat{\theta})}; 0 \leq \hat{\mu} \leq \mu \tag{10.3}$$

where, in the denominator, $\hat{\mu}$ and $\hat{\theta}$ represent the values that maximize $\mathcal{L}(data|\hat{\mu},\hat{\theta})$, i.e. the unconditional or global maximum likelihood. We require $0 \leq \hat{\mu}$ to ensure that the signal rate is always positive and $\hat{\mu} \leq \mu$ to ensure that the limit is one-sided, i.e. we only set upper limits, not lower limits on the cross section of chargino production [80].

Now, we can examine how to calculate the test statistic.

- First, we compute $\tilde{q_\mu}$ for the observed data, $\tilde{q_\mu^{obs}}$, using given values of μ.
- Next, we determine the best values for the nuisance parameters that correspond to the observed data, θ_μ^{obs} and θ_0^{obs}. θ_μ^{obs} corresponds to the signal + background hypothesis and θ_0^{obs} to the background-only hypothesis.

- Using θ_μ^{obs} and θ_0^{obs}, we perform many pseudo-experiments using toys to build *pdfs* of the test statistic, $\tilde{q}_\mu$. The *pdfs* are defined as $f(\tilde{q}_\mu|0, \hat{\theta}_0^{obs})$ for the background-only hypothesis and $f(\tilde{q}_\mu|\mu, \hat{\theta}_\mu^{obs})$ for the signal + background hypothesis.

Now that we have *pdfs* for the test statistic under the hypotheses of interest, we may now define their associated p-values. The p-value is a measure of the agreement between the observed data and the hypotheses. Mathematically, we define the p-value as:

$$p_\mu = P(\tilde{q}_\mu \geq \tilde{q_\mu^{obs}}|\text{signal} + \text{background}) = \int_{\tilde{q}_\mu^{obs}}^{\infty} f(\tilde{q}_\mu|\mu, \hat{\theta}_\mu^{obs}) d\tilde{q}_\mu \tag{10.4}$$

Larger values of p_μ indicate an agreement with the signal + background hypothesis. On the other hand, smaller values of p_μ indicate an agreement with the background only hypothesis. The convention in high energy physics is to exclude models at the 95% confidence level (CL) or exclude models in which $p_\mu \leq 0.05$

However, using this method will also exclude models in which the signal + background hypothesis is true 5% of the time. In the case where, μ is close to zero, this leads to exclusions of models to which the analysis is not sensitive. To avoid this shortcoming, we use the CL_S method. In this method, we define a second p-value associated with the background-only hypothesis

$$1 - p_b = P(\tilde{q}_\mu \geq \tilde{q_\mu^{obs}}|\text{background-only}) = \int_{\tilde{q}_0^{obs}}^{\infty} f(\tilde{q}_\mu|0, \hat{\theta}_0^{obs}) d\tilde{q}_\mu \tag{10.5}$$

Then, we define $\text{CL}_S(\mu)$ as

$$\text{CL}_s = \frac{p_\mu}{1 - p_b} \tag{10.6}$$

where a model is excluded at the 95% CL if $\text{CL}_S \leq 0.05$. Now, if the analysis has low sensitivity to a value of μ, $p_\mu \lesssim 1 - p_b$, then $\text{CL}_S(\mu) \lesssim 1$ and μ will not be excluded. On the other hand, in the realm of high sensitivity, $p_\mu \ll 1 - p_b$ so models excluded by $p_\mu \leq 0.05$ will also be excluded using the CL_S method.

Finally, we can determine the observed upper limit on the cross section as the lowest value of μ for which $\mathrm{CL}_S(\mu)= 0.05$, $\mu^{95\%\mathrm{CL}_s}$, times the expected signal model cross section.

Lastly, we can define the expected upper limits as well as the $\pm1\sigma$ and $\pm2\sigma$ bands associated with the background hypothesis by using only toys. We generate this pseudo-data and calculate $\mu^{95\%\mathrm{CL}_s}$ for each of them which builds a *pdf*, $f(\mu_{toy}^{95\%\mathrm{CL}_s})$ Therefore,

$$\text{median expected upper limit} \rightarrow 0.5 = \int_0^{\mu_{exp}^{95\%\mathrm{CL}_s}} f(\mu_{toy}^{95\%\mathrm{CL}_s}) d\mu_{toy}^{95\%\mathrm{CL}_s} \tag{10.7}$$

$$-1\sigma \text{ band} \rightarrow 0.16 = \int_0^{\mu_{-1\sigma,exp}^{95\%\mathrm{CL}_s}} f(\mu_{toy}^{95\%\mathrm{CL}_s}) d\mu_{toy}^{95\%\mathrm{CL}_s} \tag{10.8}$$

$$+1\sigma \text{ band} \rightarrow 0.84 = \int_0^{\mu_{+1\sigma,exp}^{95\%\mathrm{CL}_s}} f(\mu_{toy}^{95\%\mathrm{CL}_s}) d\mu_{toy}^{95\%\mathrm{CL}_s} \tag{10.9}$$

$$-2\sigma \text{ band} \rightarrow 0.025 = \int_0^{\mu_{-2\sigma,exp}^{95\%\mathrm{CL}_s}} f(\mu_{toy}^{95\%\mathrm{CL}_s}) d\mu_{toy}^{95\%\mathrm{CL}_s} \tag{10.10}$$

$$+2\sigma \text{ band} \rightarrow 0.975 = \int_0^{\mu_{+2\sigma,exp}^{95\%\mathrm{CL}_s}} f(\mu_{toy}^{95\%\mathrm{CL}_s}) d\mu_{toy}^{95\%\mathrm{CL}_s} \tag{10.11}$$

Now, we can use the information discussed in this section to present the results of this search.

10.2 Exclusion Contours

Two data events are observed in the search sample, which is consistent with the expected background. The observed data contribution after each stage of the *Dis-*

appearing Track selection is shown in Appendix D. The numbers of expected events from background sources compared with the data in the search sample are shown in Table 10.2. The mean and standard deviation of the distribution of pseudo-data generated under the background-only hypothesis provide an estimate of the total background contribution to the search sample of 1.4 ± 1.2 events.

Table 10.2: Numbers of expected and observed events in the *Disappearing Track* subsample.

electrons	$< 0.49_{\text{stat}} \quad < 0.50_{\text{stat+syst}}$
muons	$0.64(^{+1.47}_{-0.53})_{\text{stat}} \pm 0.32_{\text{syst}}$
taus	$< 0.55_{\text{stat}} \quad < 0.57_{\text{stat+syst}}$
fake tracks	$0.36(^{+0.47}_{-0.23})_{\text{stat}} \pm 0.13_{\text{syst}}$
data	2

The events are displayed in Figures 10.1 and 10.2. The distributions of several quantities are compared between the observed events and the estimated backgrounds in Figure 10.3. The shapes of the electron, muon, and tau background distributions are obtained from the data control samples enriched in the given background. The fake track distribution shapes are taken from the $Z \to ll$ *Control Sample*, using fake tracks with 5 hits, except for the plot of the number of hits, for which fake tracks with 7 or more hits are used.

The upper limits at 95% CL on the total production cross section of direct electroweak chargino-pair and chargino-neutralino production are calculated for various chargino masses and lifetimes. The NLO cross sections for these processes are taken from [81,82]. These limits are calculated using the procedure outlined in Section 10.1, and the constraint on the allowed chargino lifetime and mass is presented in Figure 10.4. The maximum sensitivity is for charginos with lifetime of 7 ns, for which

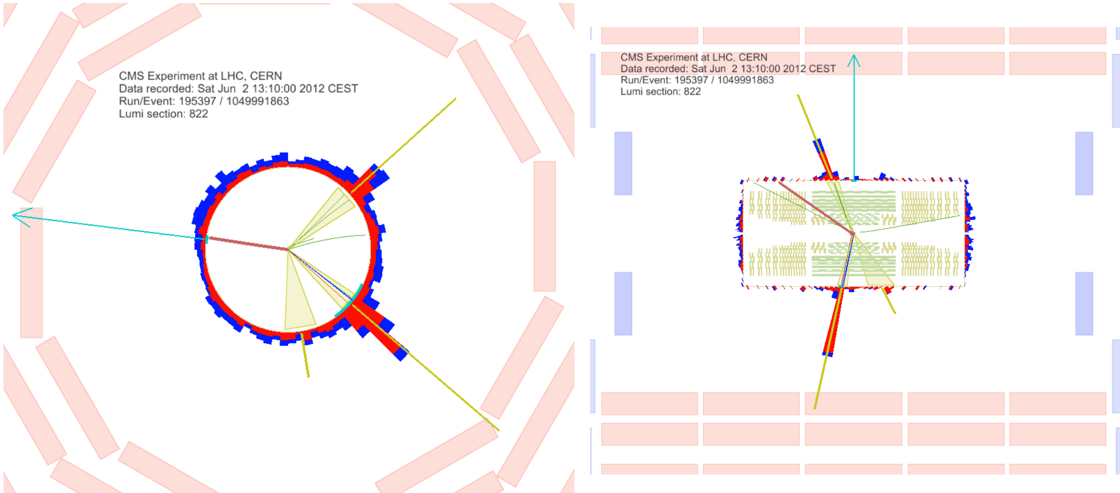

Figure 10.1: Data event 1049991863, which is in the *Disappearing Track* sub-sample. The candidate track is highlighted in red.

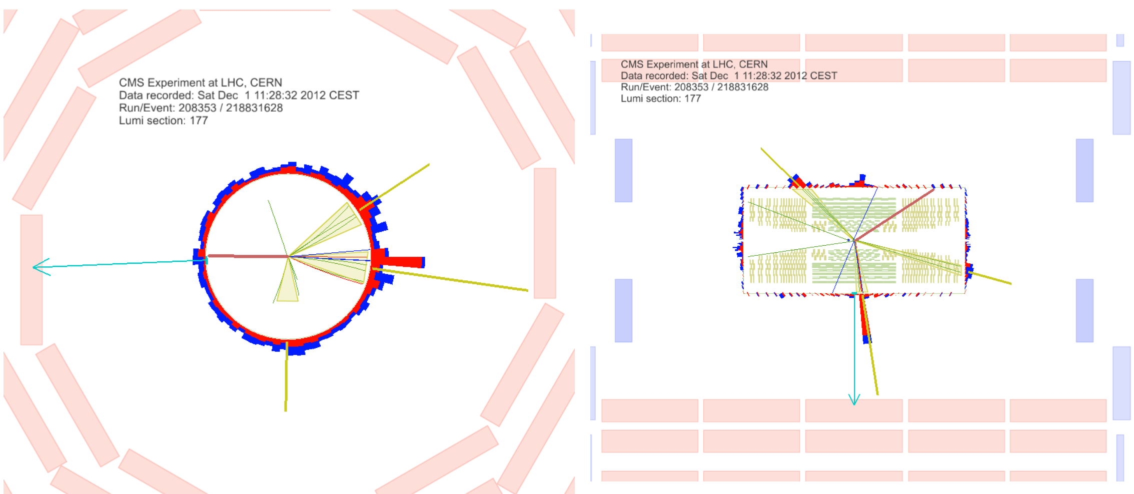

Figure 10.2: Data event 218831628, which is in the *Disappearing Track* sub-sample. The candidate track is highlighted in red.

masses less than 505 GeV are excluded at 95% CL.

In Figure 10.5, we show the constraint on the mass of the chargino and the mass difference between the chargino and neutralino, $\Delta m_{\chi_1} = m_{\chi_1^\pm} - m_{\chi_1^0}$, in the minimal

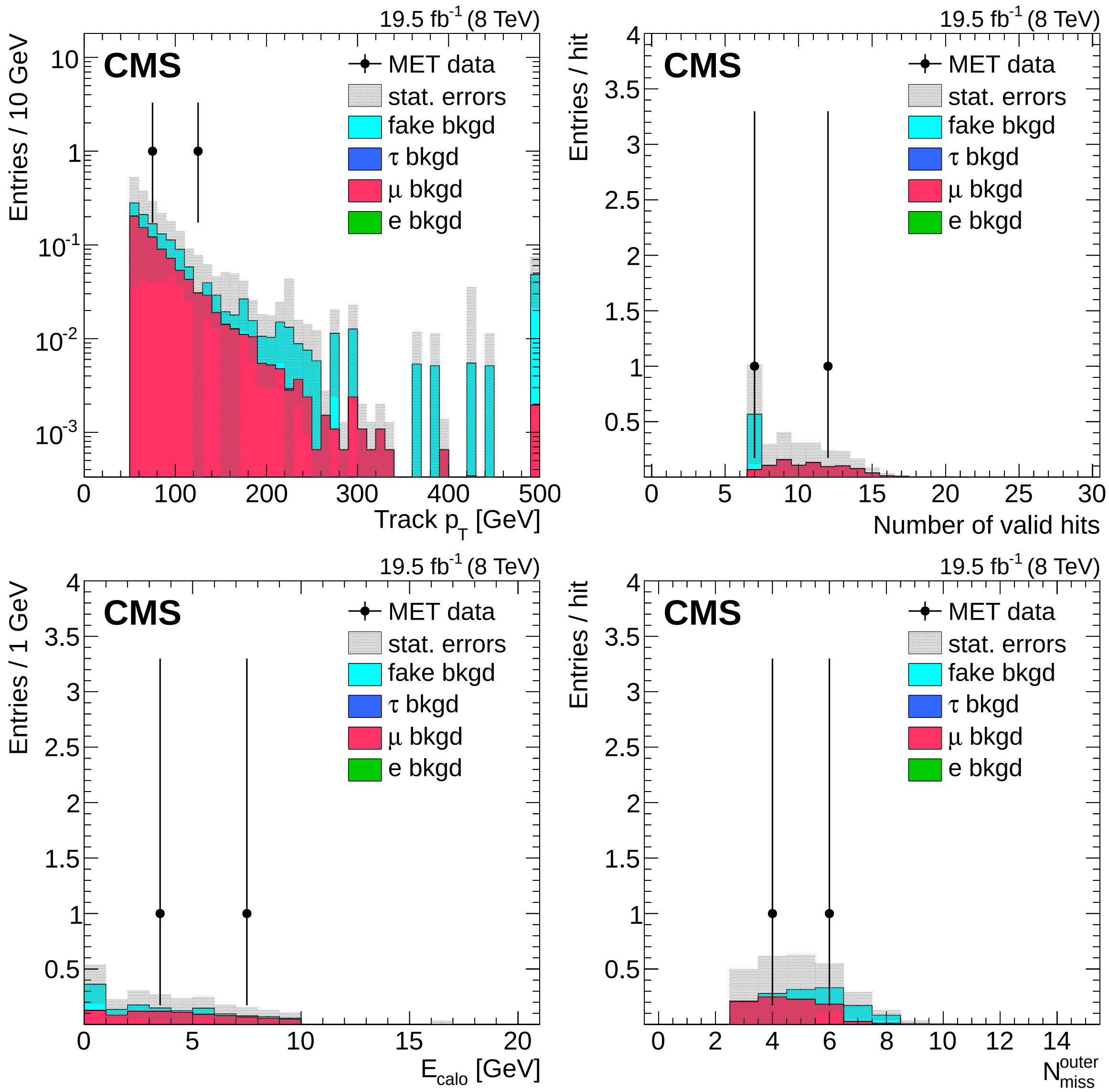

Figure 10.3: Distributions of the data and the estimated backgrounds in the search sample. The backgrounds are normalized to have the relative contributions of Table 10.2 and a total equal to the mean of the background-only pseudo-data (1.4 events). Histograms for the electron and tau backgrounds are not visible because the central value of their estimated contribution is 0.

AMSB model. The limits on $\tau_{\chi_1^\pm}$ are converted into limits on Δm_{χ_1} according to [83]. The two-loop level calculation of Δm_{χ_1} for wino-like lightest chargino and neutralino states [5] is also indicated. In the AMSB models we exclude charginos with mass less than 260 GeV, corresponding to chargino lifetime of ≈0.2 ns and $\Delta m_{\chi_1} = 160$ MeV.

In Figure 10.6, we show the observed upper limit on the total cross section of $pp \to \chi_1^{\pm}\chi_1^0$ plus $pp \to \chi_1^{\pm}\chi_1^{\mp}$ processes in terms of chargino mass and lifetime.

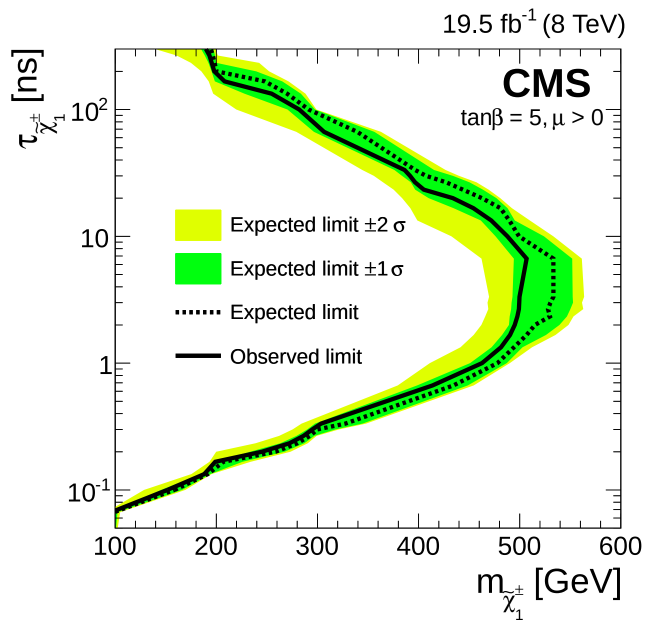

Figure 10.4: The constraint on the chargino lifetime and mass. The region to the left of the curve is excluded at 95% C.L.

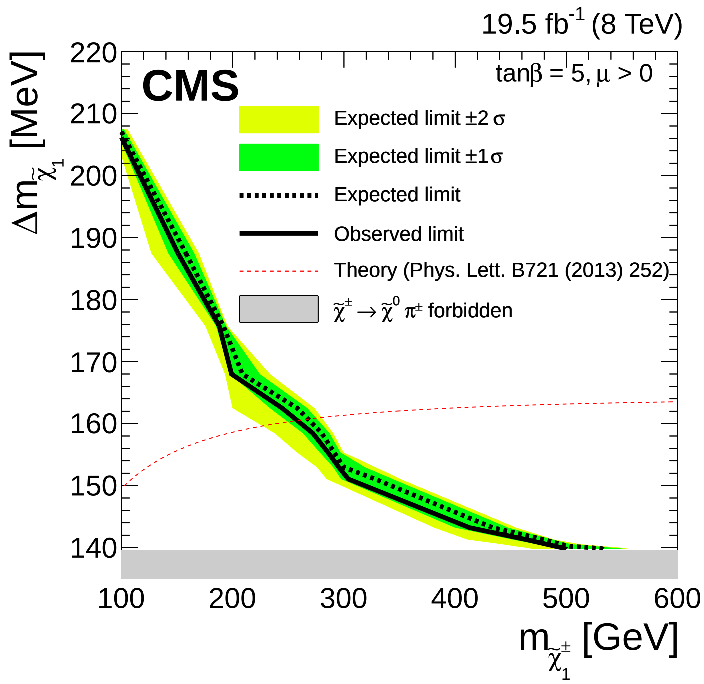

Figure 10.5: The solid curve shows the constraint on the chargino mass and the mass splitting between the chargino and neutralino in the AMSB model. The region to the left of the curve is excluded at 95% CL. The prediction for Δm_{χ_1} from [5] is also indicated.

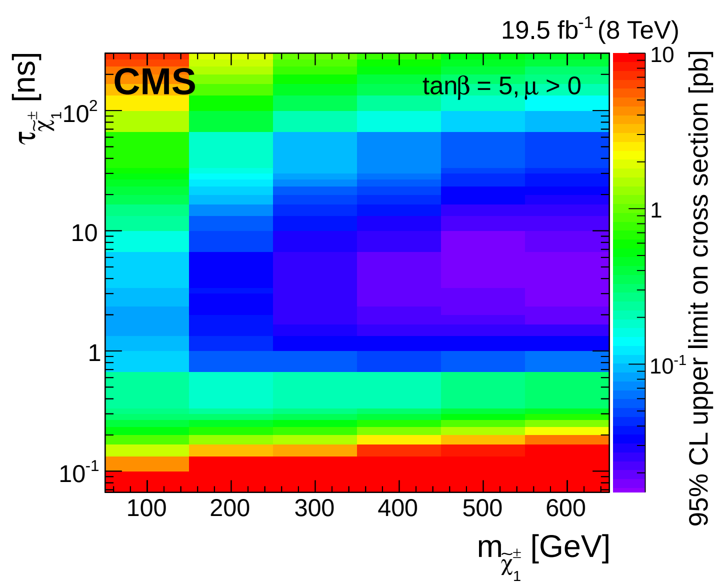

Figure 10.6: The observed upper limit (in pb) on the total cross section of pp $\to \chi_1^{\pm}\chi_1^0$ plus pp $\to \chi_1^{\pm}\chi_1^{\mp}$ processes as a function of chargino mass and lifetime. The simulated chargino mass used to obtain the limits corresponds to the center of each bin.

Chapter 11
Preparations for Run 2

This search will be repeated during Run 2 of the LHC. To prepare for this update, we have added to the CMS trigger menu a new trigger that has larger efficiency for the target signal model than the other available triggers.

11.1 Trigger Development

The triggers used in Run 1 and described in Section 5.2 collected events containing an ISR jet in which the $\not\!\!E_T$ arises from the recoil of the dichargino system against the ISR jet. As shown in Table 11.1, these triggers were a large source of signal efficiency loss, so we decided to improve upon this in Run 2.

Table 11.1: Trigger efficiencies for signal events in Run 1.

Chargino mass [GeV]	300	300	300	500	500	500
Chargino $c\tau$ [cm]	10	100	1000	10	100	1000
Trigger	10%	10%	7.4%	13%	13%	10%

We designed a new trigger path, `HLT_MET75_IsoTrk50`. Since tracking information is not available at L1, we still use L1 $\not\!\!E_T$ as the seed for this trigger (> 70 GeV). To ensure the greatest signal acceptance, we keep the $\not\!\!E_T$ requirement at the HLT level as low as possible (> 75 GeV). Next, to separate signal from background we require at least one high-p_T track (> 50 GeV). Lastly, to keep the rate down, we place quality requirements on the track and require that each track have $E_{\text{calo}}^{\Delta R<0.5} < 100$ GeV. The details of these trigger requirements are as follows:

- L1 $\not\!\!E_T$ seed > 70 GeV
- HLT $\not\!\!E_T > 75$ GeV
- ≥ 1 track with $p_T > 50$ GeV
- ≥ 1 track with relative track isolation, $(\Sigma p_T^{\Delta R<0.3} - p_T)/p_T < 0.05$
- ≥ 1 track with $N_{\text{hits}} \geq 5$
- ≥ 1 track with $N_{\text{miss}}^{\text{inner}} = 0$
- ≥ 1 track with $N_{\text{miss}}^{\text{mid}} = 0$
- $E_{\text{calo}}^{\Delta R<0.5} < 100$ GeV

11.2 Gain in Signal Efficiency

To determine the gain in signal efficiency, signal MC samples were generated as described in Section 5.2 but increasing $\sqrt{s}$ from 8 TeV to 13 TeV. We benchmark the signal efficiency in terms of MC samples with a chargino mass of 300 GeV and $c\tau$ of 100 cm. The signal efficiency is defined as (Number of events passing trigger + offline selection) / (Number of events passing offline selection). We define signal efficiency in this way to ensure that high quality tracks which we would like to keep at the analysis level are passing the trigger. The offline selection is defined as:

- $\not\!\!E_T > 100$ GeV

- χ track $p_T > 50$ GeV
- χ track with relative track isolation, $(\Sigma p_T^{\Delta R<0.3} - p_T)/p_T < 0.05$
- χ track with $|\eta| < 2.5$
- χ track with $N_{\text{hits}} \geq 5$
- χ track with $N_{\text{miss}}^{\text{inner}} = 0$
- χ track with $N_{\text{miss}}^{\text{mid}} = 0$

The signal efficiency for a chargino with a mass of 300 GeV and $c\tau$ of 100 cm for `HLT_MET75_IsoTrk50` compared to other $\not\!\!E_T$ triggers available for Run 2 are listed in Table 11.2. The addition of `HLT_MET75_IsoTrk50` increases the signal efficiency by at least 45%.

Table 11.2: Trigger efficiency of various $\not\!\!E_T$ triggers for signal MC with a chargino mass of 300 GeV and $c\tau$ of 100 cm.

Trigger name	Signal efficiency (%)
HLT_MET75_IsoTrk50	55
HLT_PFMET170NoiseCleaned	36
HLT_CaloMET200_NoiseCleaned	23
HLT_PFCenJet140_PFMETNoMu100_PFMHTNoMu140	38

In Figure 11.1, the trigger efficiency as a function of $\not\!\!E_T$ is shown for the $\not\!\!E_T$-based triggers available in Run 2 as well as `HLT_MET75_IsoTrk50`. For $\not\!\!E_T < 200$ GeV, there is a large gain in trigger efficiency for `HLT_MET75_IsoTrk50` over other triggers available in the menu. The trigger efficiency plateaus at $\not\!\!E_T \sim 400$ GeV.

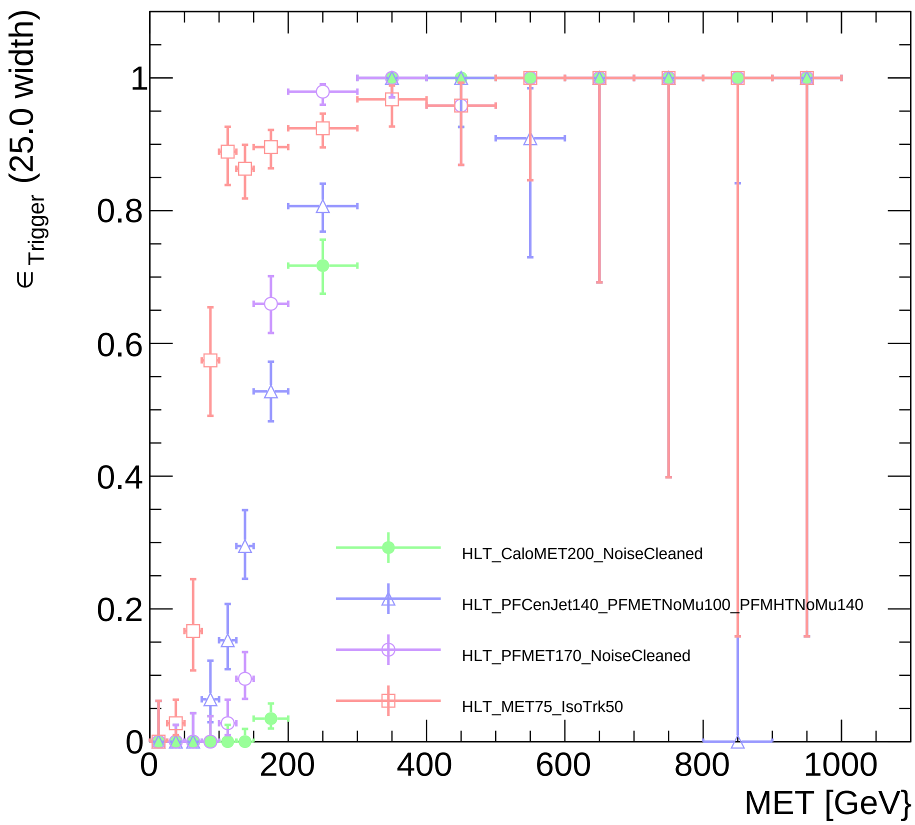

Figure 11.1: Distribution of trigger efficiencies as a function of $\not{E}_T$ for $\not{E}_T$-based triggers available in Run 2. For $\not{E}_T < 200$ GeV, there is a large gain in trigger efficiency for `HLT_MET75_IsoTrk50`. The trigger efficiency plateaus at $\not{E}_T \sim 400$ GeV.

Chapter 12
Conclusion

A search has been presented for long-lived charged particles that decay within the CMS detector and produce the signature of a disappearing track. In a sample of proton-proton data recorded at a collision energy of $\sqrt{s} = 8$ TeV and corresponding to an integrated luminosity of 19.5fb^{-1}, two events are observed in the search sample. Thus, no significant excess above the estimated background of 1.4 ± 1.2 events is observed and constraints are placed on the chargino mass, mean proper lifetime, and mass splitting. Direct electroweak production of charginos with a mean proper lifetime of 7 ns and a mass less than 505 GeV is excluded at 95% confidence level. In the AMSB model, charginos with masses less than 260 GeV, corresponding to a mean proper lifetime of 0.2 ns and chargino-neutralino mass splitting of 160 MeV, are excluded at 95% confidence level.

Appendix A
Background MC Samples

Table A.1: Background MC samples.

Individual Dataset Nickname	Individual Dataset Source Name
$QCD\ p_T\ 80-120$	QCD_Pt-80to120_*_8TeV_pythia6_**-v3_AODSIM
$QCD\ p_T\ 120-170$	QCD_Pt-120to170_*_8TeV_pythia6_**-v3_AODSIM
$QCD\ p_T\ 170-300$	QCD_Pt-170to300_*_8TeV_pythia6_v2_**-v1_AODSIM
$QCD\ p_T\ 300-470$	QCD_Pt-300to470_*_8TeV_pythia6_v3_**-v1_AODSIM
$QCD\ p_T\ 470-600$	QCD_Pt-470to600_*_8TeV_pythia6_**-v2_AODSIM
$QCD\ p_T\ 600-800$	QCD_Pt-600to800_*_8TeV_pythia6_**-v2_AODSIM
$QCD\ p_T\ 800-1000$	QCD_Pt-800to1000_*_8TeV_pythia6_**-v2_AODSIM
$QCD\ p_T\ 1000-1400$	QCD_Pt-1000to1400_*_8TeV_pythia6_**-v1_AODSIM
$QCD\ p_T\ 1400-1800$	QCD_Pt-1400to1800_*_8TeV_pythia6_**-v1_AODSIM
$QCD\ p_T\ 1800-\infty$	QCD_Pt-1800_*_8TeV_pythia6_**-v1_AODSIM
$t\ (s-channel)$	T_s-channel_*_8TeV-powheg-tauola_**-v1_AODSIM
$\bar{t}\ (s-channel)$	Tbar_s-channel_*_8TeV-powheg-tauola_**-v1_AODSIM
$t\ (t-channel)$	T_t-channel_*_8TeV-powheg-tauola_**-v1_AODSIM
$\bar{t}\ (t-channel)$	Tbar_t-channel_*_8TeV-powheg-tauola_**-v1_AODSIM
$t\ (tW-channel)$	T_tW-channel-DR_*_8TeV-powheg-tauola_**-v1_AODSIM
$\bar{t}\ (tW-channel)$	Tbar_tW-channel-DR_*_8TeV-powheg-tauola_**-v1_AODSIM
$t\bar{t}\ (hadronic)$	TTJets_HadronicMGDecays_8TeV-madgraph_**_ext-v1_AODSIM
$t\bar{t}\ (semi-leptonic)$	TTJets_SemiLeptMGDecays_8TeV-madgraph_**_ext-v1_AODSIM
$t\bar{t}\ (leptonic)$	TTJets_FullLeptMGDecays_8TeV-madgraph_**-v2_AODSIM
$Z\rightarrow\nu\nu\ (p_T\ 50-100)$	ZJetsToNuNu_50_HT_100_TuneZ2Star_8TeV_madgraph_**-v1_AODSIM
$Z\rightarrow\nu\nu\ (p_T\ 100-200)$	ZJetsToNuNu_100_HT_200_TuneZ2Star_8TeV_madgraph_**-v1_AODSIM
$Z\rightarrow\nu\nu\ (p_T\ 200-400)$	ZJetsToNuNu_200_HT_400_TuneZ2Star_8TeV_madgraph_**-v1_AODSIM
$Z\rightarrow\nu\nu\ (p_T\ 400-\infty)$	ZJetsToNuNu_400_HT_inf_TuneZ2Star_8TeV_madgraph_**-v1_AODSIM
$Z\rightarrow ee$	DYToEE_M-20_CT10_*_v2_8TeV-powheg-pythia6_**-v1_AODSIM
$Z\rightarrow\mu\mu$	DYToMuMu_M-20_CT10_*_v2_8TeV-powheg-pythia6_**-v1_AODSIM
$Z\rightarrow\tau\tau$	DYToTauTau_M-20_CT10_*_v2_8TeV-powheg-tauola-pythia6_**-v2_AODSIM
WW	WW_*_8TeV_pythia6_tauola_**-v1_AODSIM
WZ	WZ_*_8TeV_pythia6_tauola_**-v1_AODSIM
ZZ	ZZ_*_8TeV_pythia6_tauola_**-v1_AODSIM
$Z\gamma$	ZG_Inclusive_8TeV-madgraph_v2_**-v1_AODSIM
$W\gamma$	WGToLNuG_*_8TeV-madgraph-tauola_**-v1_AODSIM
$W\rightarrow l\nu\ (high\ p_T)$	WJetsToLNu_PtW-100_*_8TeV-madgraph_**-v1_AODSIM
$W\rightarrow l\nu\ (4\ Jets)$	W4JetsToLNu_TuneZ2Star_8TeV-madgraph_**-v1_AODSIM
$W\rightarrow l\nu(inclusive)$	WJetsToLNu_TuneZ2Star_8TeV-madgraph-tarball_**-v2_AODSIM
* TuneZ2star	
** Summer12_DR53X-PU_S10_START53_V7A	

Table A.2: Background MC samples.

Composite Dataset Color	Composite Dataset Nickname	Individual Dataset Nickname	Generated Events	Cross Section (pb)	Weighting Factor for 19.5 fb^{-1}
		$QCD\ p_T$ 80 − 120	5 988 720	1 034 000.0	3 370
		$QCD\ p_T$ 120 − 170	5 813 966	156 300.0	525
		$QCD\ p_T$ 170 − 300	18 932 228	34 140.0	35.2
		$QCD\ p_T$ 300 − 470	19 177 012	1 760.0	1.79
	QCD	$QCD\ p_T$ 470 − 600	3 903 001	113.9	0.57
		$QCD\ p_T$ 600 − 800	3 932 576	26.99	0.134
		$QCD\ p_T$ 800 − 1000	3 527 123	3.55	0.019 6
		$QCD\ p_T$ 1000 − 1400	1 919 722	0.737 8	0.007 5
		$QCD\ p_T$ 1400 − 1800	1 957 800	0.033 52	0.000 334
		$QCD\ p_T$ 1800 − ∞	953 491	0.001 829	$3.74e\ -05$
		$t\ (s-channel)$	259 657	3.79	0.285
		$\bar{t}\ (s-channel)$	139 835	1.76	0.246
	single top	$t\ (t-channel)$	3 754 544	56.4	0.293
		$\bar{t}\ (t-channel)$	1 933 504	30.7	0.31
		$t\ (tW-channel)$	496 918	11.1	0.436
		$\bar{t}\ (tW-channel)$	492 779	11.1	0.44
		$t\bar{t}\ (hadronic)$	31 171 004	112.3	0.070 3
	$t\bar{t}$	$t\bar{t}\ (semi-leptonic)$	25 303 396	107.7	0.083 1
		$t\bar{t}\ (leptonic)$	12 100 452	25.8	0.041 6
		$Z\rightarrow\nu\nu\ (p_T$ 50 − 100)	4 039 920	381.2	1.84
	$Z\rightarrow\nu\nu$	$Z\rightarrow\nu\nu\ (p_T$ 100 − 200)	4 414 132	160.3	0.709
		$Z\rightarrow\nu\nu\ (p_T$ 200 − 400)	5 047 844	41.49	0.16
		$Z\rightarrow\nu\nu\ (p_T$ 400 − ∞)	1 001 970	5.274	0.103
		$Z\rightarrow ee$	42 695 270	1 915.0	0.876
	$Z\rightarrow ll$	$Z\rightarrow\mu\mu$	48 810 855	1 915.0	0.766
		$Z\rightarrow\tau\tau$	48 768 831	1 915.0	0.766
		WW	9 993 617	54.84	0.107
		WZ	9 993 251	33.21	0.064 9
	Diboson	ZZ	9 741 539	17.65	0.035 4
		$Z\gamma$	6 320 039	123.9	0.383
		$W\gamma$	4 801 097	461.6	1.88
		$W\rightarrow l\nu\ (high\ p_T)$	12 718 810	282.4	0.433
	$W\rightarrow l\nu$	$W\rightarrow l\nu$ (4 *Jets*)	13 335 067	264.0	0.386
		$W\rightarrow l\nu(inclusive)$	57 698 420	37 510 .0	12.7

Appendix B
Implementation of Trigger Emulation

Since only the HLT_MonoCentralPFJet80_PFMETnoMu95_NHEF0p95 trigger is available in the background MC, we emulate the HLT_MonoCentralPFJet80_PFMETnoMu105_NHEF0p95 trigger using information stored in our ntuples. To emulate the HLT_MonoCentralPFJet80_PFMETnoMu105_NHEF0p95 trigger, we apply cuts on the following HLT filters:

- p_T of hltL1sL1ETM40 > 40 GeV
- p_T of hltCentralJet65L1FastJet > 65 GeV
- p_T of hltMET65 > 65 GeV
- p_T of hltCentralPFJet80 > 80 GeV
- p_T of hltPFMETnoMu > 105 GeV

If an events passes the above criteria, we consider it to pass the HLT_MonoCentralPFJet80_PFMETnoMu105_NHEF0p95 trigger.

To assess the systematic uncertainty on the trigger efficiency, we combine the background MC according to the relative contributions of each trigger, i.e.

Bkgd MC = (MC with 95 GeV threshold) * fracAB + (MC with 105 GeV threshold)

* fracCD, where fracAB = (integrated luminosity of 2012A and B) / (integrated luminosity for all 2012) and similarly for fracCD. This Bkgd MC combination is used to create the ratio plot in Figure 9.4. The ratio plot is then used to reweight the signal MC.

Appendix C
Cutflows for signal MC

The expected signal contributions after each stage of the *Disappearing Track* selection are shown in Table C.1, and the marginal efficiencies are shown in Table C.2.

$L = 19.519\,fb^{-1}$						Event yield
	$200GeV\chi^{\pm}$ $\tau = 0.1ns$	$200GeV\chi^{\pm}$ $\tau = 1ns$	$200GeV\chi^{\pm}$ $\tau = 10ns$	$400GeV\chi^{\pm}$ $\tau = 0.1ns$	$400GeV\chi^{\pm}$ $\tau = 1ns$	$400GeV\chi^{\pm}$ $\tau = 10ns$
trigger	$1\,842 \pm 43.7$	$1\,773 \pm 45.4$	$1\,731 \pm 41.7$	130 ± 2.16	130 ± 2.27	132 ± 2.34
$\not{E}_T > 100$ GeV	$1\,790 \pm 43$	$1\,724 \pm 44.7$	$1\,543 \pm 39.8$	127 ± 2.14	128 ± 2.25	127 ± 2.31
leading jet with $p_T > 110$ GeV	$1\,389 \pm 37.8$	$1\,340 \pm 39.7$	$1\,208 \pm 35.6$	102 ± 1.92	103 ± 2.03	102 ± 2.09
leading jet with $\|\eta\| < 2.4$	$1\,372 \pm 37.6$	$1\,318 \pm 39.1$	$1\,187 \pm 35.3$	101 ± 1.9	102 ± 2.01	99.9 ± 2.07
leading jet with charged hadron energy fraction > 0.2	$1\,342 \pm 37.3$	$1\,276 \pm 38.6$	$1\,151 \pm 34.8$	98.1 ± 1.87	99 ± 1.99	97.6 ± 2.05
leading jet with charged EM energy fraction < 0.5	$1\,337 \pm 37.2$	$1\,270 \pm 38.4$	$1\,150 \pm 34.8$	98.1 ± 1.87	98.8 ± 1.99	97.4 ± 2.04
leading jet with neutral hadron energy fraction <0.7	$1\,337 \pm 37.2$	$1\,270 \pm 38.4$	$1\,149 \pm 34.8$	98 ± 1.87	98.8 ± 1.99	97.4 ± 2.04
leading jet with neutral EM energy fraction < 0.7	$1\,329 \pm 37.1$	$1\,261 \pm 38.4$	$1\,146 \pm 34.8$	97.8 ± 1.87	98.2 ± 1.98	97 ± 2.04
0 jet pairs with $\Delta\phi > 2.5$	$1\,228 \pm 35.9$	$1\,147 \pm 36.6$	$1\,044 \pm 33.2$	89 ± 1.78	88.4 ± 1.88	86.9 ± 1.93
$\Delta\phi > 0.5 - \not{E}_T$&& 2 highest p_T jets	$1\,228 \pm 35.9$	$1\,147 \pm 36.6$	$1\,028 \pm 33$	89 ± 1.78	88.3 ± 1.88	85.1 ± 1.92
track with $p_T > 50$ GeV	367 ± 18.5	704 ± 26.5	909 ± 31.2	23.5 ± 0.871	50.7 ± 1.29	76 ± 1.79
track with $\|\eta\| < 2.1$	353 ± 18.2	669 ± 25.9	863 ± 30.3	22.1 ± 0.845	49.3 ± 1.28	73.6 ± 1.76
!in ECAL barrel-endcap crack, $1.42 < \|\eta\| < 1.65$	330 ± 17.7	630 ± 25.2	808 ± 29.2	20.5 ± 0.812	46.2 ± 1.24	70.2 ± 1.73
!in DT Wheel 0 gap, $0.15 < \|\eta\| < 0.35$	288 ± 16.4	564 ± 23.7	725 ± 27.7	17.2 ± 0.744	41.3 ± 1.16	63.9 ± 1.66
!in region of larger μ inefficiency, $1.55 < \|\eta\| < 1.85$	268 ± 15.7	527 ± 23	683 ± 26.9	16.3 ± 0.728	38.8 ± 1.11	60.3 ± 1.61
!within $\Delta R < 0.05$ of dead or noisy ECAL cluster	244 ± 14.8	493 ± 22.2	643 ± 26.2	14.9 ± 0.69	36.3 ± 1.08	56.9 ± 1.57
!within intermodule gaps of ECAL	241 ± 14.7	489 ± 22.1	639 ± 26.2	14.8 ± 0.688	35.8 ± 1.07	56.5 ± 1.57
!within $\Delta R < 0.25$ of errant CSC	234 ± 14.4	468 ± 21.6	614 ± 25.6	14.2 ± 0.675	34.7 ± 1.06	54.9 ± 1.55
track with $\|d_0\| < 0.02$cm	206 ± 13.3	450 ± 21.2	602 ± 25.3	12.1 ± 0.625	33.2 ± 1.03	53.8 ± 1.53
track with $\|d_z\| < 0.5$cm	197 ± 12.9	449 ± 21.2	602 ± 25.3	11.8 ± 0.62	33 ± 1.02	53.8 ± 1.53
track with ≥ 7 valid hits	165 ± 12.2	322 ± 16.4	565 ± 24.4	10.2 ± 0.595	21.3 ± 0.784	50.5 ± 1.47
track with no missing middle hits	153 ± 11.8	301 ± 15.9	544 ± 24	9.38 ± 0.566	20.3 ± 0.765	48.4 ± 1.44
track with no missing inner hits	137 ± 11.2	291 ± 15.6	534 ± 23.8	8.64 ± 0.545	19.5 ± 0.745	47.8 ± 1.43
track with $(\Sigma p_T^{\Delta R<0.3} - p_T)/p_T < 0.05$	1.5 ± 0.763	207 ± 12	469 ± 22.5	0.0631 ± 0.0455	12 ± 0.506	42.9 ± 1.36
$\Delta R > 0.5$ between track and subleading jet	0.58 ± 0.129	204 ± 11.9	462 ± 22.4	0.0104 ± 0.0031	11.8 ± 0.502	42.3 ± 1.35
!within $\Delta R < 0.15$ of τ, $p_T > 30$ GeV, $\|\eta\| < 2.3$, loose tau ID	0.58 ± 0.129	204 ± 11.9	462 ± 22.4	0.0104 ± 0.0031	11.8 ± 0.502	42.3 ± 1.35
!within $\Delta R < 0.15$ of e, $p_T > 10$ GeV	0.58 ± 0.129	204 ± 11.9	462 ± 22.4	0.0104 ± 0.0031	11.8 ± 0.502	42.3 ± 1.35
!within $\Delta R < 0.15$ of μ, $p_T > 10$ GeV	0.58 ± 0.129	204 ± 11.9	392 ± 21.6	0.0104 ± 0.0031	11.8 ± 0.502	36.3 ± 1.3
$E_{calo}^{\Delta R<0.5} < 10$ GeV	0.537 ± 0.127	195 ± 11.7	370 ± 21.1	0.00976 ± 0.00306	11.4 ± 0.497	33.6 ± 1.26
track with ≥ 3 missing outer hits	0.534 ± 0.127	143 ± 10.8	102 ± 12.1	0.00975 ± 0.00306	9.26 ± 0.476	9.9 ± 0.777

L = 19.519 fb^{-1}						Marginal efficiency
	$200GeV\chi^{\pm}$ $\tau = 0.1ns$	$200GeV\chi^{\pm}$ $\tau = 1ns$	$200GeV\chi^{\pm}$ $\tau = 10ns$	$400GeV\chi^{\pm}$ $\tau = 0.1cm$	$400GeV\chi^{\pm}$ $\tau = 1ns$	$400GeV\chi^{\pm}$ $\tau = 10ns$
trigger	8.09%	7.76%	7.8%	11.6%	11.6%	11.7%
$\not{E}_T > 100$ GeV	97.2%	97.2%	89.2%	98.2%	98.2%	96.1%
leading jet with $p_T > 110$ GeV	77.6%	77.7%	78.3%	80.5%	80.6%	79.9%
leading jet with $\|\eta\| < 2.4$	98.8%	98.3%	98.2%	98.5%	98.6%	98.4%
leading jet with charged hadron energy fraction > 0.2	97.8%	96.8%	97%	97.3%	97.5%	97.6%
leading jet with charged EM energy fraction < 0.5	99.6%	99.5%	99.9%	99.9%	99.8%	99.8%
leading jet with neutral hadron energy fraction <0.7	100%	100%	100%	100%	100%	100%
leading jet with neutral EM energy fraction < 0.7	99.4%	99.3%	99.7%	99.8%	99.4%	99.7%
0 jet pairs with $\Delta\phi > 2.5$	92.4%	91%	91.1%	91%	90%	89.6%
$\Delta\phi > 0.5 - \not{E}_T$&& 2 highest p_T jets	100%	100%	98.5%	100%	99.9%	98%
track with $p_T > 50$ GeV	29.9%	61.4%	88.4%	26.4%	57.4%	89.2%
track with $\|\eta\| < 2.1$	96.1%	95%	94.9%	93.7%	97.2%	96.8%
!in ECAL barrel-endcap crack, $1.42 < \|\eta\| < 1.65$	93.4%	94.1%	93.7%	92.8%	93.7%	95.4%
!in DT Wheel 0 gap, $0.15 < \|\eta\| < 0.35$	87.5%	89.6%	89.6%	84%	89.4%	91.1%
!in region of larger μ inefficiency, $1.55 < \|\eta\| < 1.85$	92.9%	93.5%	94.3%	95%	93.9%	94.3%
!within $\Delta R < 0.05$ of dead or noisy ECAL cluster	91%	93.4%	94.2%	91.5%	93.7%	94.3%
!within intermodule gaps of ECAL	99.9%	99.9%	100%	100%	99.9%	99.8%
!within $\Delta R < 0.25$ of errant CSC	96.9%	95.7%	96.1%	96.3%	96.9%	97.3%
track with $\|d_0\| < 0.02$cm	87.8%	96.3%	98%	84.7%	95.6%	98%
track with $\|d_z\| < 0.5$cm	96.1%	99.6%	100%	98%	99.5%	99.9%
track with ≥ 7 valid hits	83.6%	71.7%	93.8%	86.5%	64.6%	93.9%
track with no missing middle hits	92.9%	93.5%	96.3%	91.7%	95.4%	95.8%
track with no missing inner hits	89.6%	96.8%	98.2%	92.1%	95.6%	98.8%
track with $(\Sigma p_T^{\Delta R<0.3} - p_T)/p_T < 0.05$	1.09%	71.1%	87.9%	0.73%	61.5%	89.8%
$\Delta R > 0.5$ between track and subleading jet	38.7%	98.7%	98.3%	16.5%	98.5%	98.5%
!within $\Delta R < 0.15$ of τ, $p_T > 30$ GeV, $\|\eta\| < 2.3$, loose tau ID	100%	100%	100%	100%	100%	100%
!within $\Delta R < 0.15$ of e, $p_T > 10$ GeV	100%	100%	100%	100%	100%	100%
!within $\Delta R < 0.15$ of μ, $p_T > 10$ GeV	100%	99.9%	97.7%	100%	100%	97.3%
$E_{calo}^{\Delta R<0.5} < 10$ GeV	92.7%	95.5%	94.4%	93.5%	96.3%	92.6%
track with ≥ 3 missing outer hits	99.3%	73.3%	27.6%	99.9%	81.6%	29.5%

Appendix D
Cutflow for data

The observed data contributions after each stage of the *Disappearing Track* selection are shown in Table D.1.

L = 19.519 fb^{-1}	Event yield
	data
trigger	1.19×10^7
$\not\!\!E_T > 100$ GeV	6.13×10^6
leading jet with $p_T > 110$ GeV	4.86×10^6
leading jet with $\|\eta\| < 2.4$	4.7×10^6
leading jet with charged hadron energy fraction > 0.2	4.08×10^6
leading jet with charged EM energy fraction < 0.5	4.07×10^6
leading jet with neutral hadron energy fraction <0.7	4.07×10^6
leading jet with neutral EM energy fraction < 0.7	4.03×10^6
0 jet pairs with $\Delta\phi > 2.5$	1.79×10^6
$\Delta\phi > 0.5 - \not\!\!E_T$&& 2 highest p_T jets	1.77×10^6
track with $p_T > 50$ GeV	660 842
track with $\|\eta\| < 2.1$	605 783
!in ECAL barrel-endcap crack, $1.42 < \|\eta\| < 1.65$	551 710
!in DT Wheel 0 gap, $0.15 < \|\eta\| < 0.35$	494 445
!in region of larger μ inefficiency, $1.55 < \|\eta\| < 1.85$	452 382
!within $\Delta R < 0.05$ of dead or noisy ECAL cluster	420 309
!within intermodule gaps of ECAL	416 479
!within $\Delta R < 0.25$ of errant CSC	398 100
track with $\|d_0\| < 0.02$cm	311 701
track with $\|d_z\| < 0.5$cm	301 922
track with ≥ 7 valid hits	277 930
track with no missing middle hits	253 843
track with no missing inner hits	235 759
track with $(\Sigma p_T^{\Delta R<0.3} - p_T)/p_T < 0.05$	86 726
$\Delta R > 0.5$ between track and subleading jet	82 500
!within $\Delta R < 0.15$ of τ, $p_T > 30$ GeV, $\|\eta\| < 2.3$, loose tau ID	80 352
!within $\Delta R < 0.15$ of e, $p_T > 10$ GeV	63 181
!within $\Delta R < 0.15$ of μ, $p_T > 10$ GeV	56
$E_{calo}^{\Delta R<0.5} < 10$ GeV	13
track with ≥ 3 missing outer hits	2

Bibliography

[1] Luis Alvarez-Gaumé and John Ellis. Eyes on a prize particle. *Nature Physics*, 7(1):2–3, 2011.

[2] Stephen P Martin. A supersymmetry primer. *Perspectives on supersymmetry II*, pages 1–153, 1997.

[3] Jonathan L Feng and Takeo Moroi. Supernatural supersymmetry: Phenomenological implications of anomaly-mediated supersymmetry breaking. *Physical Review D*, 61(9):095004, 2000.

[4] CMS Collaboration. Summary of comparison plots in simplified models spectra for the 8 TeV dataset. *Public Twiki*, 2014. `https://twiki.cern.ch/twiki/bin/view/CMSPublic/SUSYSMSSummaryPlots8TeV#Results_SMS_Summary_plots`.

[5] Masahiro Ibe, Shigeki Matsumoto, and Ryosuke Sato. Mass splitting between charged and neutral winos at two-loop level. *Phys. Lett. B*, 721:252, 2013.

[6] ATLAS Collaboration. Search for charginos nearly mass degenerate with the lightest neutralino based on a disappearing-track signature in pp collisions at $\sqrt{s} = 8$ TeV with the ATLAS detector. *Phys. Rev. D*, 88:112006, 2013.

[7] CMS Collaboration. CMS luminosity-public results. *Public Twiki*, 2014. `https://twiki.cern.ch/twiki/bin/view/CMSPublic/LumiPublicResults`.

[8] Jean-Luc Caron. The LHC injection complex. Technical report, 1993.

[9] Werner Herr. Features and implications of different LHC crossing schemes. Technical report, 2003.

[10] CMS Collaboration. The CMS experiment at the CERN LHC. *Jinst*, 3(08):S08004, 2008.

[11] Rachel Paula Yohay. A Search in the Two-Photon Final State for Evidence of New Particle Production in pp Collisions at a Center of Mass Energy= 7 TeV. 2012.

[12] CMS Collaboration. Images of the CMS Tracker Endcap (TEC). Technical report, 2008.

[13] CMS Collaboration. 2012 ECAL detector performance plots. *CMS Detector Performance Summary CMS-DP-2013-007, CERN*, 39, 2013.

[14] Min Suk Kim. CMS reconstruction improvement for the muon tracking by the RPC chambers. *Journal of Instrumentation*, 8(03):T03001, 2013.

[15] Jason Nielsen. Fundamentals of LHC Experiments. *arXiv:1106.2516*, 2011.

[16] Paul Langacker. *The Standard Model and Beyond*. CRC press, 2011.

[17] Sheldon L Glashow. Partial-symmetries of weak interactions. *Nuclear Physics*, 22(4):579–588, 1961.

[18] Sheldon L Glashow, Jean Iliopoulos, and Luciano Maiani. Weak interactions with lepton-hadron symmetry. *Physical Review D*, 2(7):1285, 1970.

[19] Jeffrey Goldstone, Abdus Salam, and Steven Weinberg. Broken symmetries. *Physical Review*, 127(3):965, 1962.

[20] Abdus Salam and John Clive Ward. Electromagnetic and weak interactions. *Physics Letters*, 13(2):168–171, 1964.

[21] Murray Gell-Mann. A schematic model of baryons and mesons. *Physics Letters*, 8(3):214–215, 1964.

[22] F Abe, H Akimoto, A Akopian, MG Albrow, SR Amendolia, D Amidei, J Antos, C Anway-Wiese, S Aota, G Apollinari, et al. Observation of top quark production in pp collisions with the collider detector at Fermilab. *Physical review letters*, 74(14):2626, 1995.

[23] G Arnison, A Astbury, B Aubert, C Bacci, G Bauer, A Bézaguet, R Böck, TJV Bowcock, M Calvetti, T Carroll, et al. Experimental observation of isolated large transverse energy electrons with associated missing energy at s= 540 GeV. *Physics Letters B*, 122(1):103–116, 1983.

[24] M Banner, R Battiston, Ph Bloch, F Bonaudi, K Borer, M Borghini, J-C Chollet, AG Clark, C Conta, P Darriulat, et al. Observation of single isolated electrons of high transverse momentum in events with missing transverse energy at the CERN pp collider. *Physics Letters B*, 122(5):476–485, 1983.

[25] J Drees. Review of final LEP results or a tribute to LEP. *International Journal of Modern Physics A*, 17(23):3259–3283, 2002.

[26] Paul Langacker. Theoretical summary, electroweak physics. *arXiv:hep-ph/9905428*, 1999.

[27] Guido Altarelli. Experimental tests of perturbative QCD. 1989.

[28] François Englert and Robert Brout. Broken symmetry and the mass of gauge vector mesons. *Physical Review Letters*, 13(9):321–323, 1964.

[29] Peter W Higgs. Broken symmetries, massless particles and gauge fields. *Physics Letters*, 12(2):132–133, 1964.

[30] Francis Halzen and Alan D Martin. *Quark & Leptons: An Introductory Course In Modern Particle Physics*. John Wiley & Sons, 2008.

[31] ATLAS Collaboration. Observation of a new particle in the search for the Standard Model Higgs boson with the ATLAS detector at the LHC. *Physics Letters B*, 716(1):1–29, 2012.

[32] CMS Collaboration. Observation of a new boson at a mass of 125 GeV with the CMS experiment at the LHC. *Physics Letters B*, 716(1):30–61, 2012.

[33] SS AbdusSalam, BC Allanach, MJ Dolan, F Feroz, and MP Hobson. Selecting a model of supersymmetry breaking mediation. *Physical Review D*, 80(3):035017, 2009.

[34] Masahiro Ibe, Shigeki Matsumoto, and Tsutomu T Yanagida. Pure gravity mediation with $m_{3/2}$= 10–100 TeV. *Physical Review D*, 85(9):095011, 2012.

[35] Lisa Randall and Raman Sundrum. Out of this world supersymmetry breaking. *Nucl. Phys. B*, 557:79, 1999.

[36] Gian F. Giudice, Riccardo Rattazzi, Markus A. Luty, and Hitoshi Murayama. Gaugino mass without singlets. *JHEP*, 12:027, 1998.

[37] Archana Anandakrishnan, Linda M Carpenter, and Stuart Raby. Degenerate gaugino mass region and mono-boson collider signatures. *Physical Review D*, 90(5):055004, 2014.

[38] AC Kraan. SUSY searches at LEP. Technical report, 2005.

[39] S Ask. A Review of the supersymmetry searches at LEP. *arXiv preprint hep-ex/0305007*, 2003.

[40] Lee Sawyer. SUSY Searches at D0. Technical report, Fermi National Accelerator Lab., Batavia, IL (United States), 1993.

[41] Ping Hu. SUSY searches at CDF. Technical report, Fermi National Accelerator Lab., Batavia, IL (United States), 1993.

[42] CMS Collaboration. Search for fractionally charged particles in pp collisions at $\sqrt{s} = 7$ TeV. *Phys. Rev. D*, 87:092008, 2012.

[43] CMS Collaboration. Search for heavy long-lived charged particles in pp collisions at $\sqrt{s} = 7$ TeV. *Phys. Lett. B*, 713:408, 2012.

[44] CMS Collaboration. Searches for long-lived charged particles in pp collisions at $\sqrt{s} = 7$ and 8 tev. *JHEP*, 07:122, 2013.

[45] A Djouadi, S Rosier-Lees, M Bezouh, MA Bizouard, C Boehm, F Borzumati, C Briot, J Carr, MB Causse, F Charles, et al. The minimal supersymmetric standard model: Group summary report. *arXiv preprint hep-ph/9901246*, 1999.

[46] S Sekmen, S Kraml, J Lykken, F Moortgat, S Padhi, L Pape, M Pierini, HB Prosper, and M Spiropulu. Interpreting LHC SUSY searches in the phenomenological MSSM. *Journal of High Energy Physics*, 2012(2):1–14, 2012.

[47] CMS Collaboration. Search for disappearing tracks in proton-proton collisions at sqrt (s)= 8 tev. *arXiv:1411.6006*, 2014.

[48] Lyndon Evans and Philip Bryant. LHC machine. *Journal of Instrumentation*, 3(08):S08001, 2008.

[49] O Brüning et al. *LHC design report.* European Organization for Nuclear Research, 2004.

[50] CMS Collaboration. Commissioning of the particle-flow event reconstruction with the first LHC collisions recorded in the CMS detector. CMS Physics Analysis Summary CMS-PAS-PFT-10-001, 2010.

[51] CMS Collaboration. Particle–flow event reconstruction in CMS and performance for jets, taus, and $\not{E}_T$. CMS Physics Analysis Summary CMS-PAS-PFT-09-001, 2009.

[52] Thomas Speer, W Adam, R Frühwirth, A Strandlie, T Todorov, and M Winkler. Track reconstruction in the CMS tracker. *Nuclear Instruments and Methods in Physics Research Section A: Accelerators, Spectrometers, Detectors and Associated Equipment*, 559(1):143–147, 2006.

[53] Emilio Meschi, Pratibha Vikas, Christopher Seez, and T Monteiro. Electron reconstruction in the CMS electromagnetic calorimeter. Technical report, CERN-CMS-NOTE-2001-034, 2001.

[54] Matteo Cacciari, Gavin P Salam, and Gregory Soyez. The anti-kt jet clustering algorithm. *Journal of High Energy Physics*, 2008(04):063, 2008.

[55] J. Alwall, R. Frederix, S. Frixione, V. Hirschi, F. Maltoni, O. Mattelaer, H.-S. Shao, Torrielli P. Stelzer, T., and M. Zaro. The automated computation of tree-level and next-to-leading order differential cross sections, and their matching to parton shower simulations. *JHEP*, 07:079, 2014.

[56] Torbjorn Sjöstrand, Stephen Mrenna, and Peter Z. Skands. "PYTHIA 6.4 physics and manual". *JHEP*, 05:026, 2006.

[57] Simone Alioli, Paolo Nason, Carlo Oleari, and Emanuele Re. NLO single-top production matched with shower in POWHEG: s- and t-channel contributions. *JHEP*, 09:111, 2009.

[58] Stefano Frixione, Paolo Nason, and Carlo Oleari. Matching NLO QCD computations with Parton Shower simulations: the POWHEG method. *JHEP*, 11:070, 2007.

[59] Paolo Nason. A New Method for Combining NLO QCD with Shower Monte Carlo Algorithms. *JHEP*, 11:040, 2004.

[60] Simone Alioli, Paolo Nason, Carlo Oleari, and Emanuele Re. A general framework for implementing NLO calculations in shower Monte Carlo programs: the POWHEG BOX. *JHEP*, 1006:043, 2010.

[61] S. Agostinelli et al. Geant4–a simulation toolkit. *Nucl. Instrum. Meth. A*, 506:250, 2003.

[62] Peter Skands et al. SUSY Les Houches accord: interfacing SUSY spectrum calculators, decay packages, and event generators. *JHEP*, 07:036, 2004.

[63] H. Baer, F. E. Paige, S.C. Protopopescu, and X. Tata. ISAJET 7.48: A Monte Carlo event generator for pp, $p\bar{p}$, and e^+e^- interactions. 2000.

[64] Vardan Khachatryan et al. CMS Tracking Performance Results from Early LHC Operation. *Eur. Phys. J. C*, 70:1165, 2010.

[65] A. Bhatti et al. Search for New Physics in the Monojet final state at CMS. CMS Analysis Note 2012/421, CMS, 2012.

[66] CMS Collaboration. Baseline muon selections. *Public Twiki*, 2014. `https://twiki.cern.ch/twiki/bin/view/CMSPublic/SWGuideMuonId`.

[67] CMS Collaboration. KFFittingSmoother module. `https://cmssdt.cern.ch/SDT/lxr/source/TrackingTools/TrackFitters/src/KFFittingSmoother.cc?v=CMSSW_5_3_3`.

[68] Robert D. Cousins and Virgil L. Highland. Incorporating systematic uncertainties into an upper limit. *Nucl. Instrum. Meth. A*, 320:331, 1992.

[69] CMS Collaboration. CMS luminosity based on pixel cluster counting–summer 2013 update. CMS Physics Analysis Summary CMS-PAS-LUM-13-001, 2013.

[70] D. Barge et al. Hadronic Recoil Studies of Heavy Boosted Systems. CMS Note 2013/059, 2013.

[71] CMS Collaboration. Jet Energy Scale Uncertainties. *Public Twiki*, 2015. `https://twiki.cern.ch/twiki/bin/view/CMSPublic/WorkBookJetEnergyCorrections`.

[72] CMS Collaboration. Jet Energy Resolution Uncertainties. *Public Twiki*, 2015. `https://twiki.cern.ch/twiki/bin/view/CMS/JetResolution`.

[73] Michiel Botje, Jon Butterworth, Amanda Cooper-Sarker, Albert de Roeck, Joel Feltesse, Stefano Forte, Alexander Glazov, Joey Huston, Ronon McNulty, Torbjorn Sjostrand, and Robert Thorne. The PDF4LHC working group interim recommendations. 2011.

[74] S. Alekhin et al. The PDF4LHC working group interim report. 2011.

[75] CMS Collaboration. Measurement of tracking efficiency. CMS Physics Analysis Summary CMS-PAS-TRK-10-002, 2010.

[76] ATLAS and CMS Collaborations. Procedure for the LHC Higgs boson search combination in Summer 2011. Technical Report ATL-PHYS-PUB 2011-11, CMS NOTE 2011/005, 2011.

[77] Jerzy Neyman and Egon S Pearson. *On the problem of the most efficient tests of statistical hypotheses*. Springer, 1992.

[78] CMS Collaboration. Documentation of the RooStats-based statistics tools for Higgs PAG. *Public Twiki*, 2015. `https://twiki.cern.ch/twiki/bin/view/CMS/SWGuideHiggsAnalysisCombinedLimit`.

[79] Juerg Beringer, JF Arguin, RM Barnett, K Copic, O Dahl, DE Groom, CJ Lin, J Lys, H Murayama, CG Wohl, et al. Review of particle physics. *Physical Review D*, 86(1), 2012.

[80] Glen Cowan, Kyle Cranmer, Eilam Gross, and Ofer Vitells. Asymptotic formulae for likelihood-based tests of new physics. *The European Physical Journal C-Particles and Fields*, 71(2):1–19, 2011.

[81] W. Beenakker, M. Klasen, M. Krämer, T. Plehn, M. Spira, and P. M. Zerwas. Production of charginos, neutralinos, and sleptons at hadron colliders. *Phys. Rev. Lett.*, 83:3780, 1999. [Erratum:doi:http://dx.doi.org/10.1103/PhysRevLett.100.029901].

[82] M. Krämer et al. Supersymmetry production cross sections in pp collisions at $\sqrt{s} = 7$ TeV. 2012.

[83] C. Chen, M. Drees, and J. Gunion. Searching for invisible and almost invisible particles at e^+e^- colliders. *Phys. Rev. Lett.*, 76:2002, 1996. [Erratum: `http://arxiv.org/abs/hep-ph/9902309`].